Norwegian University
of Life Sciences

Master's Thesis 2024 60 ECTS
Faculty of Chemistry, Biotechnology and Food Science

Exploring the potential role of lytic polysaccharide monooxygenases from *Bacillus licheniformis* and *Bacillus spizizenii* in endospore germination

Ingeborg Langeby Korsane
Master of Biotechnology

This thesis utilized AI assistance throughout its preparation to enhance readability and clarity. While AI suggestions were considered, all final decisions regarding content and interpretation were made by the author.

Acknowledgements

This thesis was conducted at the Faculty of Chemistry, Biotechnology and Food Science at the Norwegian University of Life Sciences, under the supervision of Researcher Geir Mathiesen and PhD Candidate Hanne Berggreen.

Firstly, I am deeply grateful to Geir Mathiesen for his constant availability and exceptional dedication to always assist. Your openness to all questions and the safe learning environment you provided have been invaluable, and your willingness to share your extensive experience has been greatly appreciated.

I owe a special thank you to Hanne Berggreen for dedicating considerable time to helping me plan experiments and to answer my many questions. Your extensive planning and meticulous provision of detailed protocols brought a much-needed and appreciated sense of order during this chaotic time.

My appreciation extends to Eirik Kommedal, who generously shared his knowledge about endospores, and to Anton Stepnov for taking the time to share his detailed knowledge of LPMOs, including the reactions, mechanisms, and kinetics associated with these enzymes, all of which were crucial for my experiments.

To my roommates, thank you for enduring the chaotic conditions at home during our shared thesis-writing experience. A bitter but heartfelt thank you goes to my partner, who impressively managed to keep me away from the lab during the final phases of thesis writing. Thank you for being both my mentor and secretary, and for providing me with much-needed support during this period.

I also want to express my gratitude to all family and friends, and a special thank you to my fellow master's students at PEP. Your companionship made this endeavor feel like a shared survival experience, and I am thankful for the time we shared together at the lab.

Lastly, thank you to Marita and Else Marie for their assistance with microscopy, and to the second floor for allowing me access to their plate reader, which played an important role in my experiments.

Ås, May 2024

Ingeborg Langeby Korsane

Abstract

Lytic polysaccharide monooxygenases (LPMOs), traditionally recognized for degrading recalcitrant polysaccharides such as cellulose and chitin, constitute a superfamily with diverse substrate specificities and biological roles. This study examines the structural and functional properties of the previously uncharacterized *Bs*LPMO10A from *Bacillus spizizenii* along with the chitin-active *Bl*LPMO10A from the closely related *Bacillus licheniformis*, focusing on their potential roles in bacterial cell wall remodeling and endospore germination.

Initially, the study investigated the expression of *Bl*LPMO10A using a reporter gene system, fusing its promoter to mCherry within a vector transformed into *B. licheniformis* to potentially infer promoter activity. The findings revealed no detectable mCherry signal under various conditions, including growth in different media and during sporulation, suggesting an absence of LPMO expression under the tested conditions.

The activity and affinity of LPMOs for chitin were analyzed by mass spectrometry and binding assays, which confirmed the chitinolytic activity of *Bs*LPMO10A but suggested a relatively low chitin affinity for both LPMOs, which may hint to alternative biological functions.

The potential impact of LPMOs on bacterial cell walls was assessed by monitoring changes in optical density (OD600), indicative of cell lysis. While the data suggested that these LPMOs could potentially enhance lysozyme-mediated peptidoglycan breakdown in vegetative cells, any definitive conclusions were not drawn, and the potential impact of LPMO-mediated accumulation of reactive oxygen species (ROS) on cell integrity was considered.

Genomic investigations suggested a potential involvement of family 18 glycoside hydrolases in endospore germination in the parent strains of these LPMOs, substantiating the hypothesis that LPMOs may assist in this process. The potential impact of these *Bacillus*-derived LPMOs on endospore germination was assessed by monitoring the release of dipicolinic acid (DPA) and OD600. Despite complications in interpreting the results, an observed increase in DPA release in LPMO-treated endospores suggested possible LPMO involvement in endospore germination. Supporting these observations, phase contrast microscopy revealed that LPMO-treated endospores appeared phase bright and with size increases similar to what is observed in initial stages of germination, offering further indication of the involvement of LPMOs in this process.

Further investigations are necessary to explore how these LPMOs might contribute to endospore germination and to determine whether this potential function is widespread.

Sammendrag

Lytiske polysakkarid-monooksygenaser (LPMOer) er tradisjonelt anerkjent for å bryte ned komplekse polysakkarider som cellulose og kitin, og utgjør en superfamilie av enzymer med varierende spesifisiteter og biologiske roller. Denne studien undersøkte strukturelle og funksjonelle egenskaper hos den hittil ukarakteriserte *Bs*LPMO10A fra *Bacillus spizizenii* og den kitinaktive *Bl*LPMO10A fra *Bacillus licheniformis*, og fokuserte på å undersøke potensielle roller for disse LPMOene i remodellering av bakterielle cellevegger og spiring av endosporer.

Studien undersøkte først uttrykket av *Bl*LPMO10A ved bruk av et reporter-gensystem, hvor promotoren til denne LPMOen ble fusjonert med mCherry i en plasmidvektor. Vektoren ble transformert inn i *B. licheniformis*, der målet var å potensielt kunne få innsyn i promotoraktiviteten som styrer LPMO-uttrykk. mCherry-fluorescens ble ikke detektert under de testede forholdene, som inkluderte vekst i forskjellige medier og sporulering, noe som tydet på et fravær av LPMO-uttrykk under disse forholdene.

Kitinaktivitet og -affinitet for LPMOer ble analysert ved massespektrometri og bindingstester, noe som bekreftet at *Bs*LPMO10A katalyserte nedbrytning av kitin. Det ble antydet at begge LPMOene viste relativt lav kitinaffinitet, noe som kan antyde alternative biologiske funksjoner.

Den potensielle effekten av LPMO-aktivitet på bakterielle cellevegger ble vurdert ved å overvåke nedgang i optisk tetthet, noe som indikerer lysering av celler. Selv om resultatene antydet at LPMOene potensielt økte effekten av lysozym-mediert nedbrytning av bakterielle cellevegger, kunne ingen sikker effekt fastslås. Den potensielle effekten av LPMO-mediert akkumulering av reaktive oksygenarter (ROS) på cellenes integritet under forsøket ble vurdert.

Genomiske undersøkelser av artene antydet at familie 18 av glykosidhydrolaser muligens er involvert i spiring, noe som støttet hypotesen om at LPMOer kan bidra i denne prosessen. Effekten av disse LPMOene på spiring ble vurdert ved å overvåke frigjøringen av dipikolinsyre og nedgang i OD600. Til tross for utfordringer med å tolke resultatene fra dette eksperimentet, ble det observert en potensiell økning av DPA frigjort fra LPMO-behandlede sporer. Følgelig kan dette tyde på at LPMOer kan være involvert i spiring. Observasjonene ble støttet av fasekontrastmikroskopi, som viste at LPMO-behandlede sporer fremsto som mørkere og større enn ubehandlede, tilsvarende endringene som observeres i de tidligste stadiene av spiring, noe som ytterligere indikerte en potensiell rolle for LPMOer i denne prosessen.

Videre undersøkelser er nødvendige for å utforske hvordan disse LPMOene kan bidra til sporedannelse og for å fastslå om denne potensielle funksjonen er utbredt.

Abbreviations

AA	Auxiliary Activities
AEC	Anion-exchange chromatography
AscA	Ascorbic Acid
BlLPMO10A	LPMO derived from *B. licheniformis*
BSA	Bovine Serum Albumin
BsLPMO10A	LPMO derived from *B. spizizenii*
CAZyme	Carbohydrate Active enZyme
CBM	Carbohydrate-Binding Module
DPA	Dipicolinic Acid
GH	Glycoside Hydrolase
GlcNAc / NAG	N-acetylglucosamine
IPTG	Isopropyl β-D-1-thiogalactopyranoside
L-Ala	L-Alanine
LPMO	Lytic Polysaccharide Monooxygenase
m/z	Mass-to-charge ratio
MALDI-ToF	Matrix-Assisted Laser Desorption/Ionization Time-of-Flight
MIC	Minimum Inhibitory Concentration
MS	Mass Spectrometry
MurNAc / NAM	N-acetylmuramic acid
NMR	Nuclear Magnetic Resonance
PASC	Phosphoric Acid Swollen Cellulose
pI	Isoelectric point
RFU	Relative Fluorescence Units
ROS	Reactive Oxygen Species
SASPs	Small Acid-Soluble Proteins
SCLEs	Spore cortex-lytic enzymes
SDS-PAGE	Sodium Dodecyl Sulfate Polyacrylamide Gel Electrophoresis
SmLPMO10A	LPMO derived from *Serratia marcescens*
ScLPMO10C	LPMO derived from *S. coelicolor*
TbDPA	Terbium-DPA

Table of contents

1. Introduction

Enzymes are biocatalysts that accelerate biochemical reactions essential for life, significantly enhancing processes that would otherwise proceed at considerably slower rates. These catalytic proteins are essential to biological systems and have been adapted for a broad range of modern applications. The exploration of new enzymatic functions is crucial, as it not only deepens our understanding of biological mechanisms but also offers the potential for biotechnological innovations that could lead to significant progress in health research, environmental sustainability, and beyond.

With recent advancements in DNA sequencing technologies, an increasing number of genes encoding proteins with unknown functions are being discovered. Typically, the function of a newly sequenced protein is initially estimated by aligning its sequence with those of proteins whose functions are well-defined. Moreover, recent advancements in bioinformatics tools now allow for accurate sequence-based prediction of protein three-dimensional structures, alleviating the need for costly, time-consuming experimental methods and allowing for more accurate protein function estimation by structural alignment (Baek et al., 2021; Jumper et al., 2021; van Kempen et al., 2024). However, even members of protein superfamilies that share significant amino acid sequence and structural homology can catalyze different reactions or act on different substrates (reviewed by Jeffery et al., 2020).

In recent years, it has also become clear that differences in protein function within an enzyme superfamily can extend beyond differences in catalytic activity. Moonlighting proteins challenge the traditional one gene-one enzyme paradigm by exhibiting one or more noncatalytic functions in addition to a catalytic function (Jeffery C. J., 1999). These proteins are not only catalysts for specific reactions but also participate in entirely different activities, which are often unrelated to their enzymatic roles, and to date, over 500 moonlighting proteins have been identified (Chen et al., 2021). On the other hand, pseudoenzymes, while resembling the structure of active enzymes, have lost their catalytic activity due to mutations (Eyers et al., 2016), but often retain the ability to bind substrates or ligands and are commonly evolutionarily repurposed for regulatory functions (Jeffery et al., 2020).

1.1. Lytic polysaccharide monooxygenases

Lytic polysaccharide monooxygenases (LPMOs), a subgroup within Carbohydrate Active enZymes (CAZymes), exemplify the dynamic nature of enzyme research and the ongoing reevaluation of known protein functions.

Traditionally, LPMOs play a crucial role in degrading recalcitrant polysaccharides like cellulose and chitin, the two most abundant polymers in nature. These polymers are essential components of plant cell walls and arthropod exoskeletons, respectively, and constitute prime candidates for renewable biofuel production (Chen et al., 2020; Hayes et al., 2008). However, their complex structures pose significant challenges in converting them into fermentable sugars and other valuable products (Figure 1.1). Cellulose, a linear, non-branched homopolymer, consists of D-glucose units linked by β-1,4-glycosidic bonds, with cellobiose as the repeating unit (Cocinero, 2009). Chitin is similar but comprises the glucose derivative N-acetyl-D-glucosamine, with chitobiose as the repeating unit (Gooday, 1990). The structure of chitin results in two crystalline forms: α-chitin, which is denser and more rigid due to its antiparallel chain arrangement, and β-chitin, which is less dense due to a parallel arrangement (Gardner, 1975; Minke, 1978).

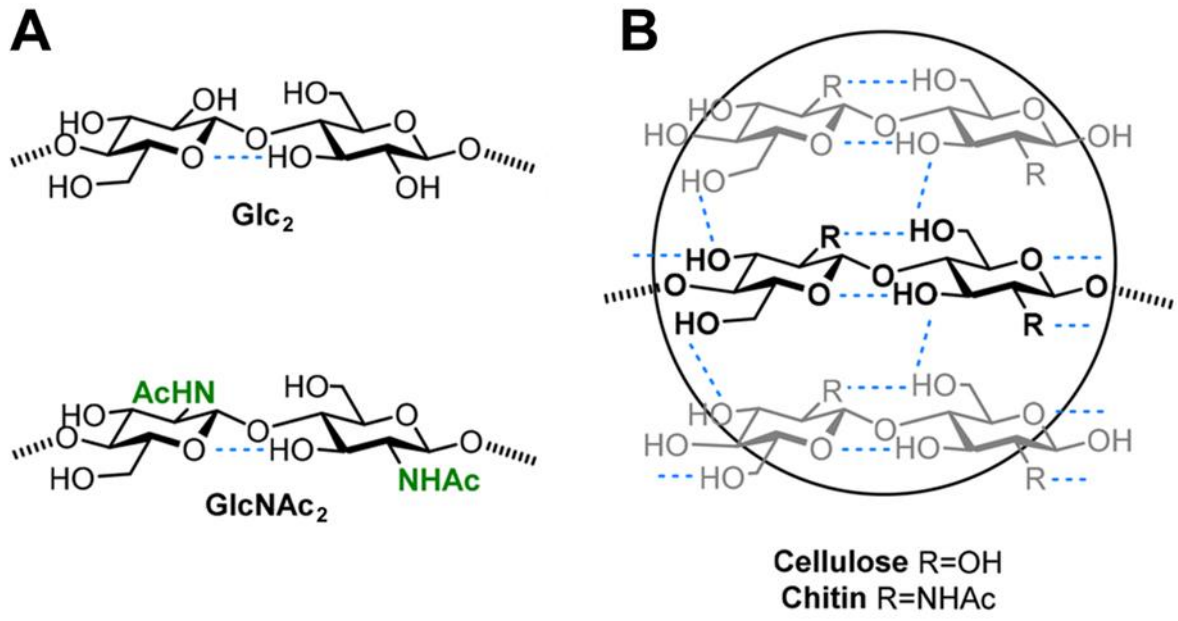

Figure 1.1. Structural comparison of cellulose and chitin. (A) The structures of cellulose and chitin both feature β-1,4-glycosidic linkages, with each successive monomer unit rotated by 180°. In cellulose, cellobiose (Glc_2) serves as the repeating unit, whereas in chitin, the repeating unit is N,N'-diacetylchitobiose (GlcNAc2), distinguished by its C_2 acetyl amine groups (AcHN/NHAc). **(B)** The hydrogen bonding patterns that occur within and between the polymer chains of cellulose (where R=OH) and chitin (where R=NHAc), stabilizing their crystalline structure. Adapted from Fittolani et al. (2022).

CAZymes are integral to both the synthesis and breakdown of carbohydrates, and are classified into five distinct classes by the CAZy database (www.cazy.org). Traditionally, the degradation of cellulose and chitin has been attributed to glycoside hydrolases (GHs), specifically cellulases and chitinases, that hydrolyze glycosidic bonds. These enzymes often include additional domains, such as non-catalytic carbohydrate-binding modules (CBMs), which enhance enzyme-substrate interactions by associating with other CAZymes (Cantarel et al., 2009; Drula et al., 2022). Cellulases and chitinases are crucial in enzyme cocktails for converting cellulose and chitin into fermentable sugars for biofuel production, with cellulases being particularly valuable in the industrial enzyme market (Singhania et al., 2017). However, glycoside hydrolases cannot access the more recalcitrant parts of these polymers, and their efficiency is further compromised by their processive nature; they require strong, sustained binding to cleave glycosidic bonds effectively and remain attached to the substrate, which inherently slows down their degradation rate (Horn et al., 2012).

The recent discovery of LPMOs has revolutionized our understanding of cellulose and chitin degradation. Initially identified as members of CAZy families CBM33 and GH61, research by Vaaje-Kolstad et al. (Vaaje-Kolstad et al., 2010, phillips) uncovered their role as copper-dependent oxidative enzymes, leading to the expansion of the CAZy database to include a new class of "auxiliary activities" (AAs). As a result, CBM33 and GH61 were reclassified as AA9 and AA10, respectively, and are now collectively known as LPMOs.

LPMOs function synergistically with glycoside hydrolases by introducing breaks in the crystalline regions of polysaccharides, thereby creating more accessible oxidized ends (Figure 1.2). This action significantly enhances the degradation efficiency of recalcitrant polysaccharides, and the addition of LPMOs to traditional cellulase cocktails result in significantly higher glucose yields (Pentekhina et al., 2020; Tokin et al., 2020; Müller et al., 2015). Moreover, LPMO activity has been shown to extend to various polysaccharide substrates, including hemicellulose (Agger et al., 2014), heteroxylans (Couturier et al., 2018; Hüttner et al., 2019; Zerva et al., 2020), starch (Lo Leggio et al., 2015; Vu et al., 2014; Vu et al., 2019), and components of pectin in plant cell walls, such as homogalacturonan and oligogalacturonides (Sabbadin et al., 2021). Based on their source of origin and substrate preference, LPMOs have expanded to include eight families, namely AA9-AA11 and AA13-AA17. Families AA9, AA11, and AA13 represent fungal LPMOs, while family AA10 is found across all domains of life but primarily comprises bacterial and some viral LPMOs.

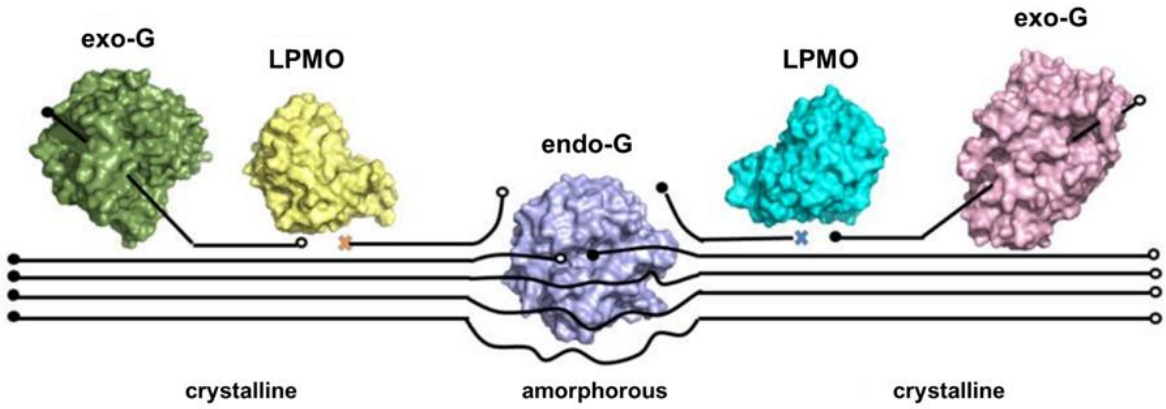

Figure 1.2. Polysaccharide degradation by GHs and LPMOs. This schematic illustrates the synergistic degradation of polysaccharides by GHs and LPMOs. Of the GHs, exoglucanases (exo-G) release disaccharide units from the ends of glycan chains, while endoglucanases (endo-G) cleave the internal glycosidic bonds in amorphous (less ordered) regions. LPMOs perform targeted oxidative cleavage within crystalline (highly ordered) regions, usually resistant to GH action, thus enhancing overall substrate accessibility. Released disaccharide units are further converted to glucose by β-glucosidases (not shown). Adapted from Liu (2019).

1.1.1. Structure of LPMOs

The function and activity of LPMOs are intricately tied to their three-dimensional structure (Figure 1.3). While some LPMOs are modular and possess additional domains like CBMs and GHs, AA10 LPMOs are primarily distinguished by their single catalytic domains (Finn et al., 2014).

Despite variations within the AA10 domain across different families, a conserved structural motif is present in the form of a slightly distorted β-sandwich. This motif consists of two β-sheets with seven or eight β-strands that are interconnected by α-helices and loops, which introduce variability into the substrate-binding surface. (Vaaje-Kolstad et al., 2017) (Figure 1.3 B). Particularly, the loop between β-strands 1 and 3, known as L2, forms a significant part of the binding surface, and exhibits the most structural variability in AA10 LPMOs (Book et al., 2014; Borisova et al., 2015; Forsberg, Mackenzie, et al., 2014; Vaaje-Kolstad et al., 2017).

The substrate-binding mechanism of *Sm*LPMO10A (also known as CBP21), the first characterized chitin-active LPMO10 derived from *Serratia marcescens*, has been thoroughly investigated using nuclear magnetic resonance (NMR). This research revealed that LPMO binding is predominantly driven by polar interactions. Aromatic residues are often involved in enzyme-carbohydrate interactions and are indeed found on the surface of LPMOs in conformations (i.e. rings parallel to the binding surface) that suggest a role in substrate binding (13, 27), with an aromatic residue (Tyr54 in *Sm*LPMO10A) playing a crucial role in orienting

the LPMO on the substrate (Aachmann et al., 2012). This single aromatic residue is conserved and positioned similarly in essentially all LPMO10s with known structures (Figure 1.3 A).

Central to the structure of LPMOs is their distinct metal-binding catalytic site (Figure 1.3 C). This configuration of the active site is a conserved feature present across all LPMO families, highlighting its critical role in the enzyme's activity. The site is characterized by a copper-histidine motif, often referred to as the "histidine brace." In this configuration, a copper ion is coordinated by two histidine residues, one of which is an N-terminal histidine. The N-terminal histidine interacts with the copper ion through both its side-chain and backbone nitrogen atoms, while the other histidine interacts through its side chain nitrogen atom, creating a T-shaped coordination geometry (Ciano et al., 2018; Quinlan et al., 2011). Moreover, the axial coordination positions, which are occupied by hydrophobic residues in AA10 LPMOs, are believed to help shape the copper binding site. In AA10s, an aromatic residue (phenylalanine or tyrosine) appears on the protein side, while an alanine is present on the solvent-exposed side (Hemsworth, Davies, & Walton, 2013; Hemsworth, Taylor, et al., 2013).

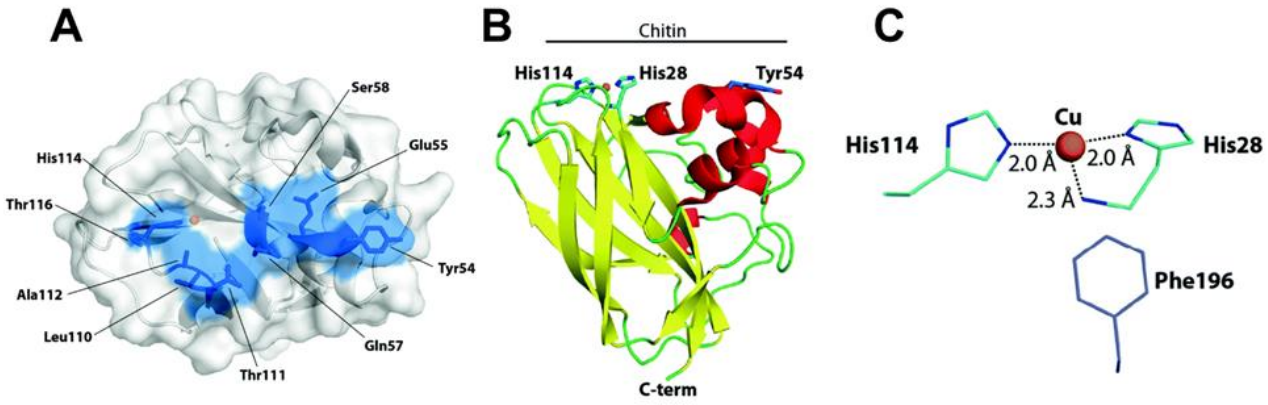

Figure 1.3. Structural features of LPMOs. **(A)** Surface view of *Sm*LPMO10A (CBP21), highlighting residues involved in binding (in blue), as identified by NMR studies (Aachmann et al. 2012). The copper ion of the active site is displayed in orange. **(B)** The overall structure of *Sm*LPMO10A features β-strands (yellow), helices (red), and loops (green), highlighting the active site (cyan) histidines and the Tyr54 crucial for substrate interaction. **(C)** The histidine brace at the copper site of *Sm*LPMO10A includes coordinating histidines (His28 and His114), and an axial Phe196. Structures were visualized using PyMol with PDB 2BEM for the enzyme and PDB 2YOX for copper coordination. Adapted from Courtade and Aachmann (2019).

1.1.2. Catalytic mechanism of LPMOs

As their name implies, LPMOs were originally classified as monooxygenases that utilized molecular oxygen and electrons for catalysis (Phillips et al., 2011; Vaaje-Kolstad et al., 2010). However, recent studies have demonstrated that LPMOs are more accurately described as

peroxygenases, preferring hydrogen peroxide (H_2O_2) as a co-substrate (Bissaro et al., 2017; Jones et al., 2020).

The catalytic cycle of LPMOs begins with the reduction of the copper ion from Cu(II) to Cu(I) in a process known as the 'priming reduction' (Figure 1.4 A). LPMOs can utilize a variety of electron sources for this reduction, including ascorbic acid, redox enzyme partners, lignin compounds, or even photoactivated molecules (Bissaro et al., 2016; Kuusk et al., 2019; Phillips et al., 2011; Westereng et al., 2015).

Subsequently, H_2O_2 acts as a co-substrate. H_2O_2 can be generated in situ either from the LPMO's own oxidase activity, which reduces oxygen independently of substrate oxidation, or from the auto-oxidation of reductants (Stepnov et al., 2021). Notably, the latter process is accelerated by the presence of free transition metal ions, such as Cu(II), which act as catalysts in this redox reaction. H_2O_2 directly interacts with the reduced copper ion of the LPMO active site, forming a Cu(I)-H_2O_2 complex. This complex undergoes homolytic cleavage, generating a Cu(II)-OH and a hydroxyl radical. These two species react to yield a copper-oxyl radical (Cu(II)-O•). The copper-oxyl radical can extract a hydrogen atom from the substrate, which results in a hydroxide associated with Cu(II) in the active site. This hydroxide then rebounds and combines with the substrate radical, resulting in the hydroxylation of the substrate. This introduction of a hydroxyl group to the carbon atom within the glycosidic linkage weakens the bond, predisposing it to spontaneous cleavage, which results in the formation of one regular and one new oxidized chain end (Bissaro et al., 2017) (Figure 1.4 B). Concurrently, the Cu(I) center is restored, preparing the LPMO for the next reaction cycle.

LPMOs are prone to autocatalytic inactivation, particularly in the absence of a substrate (Figure 1.4 C). Within the enzyme-substrate complex, the highly reactive hydroxyl radical intermediate is optimally positioned to facilitate the cleavage of glycosidic bonds. However, in the absence of a substrate, the hydroxyl radical will engage in nonproductive reactions, such as the oxidation of the enzyme itself, which may lead to a loss of catalytic activity (Kuusk & Väljamäe, 2021). It has been shown that amino acids close to the catalytic copper are primary targets of oxidative damage (Bissaro et al., 2017). This self-oxidation may cause copper to be released from the active site and end up free in solution. When a copper-sensitive reductant such as ascorbic acid is used for the priming reduction of LPMOs, a self-reinforcing process of LPMO inactivation can occur: damage to the LPMO leads to copper release, which in turn speeds up the autooxidation of ascorbic acid and increases H_2O_2 production, leading to further damage (Stepnov et al., 2022; Stepnov et al., 2021). A clear link exists between substrate affinity and

LPMO stability (Bissaro & Eijsink, 2023; Forsberg & Courtade, 2023), and the release of copper, which is indicative of enzyme inactivation, can be detected by analyzing the consumption of ascorbic acid (Østby et al., 2023).

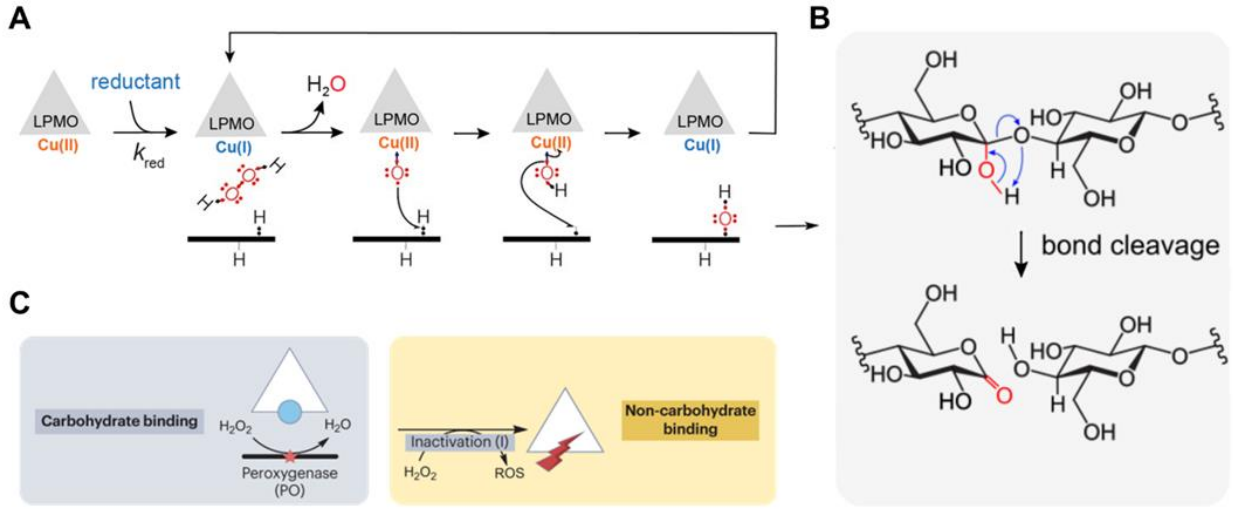

Figure 1.4. Catalytic mechanism of LPMO in polysaccharide oxidation. **(A)** This simplified reaction scheme outlines the oxidative mechanism, initiated by a 'priming reduction' where a reductant converts the LPMO from its Cu(II) to Cu(I) state, which subsequently binds H_2O_2, forming a Cu(I)-H_2O_2 complex (1). Homolytic cleavage of H_2O_2 produces a Cu(II)-OH and a hydroxyl radical, which react to form a Cu(II)-O• species and a water molecule (2). This species abstracts a hydrogen from the substrate, creating a substrate radical (3), and the copper-bound hydroxyl rebounds to hydroxylate the substrate, concurrently regenerating Cu(I) (4). **(B)** The hydroxylated polysaccharide undergoes molecular rearrangement, prompting bond cleavage and the formation of one normal and one oxidized chain end. **(C)** With a substrate present, LPMO-Cu(I) performs productive cleavage (left); in the absence of a substrate, the enzyme may be inactivated by off-pathway reactions with H_2O_2 that produce ROS, potentially leading to oxidative damage and loss of catalytic function (right). Adapted from Bissaro et al. (2017)and Munzone et al. (2024).

1.3.3. Emerging biological roles of LPMOs

In recent years, our understanding of LPMOs has expanded beyond their mere biomass-degrading roles for metabolic purposes (Figure 1.5). Recent studies have highlighted their involvement in a variety of biological processes, including pathogenesis and insecticide action, all the while moonlighting as polysaccharide degraders, and the range of identified roles, substrates, and applications for LPMOs is expected to expand further in the future (Vandhana et al., 2022).

LPMOs play critical roles in symbiotic associations, spanning mutualistic, commensalistic, and pathogenic interactions. For instance, in the mutualistic relationship between ectomycorrhizal fungus and California poplar tree roots, an AA9 LPMO aids in the subtle remodeling of plant cell walls, improving nutrient exchange (Fowler et al., 2019). In contrast, in the commensal relationships between a woodwasp and *Streptomyces* bacteria, and a marine caterpillar and the

bacterium *Teredinibacter turnerae*, the bacterial symbionts produce an AA10 LPMO that helps their host in cellulose breakdown (Takasuka et al., 2013).

LPMOs are also increasingly recognized for their role in pathogenesis. In plants, fungal pathogens utilize LPMOs to amplify invasion and evade plant immune responses (Li et al., 2020; Polonio et al., 2021), whereas *Cryptococcus neoformans*, the causative agent of human meningitis, employs an inactive LPMO-like protein to scavenge copper in copper-limited conditions such as the human brain, thereby supporting fungal virulence (Garcia-Santamarina et al., 2020).

Different bacterial species employ unique strategies in pathogenesis facilitated by multimodular enzymes with AA10 LPMOs domains. For instance, *Vibrio cholerae* uses the enzyme GbpA to enhance its attachment and colonization on both intestinal epithelial cells and crustaceans (Wong et al., 2012). Conversely, in honeybees, an LPMO derived from *Paenibacillus larvae* acts as a virulence factor, enabling the release of bacterial toxins to the gut epithelial cells of honeybee larvae (Garcia-Gonzalez et al., 2014). Moreover, *Listeria monocytogenes* is hypothesized to use *Lm*LPMO10 for host cell adhesion (Debroy et al., 2006; Frederiksen et al., 2013; Kawada et al., 2008; Tran et al., 2011), while *Pseudomonas aeruginosa* CbpD enhances its survival in host blood (Askarian et al., 2021).

Additionally, LPMOs have shown insecticidal properties and play roles in insect development. Insecticidal properties have been demonstrated by an AA10 LPMO derived from a fern (Shukla et al., 2016; Yadav et al., 2019), as well as by viral AA10 LPMOs, known as fusolins, which enhance bacterial insecticidal activity (Liu et al., 2011). Moreover, LPMOs play crucial roles in insect development in firebrats and fruit flies (Hosono et al., 2015; Mummery-Widmer et al., 2009; Sabbadin et al., 2018).

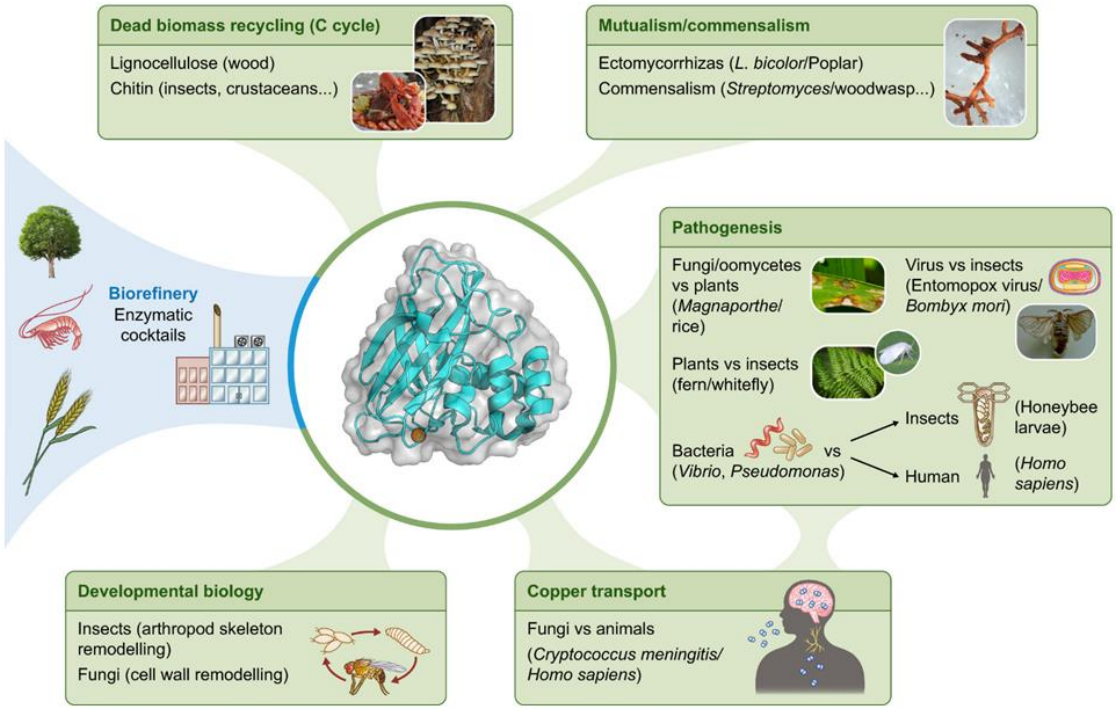

Figure 1.5. Diverse biological roles of LPMOs. LPMOs have been widely utilized to enhance the efficiency of biorefinery processes (blue zone), and naturally have been studied for their roles in biomass degradation and carbon cycling. Recent research has revealed the involvement of LPMOs in pathogenesis affecting plants, insects, and humans, as well as their support for various mutualistic and commensal relationships. Emerging studies also suggest LPMOs contribute to cell wall remodeling in arthropods and fungi. Adapted from Vandhana et al. (2022).

1.3.4. LPMOs from *S. coelicolor* potentially involved in cell wall remodeling and spore germination

LPMOs have been found to play crucial roles in cell wall remodeling, recently discovered in both fungi and bacteria. In fungi, Gonçalves et al. (2019) found an AA11 LPMO involved cell fusion regulation, while Zhong et al. (2022) revealed a similar function in bacteria, marking the first identification of LPMO-mediated breakdown of peptidoglycan in bacterial cell walls. Zhong et al. (2022) found that LpmP, or ScLPMO10E, one of seven AA10 LPMOs derived from *S. coelicolor*, cooperates with a GH16 hydrolase (CslZ) in a membrane-associated complex. Assisted by the LPMO, this complex locally remodels and degrades peptidoglycan at bacterial hyphal tips, creating pores for the external deposition of a protective glycan as the hyphae grow. While direct evidence of LPMO-mediated peptidoglycan breakdown is pending, the binding and turbidity-based activity assays conducted in the study strongly suggest that LpmP facilitates peptidoglycan degradation in *S. coelicolor*. With the widespread presence of LPMOs across bacterial species, this newly identified role in cell wall remodeling may indeed

be widespread, and may potentially represent numerous other roles involving bacterial cell walls that are yet to be discovered.

Additionally, a recent study conducted by Qezellou (2023) explored the impact of ScLPMO10D, a chitin-active LPMO from *S. coelicolor*, on the germination efficiency and viability of *Bacillus subtilis* endospores. Using several experimental approaches, the study suggested that LPMO activity might influence endospore germination and viability, because observed an increased number of colonies on agar plates when *B. subtilis* spores were incubated with ScLPMO10D. Furthermore, dose-response experiments indicated a correlation between increasing concentrations of ScAA10DCD and the number of colonies. While these findings are based on preliminary tests, they hint at a potential interaction of ScAA10DCD with the cortex peptidoglycan of endospores, which could represent a common functional role of LPMOs.

1.2. The genus *Bacillus*

Bacillus, a genus comprising some of the earlies described bacteria, encompasses diverse species known for their remarkable adaptability and prevalence in various environments. Originally named "*Vibrio subtilis*" upon its discovery by Ehrenberg in 1835 (Gordon, 1981), *Bacillus subtilis* remains the most extensively studied bacteria after *Escherichia. coli*. *Bacillus* species belong to the Bacillaceae family within the Firmicutes phylum and are characterized by their ability to form resilient endospores, which are vital for their survival during harsh conditions (Logan & De Vos, 2009).

Bacillus species are Gram-positive, rod-shaped bacteria, and display either aerobic or facultatively anaerobic metabolisms (Logan & De Vos, 2009). Despite these common traits, they exhibit considerable heterogeneity. Many species are motile, displaying various motilities such as swimming, swarming, and twitching (Calvio et al., 2005; Van Gestel et al., 2015). Furthermore, *Bacillus* bacteria can proliferate over a wide range of temperatures, with most preferring mesophilic conditions, whereas others are thermophilic or even psychrotolerant (Cihan et al., 2012). A notable characteristic is their metabolic versatility, as they can utilize a wide range of carbon sources for heterotrophic growth or alternatively grow autotrophically (Cihan et al., 2012).

Due to their robust physiological capacities, including biofilm and endospore formation, *Bacillus* are prevalent across diverse environments, and are particularly abundant in soils and

rhizospheres (Saxena et al., 2020). Their prevalence also includes the gastrointestinal tracts of humans and animals, and while most *Bacillus* species are not pathogenic, some can cause food poisoning or act as opportunistic pathogens, especially in immunocompromised individuals (Vos et al., 2011).

Most research on *Bacillus* has primarily targeted two *Bacillus* clades. The first includes *Bacillus cereus* and its close relatives, among which *Bacillus anthracis* is the causative agent of anthrax (Mock et al., 2001), *Bacillus cereus* is a significant food-borne pathogen (Stenfors et al., 2008), and *Bacillus thuringiensis* is utilized for agricultural biocontrol (Aronson et al., 2001). The second clade comprises *B. subtilis* and its close relatives, such as *Bacillus licheniformis*, *Bacillus amyloliquefaciens* and *Bacillus pumilus* (Sonenshein et al., 2002). *B. subtilis* notably serves as a model organism for studying Gram-positive bacteria and bacterial development.

1.2.1. *Bacillus spizizenii*

Previously considered a subspecies of *B. subtilis*, *Bacillus spizizenii* was recently reclassified as a distinct species (Dunlap et al., 2020). Named after the American bacteriologist J. Spizizen, whose work contributed to *B. subtilis* becoming a model organism in bacterial genetics, *B. spizizenii* shares many characteristics with its close relative. This includes aerobic growth with an optimal temperature of 30–35°C and a short doubling time of as little as 20 minutes (Dunlap et al., 2020).

Distinctive features of *B. spizizenii* include its halotolerance, thriving in environments with up to 7% (w/v) NaCl, and its ability to hydrolyze starch and casein as well as reduce nitrate to nitrite (Dunlap et al., 2020). Notably, *B. spizizenii* is renowned for its antimicrobial properties, producing antibacterial substances like lipopeptides and polypeptides, including the uniquely produced subtilin with broad-spectrum activity against Gram-positive bacteria (Wen et al., 2015; Yi et al., 2014; Dunlap et al., 2020).

1.2.2. *Bacillus licheniformis*

B licheniformis is a well-characterized species within the *B. subtilis* group, named after its rough and "licheniform" colonies. Unlike the majority of *Bacillus* species, it is a facultative anaerobe, which enables it to inhabit a broader range of ecological niches (Clements et al., 2002). Primarily, *B. licheniformis* exists as endospores in soil, but is also associated with birds, capable of degrading β-keratin found in feathers (Whitaker et al., 2005). This species also displays a

higher temperature tolerance compared to others in the *B. subtilis* group, with optimal growth between 42 and 50°C, and with some strains sustaining normal growth at temperatures as high as 65°C. (Sakai & Yamanami, 2006).

B. licheniformis is highly valued in industry for its production of extracellular products, such as enzymes and antimicrobial substances. These include proteases and α-amylase, with alkaline serine proteases being widely used in laundry detergents due to their effectiveness at both high pH and low temperatures (Eveleigh et al., 1981). Similar to *B. spizizenii*, *B. licheniformis* also synthesizes a variety of antimicrobial substances, including lipopeptides and polypeptides like bacitracin and proticin (Gherna et al., 1989). Furthermore, its potential as a probiotic is currently under investigation (Ramirez-Olea et al., 2022).

While *B. licheniformis* is not considered a causal agent of food poisoning, it presents significant challenges in food preservation (Nithya et al., 2012). Due to its ubiquitous presence as endospores in soil and dust, combined with its heightened resistance to heat treatments compared to other endospore-formers, it is known as a frequent contaminant of foods, particularly milk (Løvdal et al., 2013; Norris et al., 1981; Mostert et al., 1979; Foschino et al., 1990).

1.2.3. Bacterial endospores

The discovery of bacterial endospores in 1838 by Ehrenberg sparked systematic research into their resistance and life cycle (Gould, 2006). Endospores, produced by aerobic bacteria within *Bacillus* and anaerobic bacteria within the genus *Clostridium*, are highly specialized cells enabling survival under extreme environmental stresses such as starvation, high temperatures, and radiation. They exhibit metabolic dormancy and robust resistance to adverse conditions like desiccation, pH extremes, and antibiotics (Errington, 2003; Setlow, 2000).

The longevity of endospores is facilitated by their metabolic dormancy, ensuring virtually everlasting viability. Reports indicate endospores remaining viable over 10,000 years and even revival of endospores millions of years old (Gest et al., 1987; Nicholson et al., 2000; Vreeland et al., 2000). Their extraordinary survival capabilities extend to outer space, demonstrating resilience in extreme environments (Horneck et al., 1994).

The unique structure of bacterial endospores contributes to their resistance. The structure of the endospore includes several layers: the core, inner membrane, cortex, outer membrane, and coat layers, sometimes followed by the exosporium (Figure 1.6). Dehydration of the core during

sporulation results in a drastic reduction in water content from ~80% to 35-45%, significantly enhancing heat resistance (Gerhard and Marquis, 1989; Gould, 2006; Setlow, 2000). Believed to aid in this dehydration is dipicolinic acid (DPA), an endospore-specific compound present in the core as a complex with Ca^{2+}, where it constitutes 5-15% of the endospore's total dry weight (Paidhungat et al., 2000). Additionally, small acid-soluble proteins (SASPs) tightly bind to and protect the DNA within the core by enhancing endospore stability during dormancy, analogous to histones in eukaryotic DNA (Setlow, 1995).

Surrounding the core, a phospholipid inner membrane acts as a selective barrier, restricting the intrusion of harmful molecules (Cortezzo and Setlow, 2005; Nicholson et al., 2000). Further out, a thin peptidoglycan layer called the germ cell wall (GCW) is surrounded by a thicker layer of endospore-specific peptidoglycan known as the cortex (Popham, 2002). An additional outer membrane, not to be confused with the outer membrane of Gram-negative bacteria, envelops the cortex, though its exact function is unclear (Setlow, 2000). Beyond this, the proteinaceous endospore coat, containing up to 70 different proteins, provides the outermost defense, providing resistance to lysozymes, organic solvents, and various chemicals (McKenney et al., 2012; Driks, 1999; Nicholson et al., 2000; Setlow, 2000). Moreover, in members of the *B. cereus* group, the endospore may be loosely enveloped by an exosporium. Composed mainly of proteins and potentially containing carbohydrates, this exosporium is believed to play a role in helping the bacteria evade host defenses (Steichen et al., 2005; Boydston et al., 2006).

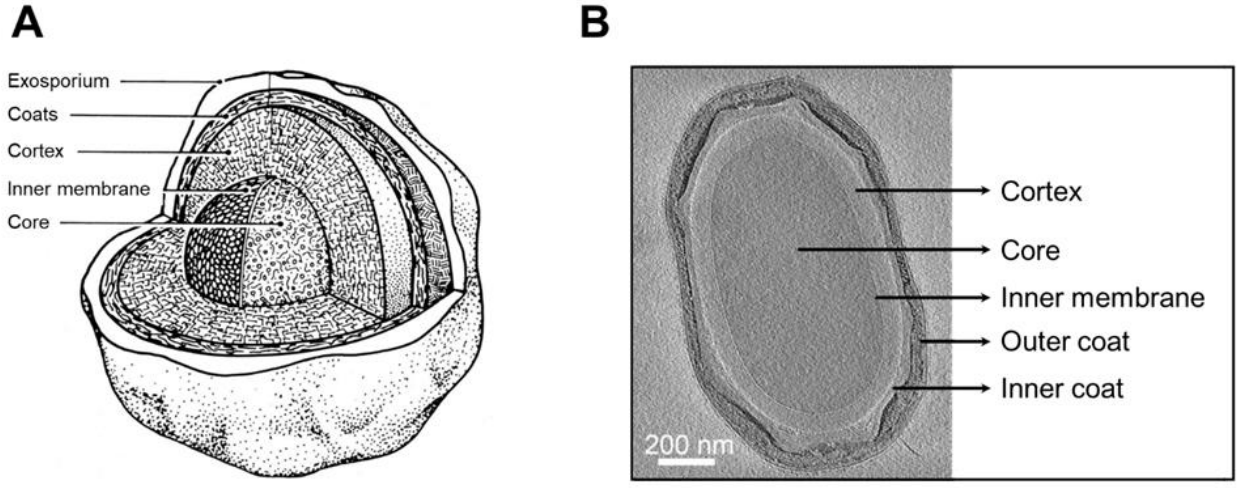

Figure 1.6. Structure of the bacterial endospore. **(A)** Schematic of an endospore showing key internal structures, adapted from Foster and Johnstone (1990). **(B)** Cryo-FIB microscopy-coupled cryo-electron tomography image of a mature *B. subtilis* endospore, highlighting important structures. Notably, *B. subtilis* lacks the exosporium. Scale bar: 200 nm. Adapted from Khanna et al. (2020).

1.2.4. Sporulation

Members of the *Bacillus* genus exhibit sophisticated survival strategies, including biofilm formation, genetic competence, and cannibalism, but will ultimately resort to sporulation when conditions deteriorate beyond sustainable limits, forming dormant endospores (Hoch et al., 1993; Kearns et al., 2005; Dubnau et al., 1996; Hofler et al., 2016).

Sporulation is an energy-intensive and irreversible process and is therefore a strategy of last resort. Nutrient depletion and high population density trigger a complex signal transduction pathway that orchestrates the early stages of sporulation (Molle et al., 2003). The entire process of endospore formation takes 7-8 hours to complete (Eichenberger et al., 2004).

Sporulation commences only after a cycle of DNA replication, ensuring the presence of two chromosome copies in the pre-divisional cell (Figure 1.7) (Veening et al., 2009). The process initiates with asymmetrical septation, which results in two cells of different sizes: a smaller forespore and a larger mother cell (Piggot et al., 1976). One copy of the chromosome is actively translocated into the forespore and subsequently condensed, resulting in its significant length being packed into a space about one-tenth of the cell's volume (Bath et al., 2000; Lopez-Garrido et al., 2018).

Post-septation, the forespore and mother cell exhibit distinct gene expression programs and developmental fates. Each compartment establishes its own gene expression regulated by specific transcription factors, alongside necessary inter-compartmental signaling that governs the developmental process's spatial and temporal aspects (Piggot et al., 2002; Errington et al., 2003). As development progresses, the forespore is completely engulfed by the mother cell through a phagocytosis-like process, facilitated by proteins that enzymatically remove peptidoglycan to allow membrane migration around the forespore (Morlot et al., 2010; Pogliano et al., 1999). This results in the forespore becoming a double membrane-bound protoplast within the mother cell, where it matures into an endospore (Piggot et al., 1976).

During maturation, a series of protective structures are constructed around the endospore core. Precursors for endospore peptidoglycan are produced in the mother cell and transferred across the outer forespore membrane into the intermembrane space, setting the stage for cortex synthesis between the two membranes (Fay et al., 2009; Popham et al., 2002). Simultaneously, coat proteins are synthesized in the mother cell to encase the developing endospore (Henriques et al., 2007). Additional processes include saturation of the forespore chromosome with SASPs, partial dehydration of the cytoplasm, and accumulation of Ca-DPA, all contributing to the

endospore's maturation (Setlow et al., 2007). Ultimately, the mother cell lyses, releasing the mature endospore into the environment, where it remains metabolically dormant until conditions favor germination and vegetative growth resumes (Lewis, 2000).

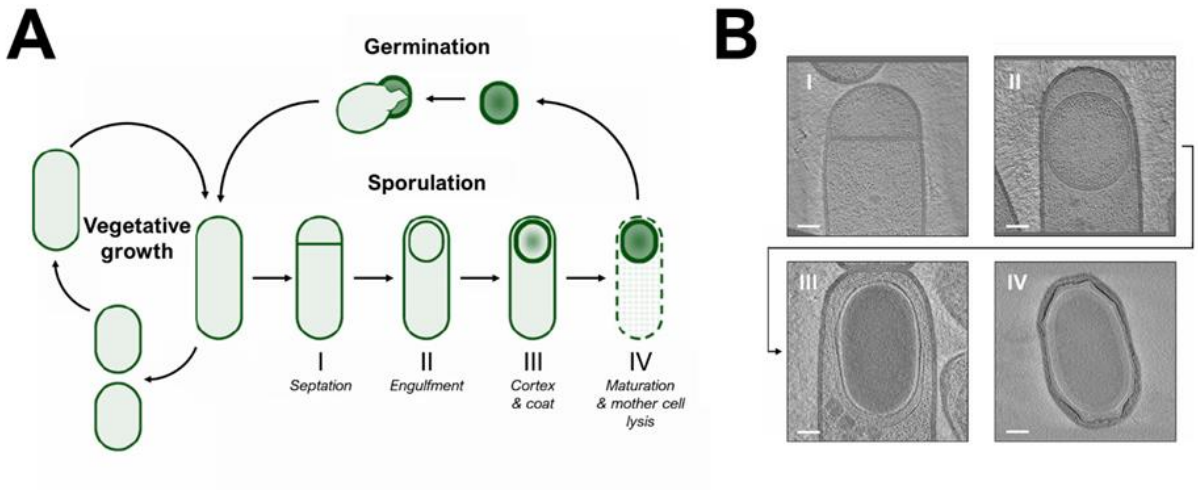

Figure 1.7. The sporulation cycle. **(A)** Schematic overview of the sporulation process initiated by nutrient scarcity. During vegetative growth, cells elongate and divide medially, producing two identical daughter cells. **I)** In response to starvation, cells undergo septation and asymmetric division, resulting in a smaller forespore and a larger mother cell. **II)** The forespore is engulfed by the mother cell, forming a double membrane-bound protoplast. **III)** endospore peptidoglycan and endospore coat proteins produced by the mother cell facilitate cortex and coat development. **IV)** The forespore chromosome is saturated with SASPs, the cytoplasm undergoes partial dehydration, and Ca-DPA accumulates, contributing to endospore maturation. The cycle concludes with the lysis of the mother cell, releasing the mature endospore into the environment, where it remains metabolically dormant until favorable conditions trigger germination and vegetative growth resumes. Adapted from Errington (2010). **(B)** The different stages of sporulation corresponding to those depicted in (A) as visualized in *B. subtilis* by cryo-FIB microscopy-coupled cryo-electron tomography. Scale bars: 200 nm. Adapted from Khanna et al. (2020).

1.2.5. Endospore germination and outgrowth

Endospore germination transforms a dormant, resistant endospore into an actively growing and dividing cell. Despite being in a dormant state, endospores can detect environmental cues through specific nutrients known as germinants that signal favorable growth conditions. Germination may be triggered by nutrients such as amino acids – especially L-alanine – and sugars, along with Ca2+DPA or peptidoglycan fragments released from other germinating endospores. Physical factors indicative of water returning to the environment, such as high hydrostatic pressure and abrasion, may also trigger germination (Gould et al., 1969; Setlow, 2003).

Germination begins when germinants bind to receptors embedded into the endospore's inner membrane, which through an unknown signaling mechanism initiates a sequence of events that degrade the endospore's protective structures and restart cellular metabolism (Trowsdale &

Smith, 1975). This process starts almost instantaneously upon exposure to germinants and takes only minutes to complete, committing the endospore to germinate even if germinants are later removed (Setlow, 2003).

The process includes a rapid efflux of monovalent cations (H+, Na+, and K+) and the release of stored Ca-DPA, causing partial rehydration of the endospore. This rehydration makes the endospore lose its refractivity, which is observable under a microscope as a change from phase bright to phase dark. The hydrolysis of the cortex layer, facilitated by cortex lytic enzymes, is crucial at this stage to allow swelling of the core by further water intake and expansion of the germ cell wall (Setlow et al., 2001). These events occur without detectable energy metabolism, and comprise the process of germination (Paidhungat et al., 2002).

Following the germination process, the resulting increased core hydration restores protein mobility within the endospore. This restoration permits the resumption of enzyme activity and metabolic processes within the endospore, occurring during a phase known as ripening, where no morphological changes are observed. In this phase, the degradation of SASPs frees the endospore's DNA, facilitating the initiation of RNA, protein, and DNA synthesis, which marks the transition into the outgrowth phase. During this phase, the endospore intensively synthesizes macromolecules to reconstruct a full-sized vegetative cell, which eventually emerges from the disintegrating endospore shells and is now capable of continued proliferation (Paidhungat et al., 2002).

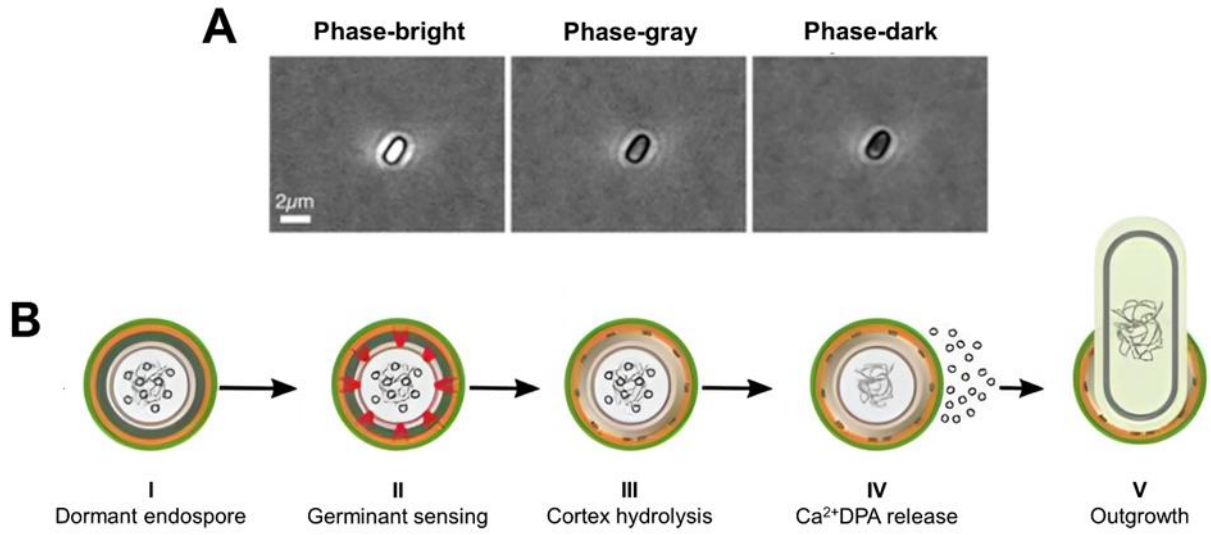

Figure 3. 1. (A) During germination, the refractility of dormant spores visualized by light microscopy changes as they become more hydrated. Hydration of the spore core occurs when the protective cortex layer is degraded during germination. Phase-gray spores have initiated germination and are becoming more hydrated as the cortex layer is being degraded. Phase-bright spores have completed germination because their cortex layer has fully degraded, resulting in full hydration of the core. Scale bar shows 2 μm. Adapted from Ribis and Shen (2023). **(B)**

Germination is activated upon sensing an appropriate small molecule, such as amino acids. The dormant spore initiates a signaling cascade that activates hydrolases and core hydration, which is necessary for metabolism to resume in the germinating spore. Adapted from Romero-Rodríguez et al. (2023).

1.3 The bacterial cell wall

The bacterial cell wall is a complex, dynamic structure surrounding the cell membrane, essential for the survival of bacterial cells. It provides structural support, protection, and shape, enabling cells to withstand osmotic pressure and mechanical stress. Additionally, the cell wall serves as a scaffold for various cellular components, including proteins and teichoic acids. The integrity of the cell wall is critical for cellular viability; any disruption in its biosynthesis, whether from mutations, antibiotic actions, or enzymatic degradation, can lead to immediate cell lysis.

1.3.1 Bacterial cell wall structure

The structure of bacterial cell walls varies significantly between Gram-positive and Gram-negative bacteria (Figure 1.8 A), contributing to their distinct staining patterns during the Gram staining process. Gram-negative bacteria feature a multilayered cell wall that includes an outer membrane composed of a phospholipid bilayer, enriched with lipopolysaccharides (LPS) (Silhavi et al., 2010; Caroff et al., 2019). Within this outer membrane resides the cytoplasmic membrane, separated by a periplasmic space containing a relatively thin peptidoglycan (PG) layer (Vollmer et al., 2008).

In contrast, Gram-positive bacteria feature a significantly thicker peptidoglycan layer, making up 30-70% of the cell wall's dry weight, in comparison to the 5-10% found in Gram-negative bacteria (Figure 1.8 A). Additionally, polyanionic polymers and proteins, mainly the polyalcohols called wall teichoic acids (WTAs), are covalently attached to the peptidoglycan layer. Some of these teichoic acids are covalently linked to lipids within the cytoplasmic membrane to form lipoteichoic acids (LTAs). Teichoic acids impart an overall negative charge to the Gram-positive cell wall due to their phosphate content, which is crucial for surface adhesion and the binding of metal ion (Matias and Beveridge, 2008; Swoboda et al., 2010; Rajagopal et al., 2025).

Peptidoglycan, often referred to as murein, is a polysaccharide and the principal structural component of the bacterial cell wall, essential for maintaining cell shape and integrity against internal and external pressures. The fundamental structure of peptidoglycan (Figure 1.8 B) is conserved across both Gram-positive and Gram-negative bacteria and features a glycan chain

similar to the one found in chitin (Figure 1.1). This glycan chain consists of alternating N-acetylglucosamine units (GlcNAc or NAG) and its lactyl ether, N-acetylmuramic acid (MurNAc or NAM), linked by β(1→4) glycosidic bonds (Weidel & Pelzer, 1964). Each NAM unit has a stem pentapeptide that is covalently attached, which enables cross-linking between the third amino acid and the penultimate amino acid of adjacent chains. These links can either be direct or occur via short peptide bridges, ultimately forming a robust, scaffold-like structure (Schleifer & Kandler, 1972).

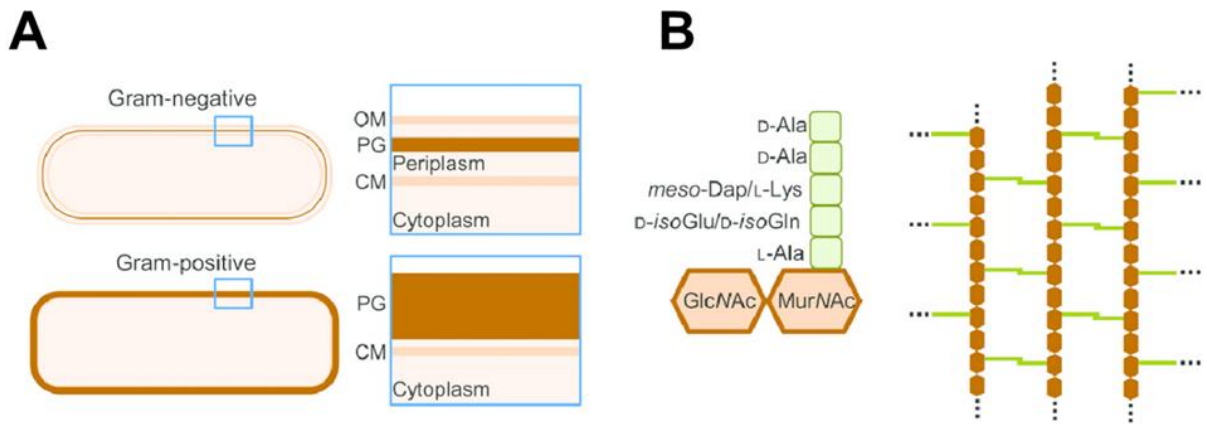

Figure 1.8. Structure of bacterial cell walls. **(A)** Illustrates the cell walls of Gram-negative and Gram-positive bacteria, with the blue box providing an enlarged view of the key components: OM (outer membrane), PG (peptidoglycan), and CM (cell membrane). **(B)** Shows the basic subunit of peptidoglycan consisting of N-acetylglucosamine (GlcNAc) and N-acetylmuramic acid (MurNAc) attached to a stem peptide, with residues labeled according to sequences typically found in Gram-negative (left) and Gram-positive (right) species. Adjacent is a segment of the peptidoglycan matrix with polymerized glycan strands interconnected by cross-linked peptides. Adapted from Egan et al. (2017).

1.3.2. Structure of the endospore wall

The dormancy and heat resistance of endospores mainly stem from the dehydration of the core, where the peptidoglycan wall plays a crucial role in maintaining and potentially attaining this dehydration (Beaman et al., 1986; Koshikawa et al., 1984).

The peptidoglycan of endospores consists of two layers: a thin inner germ cell wall and a thicker outer cortex. During the process of germination, the cortex is degraded, while the germ cell wall remains intact. This germ cell wall, which is structurally similar to the peptidoglycan of vegetative cell walls, subsequently functions as the initial cell wall of the outgrowing endospore (Atrih et al., 1988; Meador-Parton et al., 2000).

The cortex peptidoglycan exhibits several structural changes compared to that in vegetative cells. The most notable modification is the removal of peptide side chains from approximately

50% of the NAM residues, and their subsequent conversion to muramic-δ-lactam (Figure 1.9). This modification involves the cleavage of the peptide through the action of an amidase, followed by the removal of the acetyl group and the subsequent formation of the α-lactam ring by a deacetylase (Gilmore et al., 2004).

Furthermore, an additional 15 to 25% of the NAM residues have their side chains reduced to single L-Alanine residues. This alteration, coupled with the conversion of every other NAM to muramic-δ-lactam, results in a significant decrease in cross-linking within the cortex peptidoglycan. While 33 to 45% of NAM residues in the vegetative cell walls of *B. subtilis* are involved in cross-links, only about 3% of NAM residues in cortex peptidoglycan are cross-linked (Warth et al., 1969; Warth et al., 1972; Dowd et al., 2008; Atrih et al., 1996).

The primary factor influencing endospore dehydration and resistance is the thickness of the peptidoglycan layer, whereas the amount of muramic-δ-lactam and peptide cross-linking do not exhibit a clear correlation with these properties. However, the absence of muramic-δ-lactam does impede germination, which led to the proposal that this structural modification serves as a determinant of specificity for germination-specific lytic enzymes, thereby leaving the germ cell wall intact during germination (Popham et al., 1996; Atrih et al., 1998).

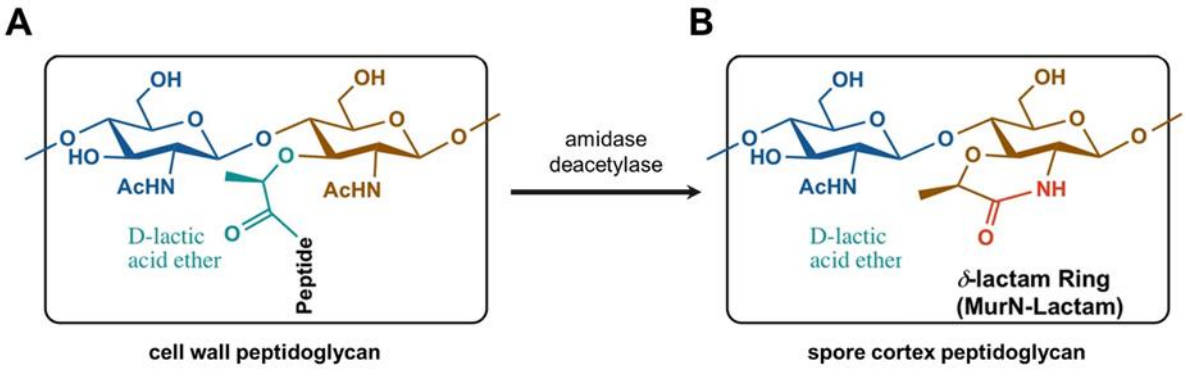

Figure 1.9. Structural comparison of peptidoglycan in vegetative cells/germ cell walls and endospore cortex. Peptidoglycans form a matrix composed of linear glycan chains of alternating N-acetylglucosamine (GlcNAc, blue) and N-acetylmuramic acid (MurNAc, brown) with interlinked short-chain peptides. (A) In vegetative cell walls and the germ cell walls of endospores, short peptides linked to the D-lactic acid (cyan) of MurNAc units cross-link the glycan chains, forming a robust network. (B) In the cortex of endospores, every second NAM unit undergoes complete peptide removal by amidases followed by acetyl group removal by deacetylases, resulting in δ-lactam rings and reduced crosslinking compared to unmodified PG. Adapted from Walter and Mayer (2019).

1.3.3. The role of cell wall hydrolases in peptidoglycan degradation

During bacterial growth and division, there is a constant balance between cell wall degradation and biosynthesis. The processes of elongation and division require both the synthesis and strategic breakdown of peptidoglycan to allow the insertion of new material into the cell wall (Scheffers and Pinho 2005; Typas et al., 2012).

This peptidoglycan remodeling is facilitated by cell wall hydrolases (CWHs), a diverse group of enzymes, and their activity is carefully regulated to maintain cell integrity. These enzymes include glycoside hydrolases that hydrolyze the glycosidic bonds of the glycan chains, and amidases, endopeptidases, and carboxypeptidases that cleave different bonds in the peptide crosslinks. The glycosidases fall into two major groups: N-acetyl-β-D-muramidases, which cleave NAM-to-NAG bonds, and N-acetyl-β-D-glucosaminidases, which cleave NAG-to-NAM bonds. N-acetyl-β-D-muramidases are further classified as lysozymes or lytic transglycosylases (Höltje et al., 1995). Cell wall hydrolases also play a crucial role in cell wall turnover—where up to 50% of the peptidoglycan can be recycled per generation—and in the separation of daughter cells post-division (Höltje et al., 1995).

In bacterial endospores, cell wall hydrolases are essential throughout both the sporulation and germination stages. During sporulation, these enzymes perform several critical functions, including hydrolyzing the asymmetric septum, contributing to the maturation of the endospore cortex, and facilitating the release of the endospore by lysing the mother cell wall (Smith et al., 2000). Furthermore, the degradation of the cortex peptidoglycan during germination is carried out by germination-specific lytic enzymes (GSLEs). GSLEs are further divided into spore cortex-lytic enzymes (SCLEs), which degrade intact cortex peptidoglycan, and cortex fragment-lytic enzymes (CFLEs), which target peptidoglycan fragments resulting from SCLE activity (Makino et al., 2002). Both groups are specific to the muramic-δ-lactam-containing cortex peptidoglycan, ensuring selective cortex degradation while preserving the germ cell wall (Popham et al., 1996; Makino et al., 2002). GSLEs are synthesized during endospore formation and remain inactive within the dormant endospore until the process of germination is initiated (Setlow et al., 2001).

1.4. Aim and outline of the thesis

This study aimed to contribute to the long-term objective of identifying new functional roles of LPMOs by exploring the biochemical and functional properties of those derived from *B. licheniformis* (*Bl*LPMO10A) and *B. spizizenii* (*Bs*LPMO10A). The selection of these LPMOs was partially based on their genomic isolation from chitinases, potentially hinting at alternative functions. While *Bl*LPMO10A is chitin-active and has been structurally characterized by NMR (Courtade et al., 2015; Forsberg, Røhr, et al., 2014; Manjeet et al., 2013), the structure and specificity of the putatively chitin-active *Bs*LPMO10A has remained uncharacterized prior to this study. Building on the recently discovered role of LPMOs in cell wall remodeling in other gram-positive soil bacteria (Zhong et al., 2022), as well as their suggested effect on the germination of *B. subtilis* endospores (Qezellou, 2023), this research sought to further investigate LPMO interactions with cell walls of bacteria and endospores, potentially aiding to uncover novel peptidoglycan degradation pathways.

The methodological approach, illustrated in Figure 1.10, aimed to systematically explore the structure, specificity, and biological roles of the selected LPMOs. Initially, a promoter screening was performed to identify factors influencing LPMO expression in *B. licheniformis*, thereby providing insights into its regulatory mechanisms.

The second part of the study focused on the characterization of *Bs*LPMO10A. To characterize this LPMO, in silico structural elucidation and alignment was performed to contextualize the LPMO within its family and infer substrate specificities, before it was expressed and purified alongside *Bl*LPMO10A in order to verify its putative chitinolytic activity by product analysis. Additionally, potential activity on cellulose was assessed, and substrate-binding assays were performed to determine its specificity and affinity for these substrates.

The final part of the study focused on the potential interactions or activity of LPMOs with cell walls of bacteria and endospores. Methods employed included optical density-based activity assays using washed bacterial cells to assess lytic activity and synergistic effects with lysozymes in cell wall hydrolysis. Additionally, the impact of LPMOs on endospore germination was evaluated through germination assays that utilized DPA-specific fluorescence and optical density to monitor the rate of germination, alongside microscopic analysis and binding assays.

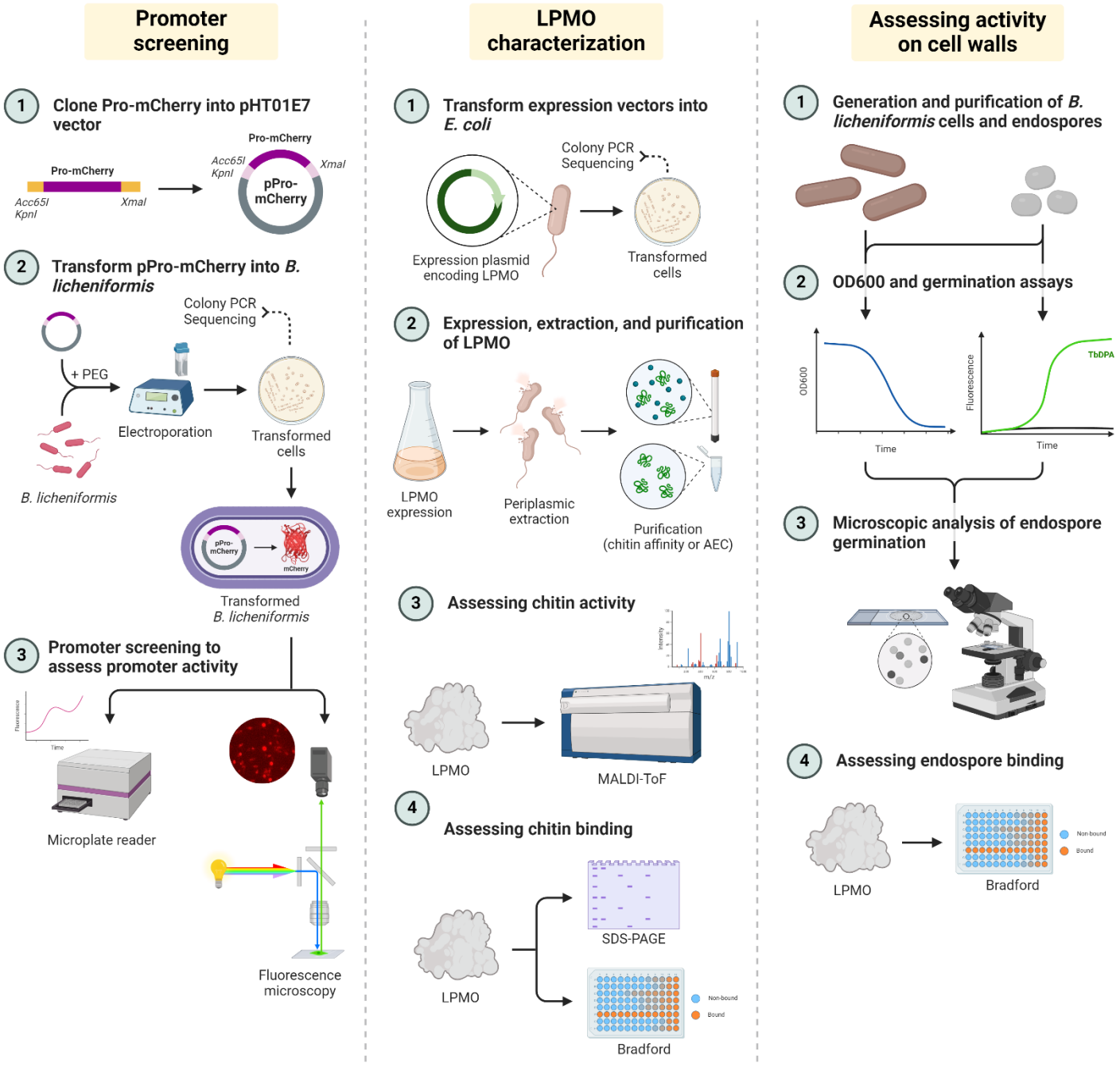

Figure 1.10. Flowchart of the methodological approaches used in this study. Figure created in BioRender.

2. Materials and methods

2.1 Laboratory equipment

Table 2.1. List of laboratory equipment used in this study.

Category	Items	Manufacturer
Agarose gel electrophoresis	Blue Tray; Gel Doc™ EZ Imager; Gel Tray; Mini-PROTEAN® Tetra System; Mini-Sub® Cell GT; PowerPac™ Basic 300 V/400mA/75W Power Supply	Bio-Rad
	Transilluminator	VWR
	Carbon Steel Scalpel Blades; Scalpel Knife Handle	VWR
Anion-exchange chromatography	Äkta Pure™ chromatography system; Fraction collector F9-R; HiTrap™ Q FF anion exchange chromatography column (5 mL)	GE Healthcare, Cytiva
Autoclave	CertoClav Labor-Autoklav CV-EL 12L/18 L	CertoClav
Balance, analytical	Secura®, Sartoius	VWR
Biological safety cabinet	Telstar AV-100	Telstar
Blue-capped bottles	VWR® Laboratory Bottles, 50 mL, 100 mL, 250 mL, 500 mL, 1000 mL	VWR
Bunsen burner	FIREBOY Safety Bunsen Burner	Integra Biosciences
Cell culture tubes	13 mL, 100x16 mm, polypropylene	Sarstedt AG & Co. KG
Cell density photometer	Biochrom Ultrospec™ 10 Cell Density Meter	Harvard Bioscience
Centrifuge bottles	400 mL Polypropylene Bottle Assembly	Beckman Coulter
Centrifuge rotors	JA-10 rotor; JA-20 rotor; J-Lite® JLA-8.1000 rotor	Beckman Coulter
Centrifuge tubes	42 mL Oak Ridge High-Speed PPCO Centrifuge Tubes; CELLSTAR® Centrifuge tubes, 15 and 50 mL	Nalgene; Greiner Bio-One
Chitin affinity chromatography	BioLogic LP chromatography system; Econo-Column® Chromatography Column; Econo-Column® flow adaptor	Bio-Rad
	Chitin Resin (stored in 20% ethanol)	New England Biolabs
Cryo-tubes	Screw cap micro tube, 2 mL, PP	Sarstedt AG & Co. KG
Cuvettes	Disposable cuvette, 1.5 mL; Gene Pulser Electroporation Cuvettes, 0.2 cm gap; UVette® disposable cuvettes	Brand; Bio-Rad; Eppendorf Agilent Technologies
Drigalski spatula		VWR
Erlenmeyer flasks	Duran® Erlenmeyer Flask Glass, 100 mL; Nalgene® Erlenmeyer Flask, baffled, 2 L	Duran; Nalgene
Filters	Filter Upper Cup, 0.22 µm pore size, PES membrane, 250 mL	VWR
	Steritop® 45 mm Neck Size Millipore Express® PLUS 0.22 µm PES membrane, 250 mL; Millipak® Express 40, 0.22 µm PES membrane	Merck Millipore
Fume hood	Waldner MC 6	Waldner
Gene Pulser	Gene Pulser II Porator	Bio-Rad
Ice flake machine		Porkka
Magnetic hotplate stirrer	IKA® RCT classic	IKA
Magnetic stir bar	Bel-Art™ SP Scienceware™ Polygon Spinbar™ Magnetic Stirring Bar without Pivot Ring	Thermo Fisher Scientific
MALDI-ToF Mass spectrometry	MTP 384 target plate ground steel BC; UltrafleXtreme mass spectrometer equipped with a Nitrogen 337-nm laser	Bruker Daltonics

Measuring cylinders	1000 mL, 250 mL, 50 mL	VWR
Microcentrifuge tubes	Axygen® MaxyClear Snaplock Microcentrifuge Tubes, 1.5 mL and 2 mL	Corning
Microplate reader	Varioskan™ LUX multimode microplate reader	Thermo Fisher Scientific
Microscopy	Leica DM750 Microscope; Zeiss LSM 700 Confocal Microscope	Leica Microsystems; Zeiss
	Microscope slides thickness approx. 1 mm; Microscope slide with reaction wells; Cover glasses; Bürker chamber, 0.1 mm depth; Cover glasses for counting chambers and haemacytometers, 0.4 mm; Lens cleaning tissue paper;	Marienfeld
	Certified Molecular Biology Agarose	Bio-Rad
Milli-Q water dispenser	Q-POD® Ultrapure Water Remote Dispenser	Merck Millipore
PCR tubes	Axygen® PCR Tubes and Caps, 0.2 mL	Corning
Petri dishes	Petri dishes, 9 cm	Heger AS
pH-meter	913 pH meter	Metrohm
Pipette, automatic	0.2-2 µL; 2-10 µL; 100-1000 µL; 1-5 mL	Thermo Fisher Scientific
	10-100 µL	VWR
	Finnpipette F1 Multichannel Pipette, 5-50 µL, 8 channels	Thermo Fisher Scientific
Pipette tips	10 µL, 1000 µL; 200 µL; 5 mL	VWR; Sartorius; Thermo Fisher Scientific
	Filter tips; 10 µl, 200 µl, 1000 µl	Sarstedt AG & Co. KG
	Wide Orifice Tips; 200 µL, 1000 µL	VWR
Rotator	Multi RS-60	BioSan
SDS-PAGE	Gel Doc™ EZ Imager; Mini PROTEAN® TGX Stain-Free™ Precast Gels; Mini-PROTEAN® Tetra Cell; Mini-PROTEAN® Tetra System; PowerPac™ Basic 300 V/400mA/75W Power Supply; Stain-Free Tray	Bio-Rad
Spectrophotometer	BioPhotometer® D30	Eppendorf Agilent Technologies
Syringe filter	Filtropur S, PES membrane, 0.2 µm pore size	Sarstedt AG & Co. KG
Syringes	BD Plastipak; 30 mL, 60 mL	Becton Dickinson
Test tubes	VWR® Test tubes without Rim, Thin Walled	VWR
Thermocycler	SimpliAmp™ Thermal Cycler	Thermo Fisher Scientific
Thermomixer	ThermoMixer® C; ThermoTop®	Eppendorf Agilent Technologies
Vacuum manifold	MultiScreen®HTS Vacuum Manifold	Merck Millipore
Vacuum pump	Chemical Duty Pump, 230 V/50/60 Hz	Merck Millipore
Volumetric flasks	1000 mL, 2000 mL, 500 mL	VWR
Vortex mixer	IKA® MS 3 basic	IKA
Water bath	Julabo™ Water Bath	Julabo

2.2 Chemicals

Table 2.2. List of chemicals used in this study.

Chemical	Molecular Formula	Molecular Weight (g/mol)	Manufacturer
Acetic acid, glacial	CH_3COOH	60.05	Merck Millipore
Agarose (SeaKem® LE Agarose)	$C_{24}H_{38}O_{19}$	538.56	Lonza Bioscience
Alanine (L-Alanine)	$C_3H_7NO_2$	89.09	Sigma-Aldrich
Ammonium sulfate	$(NH_4)_2SO_4$	132.14	Sigma-Aldrich
Ampicillin sodium salt	$C_{16}H_{18}N_3NaO_4S$	371.39	Sigma-Aldrich
Ascorbic acid (L-Ascorbic acid)	$C_6H_8O_6$	176.12	Sigma-Aldrich
β-chitin from squid pen, milled, 0.85 mm	$(C_8H_{13}O_5N)n$	~203.19	France-Chitine
Bradford reagent dye (Protein Assay Dye Reagent Concentrate, 1X)	-	-	Bio-Rad
Chloramphenicol	$C_{11}H_{12}Cl_2N_2O_5$	323.13	Sigma-Aldrich
Chloroform	$CHCl_3$	119.38	Sigma-Aldrich
Cobalt(II) chloride hexahydrate	$CoCl_2 \cdot 6H_2O$	237.93	Sigma-Aldrich
Copper(II) chloride dihydrate	$CuCl_2 \cdot 2H_2O$	170.48	Sigma-Aldrich
Copper(II) sulfate pentahydrate	$CuSO_4 \cdot 5H_2O$	249.68	Sigma-Aldrich
Cysteine (L-cysteine)	$C_3H_7NO_2S$	121.16	Sigma-Aldrich
Dihydroxybenzoic acid (DHB) matrix	$C_7H_6O_4$	154.12	Sigma-Aldrich
Dipicolinic acid (2,6-Pyridinedicarboxylic acid)	$C_7H_5NO_4$	167.12	Sigma-Aldrich
Dithiothreitol (DL-Dithiothreitol; DTT)	$C_4H_{10}O_2S_2$	154.25	Sigma-Aldrich
Ethanol, absolute	C_2H_6O	46.07	VWR
Ethylenediaminetetraacetic acid (EDTA)	$C_{10}H_{16}N_2O_8$	292.24	Sigma-Aldrich
Fructose (D-(−)-Fructose)	$C_6H_{12}O_6$	180.16	Sigma-Aldrich
Gallic acid	$C_7H_6O_5$	170.12	Sigma-Aldrich
Glucose (D-(+)-Glucose)	$C_6H_{12}O_6$	180.16	Sigma-Aldrich
Glycerol (85%), sterile	$C_3H_8O_3$	92.09	VWR
Glycogen from bovine liver	$(C_6H_{10}O_5)n$	~162.14	Sigma-Aldrich
Hydrochloric acid, fuming (37%)	HCl	36.46	Sigma-Aldrich
Iron(II) sulfate heptahydrate	$FeSO_4 \cdot 7H_2O$	278.01	Sigma-Aldrich
Isopropyl β-D-1-thiogalactopyranoside (IPTG)	$C_{19}H_{18}O_5S$	358.41	Protein Ark
Kanamycin sulfate	$C_{18}H_{38}N_4O_{15}S$	582.58	Gibco
Magnesium chloride hexahydrate	$MgCl_2 \cdot 6H_2O$	203.3	Sigma-Aldrich
Malachite green	$C_{23}H_{25}ClN_2$	364.91	Merck
Manganese(II) sulfate monohydrate	$MnSO_4 \cdot H_2O$	169.02	Sigma-Aldrich
Mannose (D-(+)-Mannose)	$C_6H_{12}O_6$	180.16	Sigma-Aldrich
Milli-Q® Sterile Water	dH_2O	18.02	Merck Millipore
Phosphoric acid swollen cellulose (PASC)	$(C_{12}H_{20}O_{10})n$	~324.30	Provided by Hanne Berggreen
Potassium chloride	KCl	74.55	Sigma-Aldrich
Safranin	$C_{20}H_{19}ClN_4$	350.85	VWR
Sodium acetate, anhydrous	CH_3COONa	82.03	Sigma-Aldrich
Sodium chloride	NaCl	58.44	VWR
Sodium hydroxide solution	NaOH	40	Honeywell
Sodium molybdate dihydrate	$Na_2MoO_4 \cdot 2H_2O$	241.95	Sigma-Aldrich
Sodium phosphate dibasic	Na_2HPO_4	141.96	Sigma-Aldrich
Sodium phosphate monobasic	NaH_2PO_4	119.98	Sigma-Aldrich
Sulfuric acid	H_2SO_4	98.08	Honeywell
Terbium(III) chloride, anhydrous	$TbCl_3$	263.26	Sigma-Aldrich
Zinc sulfate heptahydrate	$ZnSO_4 \cdot 7H_2O$	287.54	Sigma-Aldrich

2.3 Buffers and stock solutions

Table 2.3. List of buffers and stock solutions used in this study.

Buffer / stock solution	Notes*	Final Concentration	Volume
Alanine (L-Alanine)	178.2 mg L-Alanine	200 mM	10 mL
Ammonium sulfate	264.28 g $(NH_4)_2SO_4$ Stored at room temperature	4 M	500 mL
Ampicillin	500 mg ampicillin sodium salt Sterile filtered (syringe, 0.2 µm) Stored at -20 °C	50 mg/mL	10 mL
Ascorbic acid (L-Ascorbic acid)	17.6 mg L-ascorbic acid Sterile filtered (syringe, 0.2 µm) Stored at -20 °C in 100 µL aliquots	100 mM	1 mL
β-chitin	Provided by Hanne Berggreen	20 g/L	
Chloramphenicol	150 mg chloramphenicol Dissolved in ethanol, absolute Sterile filtered (syringe, 0.2 µm) Stored at -20 °C	15 mg/mL	10 mL
Chloroform-saturated Tris-HCl, pH 8.0	1.9 mL chloroform Dissolved in 100 µL 1 M Tris-HCl (pH 8.0) in a fume hood Vortex before use	50 mM	2 mL
Dipicolinic acid (DPA)	1.67 mg DPA Sterile filtered (syringe, 0.2 µm) Stored at room temperature	1 mM	10 mL
Erythromycin	Provided by Hanne Berggreen	10 mg/mL	
Isopropyl b-D-1-thiogalactopyranoside (IPTG)	Provided by Geir Mathiesen	500 mM	
Kanamycin	0.5 g kanamycin sulfate Sterile filtered (syringe, 0.2 µm) Stored at -20 °C	50 mg/mL	10 mL
Loading buffer, SDS-PAGE	1 mL NuPAGE™ 4X Loading Sample Buffer 400 µL NuPAGE™ 10X Sample Reducing Agent 600 µL dH_2O Stored at 4 °C	2X	2 mL
Magnesium chloride, ($MgCl_2$)	1.0165 g $MgCl_2 \cdot 6H_2O$ Sterile filtered (syringe, 0.2 µm) Stored at 4 °C	100 mM	50 mL
Malachite green	100 mg malachite green	1% (w/v)	10 mL
Metal solution #1	2.78 g $FeSO_4 \cdot 7H_2O$ 4.26 g $CuCl_2 \cdot 2H_2O$ 5.95 g $CoCl_2 \cdot 6H_2O$ 35.94 g $ZnSO_4 \cdot 7H_2O$ 99.66 g $MnSO_4 \cdot H_2O$ 6.05 g $Na_2MoO_4 \cdot 2H_2O$ Sterile filtered (syringe, 0.2 µm) Stored at 4 °C	10X	100 mL
Metal solution #2	2.03 g $MgCl_2 \cdot 6H_2O$ 2.36 g $Ca(NO_3)_2 \cdot 4H_2O$ Sterile filtered (syringe, 0.2 µm) Stored at 4 °C	10X	100 mL
Phosphate buffered saline (PBS)	Provided by Hanne Berggreen	10X	
PEG 6000	20 g polyethylen glycol (PEG) 6000 dH_2O Sterile filtered (syringe, 0.2 µm)	40% (w/v)	50 mL

	Stored at 4 °C		
Phosphoric acid swollen cellulose (PASC)	Provided by Hanne Berggreen	11.5 g/L	50 mL
Sodium acetate buffer, pH 5.6	34.18 g sodium acetate	1 M	250 mL
Sodium chloride, NaCl	292.75 g NaCl Sterile filtered (vacuum filtration, 0.22 µm) Stored at room temperature	5 M	1 L
Spheroplast buffer	171 g D(+)-Saccharose; 10mL 1M Tris HCl, pH 8.0; 0.1 mL 0.5 M EDTA, pH 8.0 Sterile filtered (vacuum filtration, 0.22 µm) Stored at 4 °C	0.5 M; 100 mM; 50 µM	1 L
Terbium(III) chloride	4.26 g $TbCl_3$ Dissolved in sodium acetate buffer (1M, pH 5.6) Sterile filtered (syringe, 0.2 µm) Stored at room temperature	150 mM	10 mL
Tris-acetate-EDTA (TAE) Buffer	Stored at room temperature	1X	50 mL
Tris-glycine-SDS (TGS) Buffer	Stored at room temperature	1X	2 L
Tris-HCl buffer, pH 8.0	60.57 g Tris Base pH adjusted using 37% HCl Sterile filtered (vacuum filtration, 0.22 µm) Stored at room temperature	1 M	500 mL

**Components are dissolved in* dH_2O *to the final volume unless stated otherwise.*

2.4 Agars and media

Table 2.4. List of agars and media used in this study.

Culture medium	Preparation	Components	Supplier	Volume
Agar plates	Dissolve components in approximately 400 mL dH_2OAdjust volume to 500 mL Autoclave at 121°C for 20 minutes Allow cooling to 50-60°C Aseptically add appropriate antibiotic (see Table X) Pour into petri dishes and place lids partly on to prevent condensation Solidify for 30 minutes Invert plates and leave overnight at room temperature to allow proper drying Store inverted at 4°C	7.5 g agar powder Liquid medium components for 500 mL	VWR	500 mL
BHI (brain heart infusion)	Dissolve components in approximately 800 mL dH_2O Adjust volume to 1 L Autoclave at 121°C for 20 minutes Allow cooling to room temperature Store at room temperature	37g BHI broth powder	Oxoid	1 L
LB (lysogeny broth)	Dissolve components in approximately 800 mL dH_2O Adjust volume to 1 L Autoclave at 121°C for 20 minutes Allow cooling to room temperature Store at room temperature	10 g Bacto™ Tryptone 5 g Bacto™ Yeast Extract 10 g NaCl	Gibco (Thermo Fisher Scientific)	1 L

MRS (De Man, Rogosa, Sharpe)	Provided by Hanne Berggreen	52 g/L MRS broth	Oxoid	
MRSSM (MRS + sucrose + $MgCl_2$)	Provided by Hanne Berggreen	52 g/L MRS broth 0.5 M sucrose 0.1 M $MgCl_2$	Oxoid	
S.O.C. (Super Optimal broth with Catabolite Repression)	Pre-mixed from supplier Stored at -20° C		Invitrogen	
Sporulation medium (modified from Voort et al., 2010)	Dissolve dry components in approximately 800 mL dH_2O Adjust volume to 1 L Autoclave at 121°C for 20 minutes Allow cooling to room temperature Add each metal solution separately to avoid precipitation from mixing concentrated Ca(NO3)2 with sulfate ions Store at room temperature	8 g Nutrient Broth powder 10 mL metal solution #1 (1X) 10 mL metal solution #2 (1X)	Difco	1 L

2.5 Plasmids and primers

Table 2.5. List of plasmids and fragments used in this study.

Plasmid	Description	Source	Antibiotic selection*	µg/ml
p*Bs*LPMO10A	pET-26b(+) derivative for inducible expression of *Bs*LPMO10A, signal peptide derived from *Sm*LPMO10A	Addgene	Kan (*E. coli*)	100
pEV	Empty pHT01 vector	MoBiTec	Amp (*E. coli*) ; Cm (*Bacillus* spp.)	100 (solid), 200 (liquid); 15
pHT01E7	pHT01 derivative encoding TfLPMO10A (E7)	Zarah Forsberg	Amp (*E. coli*) ; Cm (*Bacillus* spp.)	100 (solid), 200 (liquid); 15
pPro-mCherry	pHT01 derivative with a promoter-mCherry construct; promoter part composed of the 400 bp region upstream of *Bl*LPMO10A	This study	Amp (*E. coli*) ; Cm (*Bacillus* spp.)	100 (solid), 200 (liquid); 15
p*Bl*LPMO10A	pRSET™B derivative for constitutive expression of *Bl*LPMO10A, signal peptide derived from *Sm*LPMO10A	Zarah Forsberg	Amp (*E. coli*)	100 (solid), 200 (liquid)
pCherry	pSIP401 derivative for inducible expression of mCherry	Solveig Birkedal Wiig	Ery (*E. coli*) ; Ery (*L. plantarum*)	200; 5-10
pCherry-K202E	pSIP401 derivative for inducible expression of mCherry-K202E	This study	Ery (*E. coli*) ; Ery (*L. plantarum*)	200; 5-10

**Abbreviations: Kan (Kanamycin), Amp (Ampicillin), Cm (Chloramphenicol), Ery (Erythromycin).*

Table 2.6. Primers and DNA fragments used in this study.

Primer	Sequence* (5' → 3')	Description	Expected amplicon size	Restriction enzyme
mCherry_F	ggagtatgatt**catATG**AGCAAAGGAGAAGAAGATAAC	Forward primer for amplification of mCherry, In fusion tail to pSIP vector	738 bp	NdeI
mCherry_R	ctgtaatttg**aagctt**TTATTTGTAAAGCTCATCCATTCCGC	Reverse primer for amplification of mCherry, In fusion tail to pSIP vector		HindIII
pHT01_Sek_F	TCAGCCGACTCAAACATCAAA	Forward primer for colony PCR and sequencing pPro-mCherry	1341 bp	
pHT01_Sek_R	TTCAACCATTTGTTCCAGGT	Reverse primer for colony PCR and sequencing pPro-mCherry		
Pro-mCherry_F	gaattagctt**ggtacc**AAGTTTGCCGAGGCCTGC	Forward primer for amplification of Pro-mCherry fragment, In fusion tail to pHT01 vector	1135 bp	Acc65I/ KpnI
Pro-mCherry_R	ggcgggctgc**cccggg**TTATTTGTAAAGCTCATCCATTCCGC	Reverse primer for amplification of Pro-mCherry fragment, In fusion tail to pHT01 vector		XmaI
Pro-mCherry fragment	Supplement 1	400 bp region upstream of *Bl*LPMO10A fused to mCherry (Beilharz et al., 2015), codon-optimized for expression in *B. licheniformis*. In fusion tails to pHT01 vector	1135 bp	Acc65I/ KpnI; XmaI

**Restriction sites are indicated in bold, underlined; tails are indicated in lower case.*

2.6 PCR and cloning reagents

Table 2.7. PCR and cloning reagents used in this study.

Reagent	Supplier
In-Fusion HD Enzyme Premix (5X)	TakaraBio
NEBuffer™ r2.1	New England Biolabs
Q5® Hot Start High Fidelity Master Mix (2X)	New England Biolabs
Quick Ligase (2,000,000 units/mL)	New England Biolabs
Quick Ligase Reaction Buffer (2X)	New England Biolabs
Taq 2x Master Mix	VWR

2.7 Gel electrophoresis reagents

Table 2.8. Agarose and polyacrylamide gel electrophoresis reagents and buffers used in this study.

Purpose	Reagent	Supplier
Agarose gel electrophoresis	Agarose (SeaKem® LE Agarose)	Lonza Bioscience
	DNA Gel Loading Dye 6X (NEB)	New England Biolabs
	peqGREEN DNA/RNA Dye (20,000X)	Peqlab
	Tris-Acetate-EDTA (TAE) buffer (50X)	Thermo Fisher Scientific
SDS-PAGE	NuPAGE™ LDS Sample Buffer (4X)	Thermo Fisher Scientific
	NuPAGE™ Sample Reducing Agent (10X)	Thermo Fisher Scientific
	Tris-Glycine-SDS (TGS) buffer (10X)	Bio-Rad

2.8 Kits

Table 2.9. Kits used in this study.

Kit	Components	Supplier
NucleoSpin® Gel and PCR Clean-up	NucleoSpin® Gel and PCR Clean-up columns Collection tubes, 2 mL Binding buffer (NTI) Wash buffer (NT3) Elution buffer (NE)	Macherey-Nagel
NucleoSpin® Plasmid (NoLid)	NucleoSpin® Plasmid Columns Collection Tubes (2 mL) Resuspension buffer A1 Lysis buffer A2 Neutralization buffer A3 Wash buffer AW Wash Buffer A4 Elution buffer AE	Macherey-Nagel
Qubit™ dsDNA BR Assay	Qubit™ Assay tubes Qubit™ dsDNA BR reagent Qubit™ dsDNA BR buffer Qubit™ dsDNA BR standards	Invitrogen

2.9 Proteins, enzymes and LPMOs

Table 2.10. Proteins and enzymes used in this study.

Category	Name	Manufacturer
Inducer peptide	SppIP	CASLO
Muramidase	Hen-egg white lysozyme (HEWL)	Roche
Protein standard	BSA Molecular Biology Grade (Bovine serum albumin)	New England Biolabs
Restriction enzymes	Acc65I, HindIII, KpnI-HF, NdeI, XmaI	New England Biolabs

Table 2.11. LPMOs used in this study.

Name	Source organism	Produced by	GenBank Accession	PDB ID
BlLPMO10A	*B. licheniformis* DSM13 = ATCC 14580	This study	AAU39477.1	6TWE
BsLPMO10A	*B. spizizenii* TU-B-10	This study	AEP86897.1	N/A
ScLPMO10C **(CelS2)**	*S. coelicolor* A3	Zarah Forsberg	CAB61600.1	4OY7
SmLPMO10A **(CBP21)**	*Serratia marcescens* BJL200	Eirik Kommedal	WP_060560026.1	2BEM

2.10 Standards

Table 2.12. List of standards used in this study.

Standard	Note	Manufacturer
BenchMark™ Protein ladder	Standard, SDS-PAGE	Invitrogen, Thermo Fisher Scientific
Cello-oligosaccharides (A3-A6, 1 mM)	Standard, MALDI-ToF (Glc_{3-6})	Megazyme
Chito-oligosaccharides (A3-A6, 1mM)	Standard, MALDI-ToF ($GlcNAc_{3-6}$)	Megazyme
GeneRuler™ 1 kb DNA Ladder	Standard, agarose gel electrophoresis	Thermo Fisher Scientific

2.11 Software and online tools

Table 2.13. Software and online tools used in this study.

Software/online tool	Purpose	Developer
Basic Local Alignment Search Tool (BLAST)	DNA and protein sequence similarity search	National Library of Medicine
Benchling cloud-based platform	In silico cloning	Benchling
BioCyc Pathway/Genome Database Collection	Genome and metabolic pathway information, alignment in multigenome viewer for genomic context	SRI International
CAZy database	Retrieval of LPMO structure and sequences	Architecture et Fonction des Macromolécules Biologiques (AFMB)
CLC DNA Main Workbench 7	DNA sequencing data analysis	Qiagen
ColabFold version 1.5.5	Protein structure prediction	(Mirdita et al., 2022) Mirdita et al. (2022)
DALI	Protein structure comparison	Holm et al. (2023)
ExPASy ProtParam	Calculations of theoretical pI, molecular mass, and extinction coefficient of proteins	Swiss Institute of Bioinformatics (SIB)
Fiji 2.15.1	Image analysis	National Institutes of Health
FlexControl	MALDI-ToF mass spectrometry	Bruker Daltonics
Foldseek Search Server	Protein structure search	van Kempen et al. (2024)
GenBank® genetic sequence database	Retrieval of protein and nucleotide sequences	National Center for Biotechnology Information
GraphPad Prism 9	Figure generation	GraphPad Software Inc.
Image Lab™, version 6.1.0	Identification and visualization of proteins on gels	Bio-Rad
In-Fusion molar ratio calculator	Calculating optimal amounts of vector and insert for In-Fusion Cloning	Takara Bio
iTOL version 6.9	Visualization of phylogenetic trees	Letunic and Bork (2024)
Jalview 2.11.3.0	Visualization of protein sequence alignments	European Bioinformatics Institute
Job Dispatcher	Sequence analysis tools, multiple sequence alignment, generation of phylogenic trees	European Molecular Biology Laboratory/European Bioinformatics Institute
Leica AirLab version 2.0	Light microscopy imaging	Leica
NEB Tm Calculator, version 1.16.5	Calculating primer annealing temperature	New England Biolabs
NEBioCalculator	Calculating optimal amounts of vector and insert for Quick Ligation Cloning	New England Biolabs
pDRAW32	Plasmid design	AcaClone
PyMOL Molecular Graphics System, version 2.5.3	Visualization of protein structures and protein structure alignments	Schrödinger
SkanIt RE 7.0.2 for Microplate Readers	Microplate-reader control and data-handling	Thermo Fisher Scientific
Unicorn™ 6.4 Software	Protein purification	GE Healthcare, Cytiva
ZEN Microscopy Software	Fluorescence microscopy	ZEISS

2.12 Bacterial strains and cultivation conditions

Bacterial strains were cultured in media as specified in Table 2.14, supplemented with the necessary antibiotics listed in Table 2.5. *E. coli* and *Bacillus* spp. were grown overnight at 37°C in LB or BHI medium with vigorous shaking at 200-220 rpm to maximize oxygenation and nutrient distribution. The induction of *Bacillus* spp. endospores using a specialized sporulation medium is detailed in Section 2.29. *L. plantarum* was cultured at 37°C in MRS medium without agitation to support aerotolerant anaerobic growth. Agar plates for solid media were incubated at 37°C in an inverted position to prevent condensation that might disrupt colony formation and increase contamination risk.

Table 2.14. Overview of bacterial strains and cultivation conditions used in this study.

Species	Medium	Strain	Supplier	Plasmids	Transformed by
Bacillus licheniformis	LB/BHI	MW3	Provided by Marina Aspholm	pEV pPro-mCherry	This study
		DSM13 = ATCC 14580	ATCC	-	-
Bacillus spizizenii	LB/BHI	TU-B-10	Leibniz Institute DSMZ	pEV pPro-mCherry	This study
Escherichia coli	LB/BHI	BL21 Star™ (DE3)	Life Technologies	p*Bl*LPMO10A p*Bs*LPMO10A	This study
		One Shot™ TOP10	Thermo Fisher Scientific	pEV; p*Bl*LPMO10A p*Bs*LPMO10A pCherry-K202E	Zarah Forsberg; This study
		DH5α Mix & Go	Zymo Research	pPro-mCherry	This study
Lactiplantibacillus plantarum	MRS	WCFS1	ATCC	pCherry; pCherry-K202E	Solveig Birkedal Wiig; This study

2.13 Storage of bacteria

Glycerol stocks were prepared by combining 300 µL of sterile 87% glycerol with 1 mL of a bacterial overnight culture in a cryotube. The tube was inverted several and stored at -80°C for long-term preservation. For subsequent cultivation, a sterile toothpick was used to aseptically transfer a small sample from the glycerol stock into 10 mL of growth media (Table 2.14) supplemented with the appropriate antibiotics (Table 2.5).

2.14 Plasmid isolation

Plasmid isolation was performed using the NucleoSpin® Plasmid Kit (Table 2.9) according to the manufacturer's instructions, using sterilized water as eluent. The isolated plasmid DNA was stored at -20°C until use.

2.15 DNA quantification

The QubitTM Fluorometer from Invitrogen was employed following the manufacturer's guidelines to quantify the concentration of isolated plasmid DNA. Briefly, a 1:200 dilution of Qubit reagent in Qubit buffer was added to 1-10 µL sample to a total volume of 200 µL in a Qubit tube, before being measured in a recently calibrated QubitTM Fluorometer.

2.16 Polymerase chain reaction

Polymerase Chain Reaction (PCR) is a fundamental technique in molecular biology for amplifying DNA. It involves three main steps: denaturation (94-98°C), which separates DNA strands; annealing (50-72°C), which allows primers to bind; and elongation (72°C), which extends DNA strands from the primers using a heat-stable polymerase. This cyclic process, typically repeated 25-30 times, leads to exponential amplification with theoretical doubling of the target DNA with each cycle. Master mixes simplify the PCR setup by including essential components like DNA polymerase, nucleotides, buffer, and Mg^{2+} as a cofactor.

2.17 High-Fidelity PCR with Q5® High-Fidelity Polymerase

Q5® High-Fidelity Polymerase was selected for PCR reactions requiring accurate DNA amplification, as it offers ~280-fold lower error rates compared to Taq polymerase (Pezza et al., n.d.).

Materials:

The materials used are described in Table 2.15.

Table 2.15. Q5 High-Fidelity PCR reaction components.

Component	Volume (µL)	Final concentration
Q5® Hot Start High-Fidelity 2x Master Mix (NEB)	25	1x
Forward Primer (10 µM)	2.5	1 µM
Reverse Primer (10 µM)	2.5	1 µM
DNA template	variable	genomic: 0.02-20 µg/mL, plasmid: 0.02-200 ng/mL
Total	To 50 µL	

Protocol:

1. The components given in table 2.5 were mixed in 0.2 mL PCR tubes (Axygen®, Inc. Union City, CA).
2. The tubes were placed in a PCR machine, and a program appropriate for the template and primers was initiated as detailed in Table 2.16.

Table 2.16. Q5 High-Fidelity PCR cycling conditions

Step	Temperature (°C)	Time	Cycles
Initial denaturation	98	30 s	1
Denaturation	98	10 s	
Annealing	50-72*	30 s	25-35
Elongation	72	20-30 s/kb**	
Final elongation	72	2 min	1
Hold	4	∞	

**The annealing temperature (T_a) is generally set 3°C above the T_m of the lower T_m primer. **Duration of the elongation step is adjusted based on the DNA template length, as the Q5 polymerase will elongate approximately a thousand bases in 20-30 seconds.*

2.18 Colony PCR

Colony PCR, used to screen plasmids directly from bacterial colonies, eliminates the need for time-consuming culturing or purification steps. Despite its higher error rate compared to Q5, Taq DNA Polymerase is preferred for its cost-effectiveness and robustness, as it efficiently handles the addition of bacterial colonies or suspensions directly in the PCR reaction.

Materials:

The materials used are described in Table 2.17.

Table 2.17. Colony PCR reaction components

Component	Volume (µL)	Final concentration
Taq 2x Master Mix (VWR)	25	1x
Forward Primer (10 µM)	1	0.2 µM
Reverse Primer (10 µM)	1	0.2 µM
DNA template (one colony)	-	-
dH_2O	to 50	

Protocol:

1. A sterile toothpick was used to transfer a single colony into a PCR tube.
2. For gram-positive species, cell lysis was achieved by either heating the PCR tube in a microwave on high for 1-2 minutes or by adding 10 µL 20 mM Tris-HCl followed by three freeze-thaw cycles: 5 minutes of incubation on ice, microwaving on full power, and 30 seconds of incubation on ice between each cycle.
3. The remaining components listed in Table 2.17 were added to the PCR tubes while maintaining them on ice.
4. The samples were loaded into a PCR machine with a program customized for the template length and primer annealing temperature, as detailed in Table 2.18.

Table 2.18. Colony PCR cycling conditions.

Step	Temperature (°C)	Time	Cycles
Initial denaturation	95	2 min	1
Denaturation	95	20-30 s	
Annealing	50-65*	30 s	25-35
Elongation	72	1 min/kb**	
Final elongation	72	5 min	1
Hold	4	∞	

**The annealing temperature (T_a) is generally set about 5°C below the T_m of the primers. ** Duration of the annealing step is adjusted based on the DNA template length, as the Taq polymerase will elongate approximately 1 kb in 60 seconds.*

2.19 Agarose gel electrophoresis

Agarose gel electrophoresis is a technique used to separate DNA fragments based on their size and charge, relying on the migration of charged DNA molecules through a gel matrix under the influence of an electric field. Agarose, a polysaccharide derived from seaweed, forms a

porous gel matrix when dissolved in buffer solutions like TAE, enabling smaller DNA fragments to migrate more rapidly through its pores compared to larger ones. During electrophoresis, an electric current generates a positively charged anode and a negatively charged cathode, prompting DNA migration towards the anode due to its negative charge arising from its phosphate backbone. Migration rates through the gel are inversely proportional to DNA fragment sizes, resulting in the separation of fragments into distinct bands along the gel, which can be compared to a standard with known sizes. Visualization of these bands is facilitated by fluorescent dyes like ethidium bromide or peqGREEN, which intercalate between DNA bases and fluoresce under UV light, allowing for visualization of DNA bands using a gel documentation system or transilluminator. Specific gel bands can also be excised and purified for downstream applications.

Materials:

- TAE Buffer (1X)
- SeaKem® LE Agarose
- peqGREEN (20,000X)
- DNA Gel Loading Dye (6X)
- GeneRuler™ 1 kb DNA Ladder
- GelDoc EZ imager
- Transilluminator
- Scalpel

Protocol:

1. A 1 µL volume of peqGREEN dye was added to approximately 60 mL of agarose solution.
2. The gel solution was poured into a gel tray with combs to create wells.
3. After solidification for 20-30 minutes, the gel was placed in an electrophoresis chamber filled with 1x TAE buffer.
4. DNA Gel Loading Dye 6X (NEB) was introduced to the DNA to aid in sample loading and for monitoring of the electrophoresis progression.
5. Up to 50 µL of DNA samples and 15 µL of Quick-Load® Purple 1 kb DNA Ladder (NEB) were loaded into the wells.
6. Electrophoresis was conducted at 90V for 30-90 minutes, adjusted based on fragment size for optimal resolution, typically stopping when the dye reached ¾ of the gel length.
7. Visualization of the resulting DNA bands was done using the GelDoc EZ imager.
8. To obtain specific fragments for downstream applications, gel pieces containing the target DNA were excised with a scalpel while visualized on a transilluminator, and were either used immediately or stored in Eppendorf tubes at -20°C for future purification.

2.20 Extraction and purification of DNA fragments from PCR reaction and agarose gels

To purify DNA fragments from PCR reactions and excised agarose gel pieces, the NucleoSpin® Gel and PCR Clean-up Kit from MACHEREY-NAGEL was used according to the manufacturer's recommendations, using distilled water as eluent. The purified DNA fragments were subsequently used in various downstream applications, such as sequencing or cloning.

2.21 DNA digestion with restriction enzymes

Restriction enzymes, or restriction endonucleases, are essential tools in molecular cloning. These enzymes originate from bacteria and archaea, where they cleave foreign DNA at specific sites typically ranging from 4 to 8 base pairs. This action produces either blunt or cohesive ends, the latter referring to overhanging, single-stranded DNA sequences. In traditional molecular cloning, these cohesive ends facilitate the precise insertion of DNA fragments into vectors via complementary base pairing. To ensure the accurate orientation of the fragment, double digestion using two different restriction enzymes is a common practice.

Materials:

The materials used are described in Table 2.19.

Table 2.19. DNA digestion reaction components.

Component	Volume (µL)	Final concentration
Restriction enzyme 1 (10,000 U/mL)	2.5	500 U/mL
Restriction enzyme 2 (10,000 U/mL)	2.5	500 U/mL
Compatible restriction buffer (10x)	5	1x
DNA	Variable	<20 µg/mL
dH_2O	Up to 50	

Protocol:

1. A total volume of 50 µL was prepared by combining the components as specified in Table 2.19 in 1.5 mL Eppendorf tubes. The specific combinations of vectors, restriction enzymes and restriction buffer used in this study are outlined in Table 2.20.
2. The reaction mixture was incubated in a 37°C water bath for 1.5 to 3 hours.
3. Successful digestion was verified by loading digested samples onto a 1-1.2% agarose gel (Section 2.19).
4. The appropriate band corresponding to the target fragment was excised and purified (Section 2.20).

Table 2.20. Specific restriction enzyme and buffer combinations for double digest of plasmids

Plasmid/fragment	Restriction Enzyme	Buffer
pHT01	Acc65I, XmaI	r2.1
pSIP401	HindIII, NdeI	r2.1

2.22 Cloning

Molecular cloning involves insertion of a specific DNA sequence, often a gene of interest, into a vector such as a plasmid. The resulting recombinant DNA construct is then introduced into a host organism, such as bacteria or yeast, where it undergoes replication, generating multiple copies of the inserted gene. Furthermore, this process enables the manipulation and study of specific DNA sequences for various applications, including gene expression studies, protein production, functional analysis of genes, and genetic engineering.

2.22.1 In-Fusion® Cloning

In-Fusion cloning is a molecular cloning technique that enables the seamless insertion of a DNA fragment into a plasmid vector through homologous recombination, eliminating the need for ligase. The target DNA is amplified via PCR using primers that include a 15 base pair overlap with the ends of a vector linearized by digestion, ensuring compatibility for recombination. The resulting fragment is combined with the linearized vector in a reaction containing the In-Fusion enzyme mix. These enzymes facilitate joining of the overlapping ends of the insert and the vector through in vitro homologous recombination. Subsequently, the recombinant DNA is introduced into competent *E. coli cells* through transformation, and successful transformants are selected on antibiotic-containing media.

Materials:

The materials used are described in Table 2.21.

Table 2.21. In-Fusion cloning reaction components

Component	Volume (µL)	Final concentration
5X In-Fusion HD Enzyme Premix	2	1x
Purified PCR fragment (insert DNA)	x	2:1; < 20 µg/mL
Linearized vector (backbone DNA)	x	
dH_2O	to 10	

Protocol:

1. The recommended amount of DNA for a 2:1 insert-to-vector molar ratio was calculated using the online In-Fusion Molar Ratio Calculator (Table 2.13).
2. The components listed in Table 2.21 were thoroughly mixed in a PCR tube at room temperature.
3. The reaction mix was incubated for 15 minutes at 50°C in a thermocycler.
4. The reaction was placed on ice and 2 µL was immediately transformed into *E. coli* (Section 2.23). Alternatively, the reaction was stored at -20°C until transformation.

2.22.2 Quick ligation

Quick ligation cloning is a refined version of traditional ligase-dependent cloning of DNA fragments into linearized plasmid vectors. Initially, both the vector and the DNA fragment are treated with specific restriction enzymes to produce compatible cohesive ends. These ends are then efficiently joined in a ligation reaction facilitated by T4 DNA ligase, which effectively catalyzes the formation of phosphodiester bonds between the cohesive ends.

Materials:

The materials used are described in Table 2.22.

Table 2.22. Quick ligation reaction components.

Component	Volume (µL)	Final concentration
Quick Ligase Reaction Buffer (2x)	10	1x
Purified PCR fragment (insert DNA)	x	2:1; 1-10 µg/mL
Linearized vector (backbone DNA)	x	
Quick Ligase (2,000,000 units/mL)	1	200,000 units/mL
dH_2O	to 20	

Protocol:

1. The NEBioCalculator (Table 2.13) was utilized to calculate the recommended amount of DNA for a 2:1 insert-to-vector molar ratio.
2. The components specified in Table 2.22 were thoroughly mixed in a PCR tube.
3. The sample was incubated for five minutes at room temperature.
4. The reaction was placed on ice, and 2 µL was immediately utilized for *E. coli* transformation (Section 2.23). Alternatively, the reaction was stored at -20°C until transformation.

2.23 Transformation of *E. coli*

The transformation of *E. coli* is essential for introducing plasmids into bacterial hosts, necessary for plasmid amplification and protein expression. This study employed *E. coli* strains TOP10 and Mix & Go DH5α for plasmid amplification, alongside *E. coli* BL21 for protein expression. Each strain was transformed following the manufacturers' protocols, which include a heat shock step to facilitate DNA uptake by inducing transient pores in the cell membrane. After DNA addition, a preincubation step allows cells to recover and express antibiotic resistance genes encoded by the vector, which is essential before spreading on selective media. Notably, Mix & Go DH5α cells are designed to bypass the need for heat shock and preincubation, which streamlines the process by enabling the direct addition of DNA and immediate plating. The protocol for TOP10 is detailed as a representative example.

Materials:

- One Shot™ TOP10 Chemically Competent *E. coli*
- Ligation mixture/purified plasmid
- S.O.C. medium
- Agar plates supplemented with appropriate selection antibiotics (Table 2.5)

Protocol:

1. A vial of One Shot® competent cells was thawed on ice.
2. Plasmid DNA ranging from 1 to 5 µL (10 pg to 100 ng), or 2 µL of ligation mixture, was added to the cells. The vial was gently tapped to ensure thorough mixing.
3. The cells were incubated on ice for 30 minutes.
4. The vial was quickly transferred to a 42°C water bath for 30 seconds to induce heat shock.
5. Immediately following heat shock, the cells were placed back on ice for 2 minutes.
6. Aseptically, 250 µL of pre-warmed S.O.C. medium was added, and the vial was incubated at 37°C with 200 rpm shaking for 1 hour.
7. Subsequently, 50-100 µL of the cell suspension was spread onto agar plates supplemented with the appropriate antibiotics and incubated overnight at 37°C.

   Note: If no transformants were observed, the remaining cell suspension was stored at room temperature overnight. A new plate was inoculated with 50-100 µL the following day.

2.24 Sequencing of plasmids

Sanger sequencing was used to determine the nucleotide sequences of specific regions within plasmids that contained cloned DNA inserts. This method served to confirm successful cloning and to provide crucial genetic information, such as the identification of mutations. Sanger sequencing operates through the cyclic incorporation of chain-terminating dideoxynucleotides (ddNTPs) by DNA polymerase during in vitro DNA replication. Each ddNTP is tagged with a unique fluorescent dye, enabling the sequential reading of emitted colors to deduce the DNA sequence. The sequencing service was provided by Eurofins Genomics (Moss, Norway). Before submission, each plasmid was prepared by combining the plasmid with a specific primer in 1.5 mL Eppendorf tubes, as outlined in Table 2.23. Upon receiving the sequencing results, bioinformatics analysis was conducted using the CLC DNA Main Workbench 7 software (Table 2.13).

Table 2.23. Plasmid sequencing preparation.

Component	Volume (µL)	Final concentration
Plasmid DNA (approximately 500 ng)	Variable	~45 µg/mL
10 µM primer specific to the region*	2.5	2.3 µM
dH_2O	to 11	

2.25 MIC determination

MIC determination via the microdilution method was conducted for *B. licheniformis* to establish the minimum inhibitory concentration (MIC) of chloramphenicol required for

inhibiting the growth of wild-type strains. This determination was essential for the selection of transformants, as chloramphenicol served as the selection antibiotic for the vectors pEV and pPro-mCherry in *B. licheniformis*.

Materials:

- Liquid culture of *B. licheniformis* MW3
- LB medium
- Chloramphenicol stock solution (50 mg/mL)
- Sterile 96-well plate

Protocol:

1. Chloramphenicol was diluted to 100 µg/mL in LB medium.
2. Varied volumes of the chloramphenicol solution were added in triplicates to wells of a 96-well plate to achieve final concentrations ranging from 0 to 45 µg/mL in 5 µg/mL increments.
3. LB medium was added to each well to achieve a volume of 195 µL.
4. Each well was inoculated with 5 µL of the overnight culture of the respective strain.
5. The plate was statically incubated overnight at 37°C.
6. The minimum inhibitory concentration was defined as the lowest concentration of chloramphenicol that successfully inhibited bacterial growth.

2.26 Transformation of *L. plantarum*

Transformation of *L. plantarum* WCFS1 with the vector pCherry-K202E was performed to assess the fluorescence signal of a K202E mutant variant of the mCherry fluorescent protein.

Materials:

- Electrocompetent *L. plantarum* WCFS1 cells (provided by Hanne Berggreen)
- Purified plasmid
- Electroporation cuvette (0.2 cm, pre-chilled)
- Gene Pulser
- MRSSM medium (Table 2.4)
- MRS agar plate supplemented with the appropriate selection antibiotics (Table 2.5)

Protocol:

1. An aliquot of electrocompetent *L. plantarum* cells was thawed on ice.
2. 2 µL plasmid was added to the cells. The tube was gently tapped to ensure thorough mixing.
3. The mixture was incubated on ice for 5 minutes.
4. The cells were transferred to a pre-chilled 0.2 cm electroporation cuvette.

5. Electroporation was conducted utilizing a Gene Pulser with a single pulse of 1.5 kV, a resistance of 400 Ω, and a capacitance of 25 μF.
6. The cells were immediately supplemented with 950 μL of cold MRSSM medium, before being transferred to a sterile Eppendorf tube and incubated at 37°C for 2 hours in a static incubator.
7. Following incubation, 50-100 μL was plated on LB agar containing appropriate selection antibiotics.

2.27 Transformation of *B. licheniformis*

An optimized transformation protocol was developed focusing on *B. licheniformis* MW3, which was chosen for its enhanced transformation efficiency compared to *B. licheniformis* DSM13 (Bianca Waschkau et al., 2008). The protocol involves both the preparation of electrocompetent cells and the subsequent steps for the optimized transformation process.

2.27.1 Preparation of electrocompetent *B. licheniformis* MW3

The preparation of electrocompetent *Bacillus* cells involved a general process designed to maximize transformation efficiency through electroporation.

Materials:

- *B. licheniformis* MW3 or *B. spizizenii* TU-B-10
- LB medium
- BHI medium
- Baffled flasks (25 mL and 200 mL)
- 50 mL falcon tubes
- Sterile water, 4C
- 40% (w/v) PEG 6000 solution, freshly prepared, 4°C

Protocol:

1. An overnight culture was initiated by inoculating a glycerol stock of *B. licheniformis* MW3 into 25 mL of LB medium in a baffled flask.
2. The culture was incubated at 37°C with shaking at 200 rpm.
3. After overnight growth, 2 mL of the culture was transferred to 200 mL of BHI medium in a baffled flask and incubated at 37°C with shaking at 200 rpm.
4. The OD_{600} of the culture was monitored regularly using a spectrophotometer until it reached the early log phase with an OD_{600} of approximately 0.9.
5. The culture was divided into four 50 mL falcon tubes and centrifuged at 4°C and 4000 x g for 15 minutes.
6. The supernatant was discarded, and each pellet was resuspended in 40 mL of sterile room temperature water.

7. Centrifugation was repeated at 4°C and 4000 x g for 15 minutes.
8. Step 6-7 was repeated two more times.
9. Each pellet was resuspended in 8 mL of freshly prepared ice cold 40% (w/v) PEG 6000 and centrifuged at 4°C and 4000 x g for 15 minutes.
10. The pellets were subsequently resuspended in 100 µl of 40% (w/v) PEG 6000, and aliquots of 80 µl were transferred to 1.5 mL Eppendorf tubes.
11. The Eppendorf tubes were stored at -80°C for later use.

2.27.2 Transformation of electrocompetent *B. licheniformis* MW3

The protocol used for the transformation of electrocompetent *B. licheniformis* MW3 with vectors pEV and pPro-mCherry by electroporation is detailed below.

Materials:

- Electrocompetent *B. licheniformis* MW3 cells (Section 2.27.1)
- Purified plasmid
- Electroporation cuvette (0.2 cm, pre-chilled)
- Gene Pulser
- S.O.C. medium (room temperature)
- 13 mL cell culture tube
- BHI agar plate supplemented with the appropriate selection antibiotics (Table 2.5)

Protocol:

8. An aliquot (80 µL) of the electrocompetent *B. licheniformis* MW3 cells was thawed on ice until the last ice crystal disappeared.
9. 2 µL (0.5 µg) plasmid was added to the cells. The tube was gently tapped to ensure thorough mixing.
10. The mixture was incubated on ice for 5 minutes.
11. The cells were transferred to a pre-chilled 0.2 cm electroporation cuvette.
12. Electroporation was conducted utilizing a Gene Pulser with a single pulse of 1.4 kV, a resistance of 400 Ω, and a capacitance of 25 µF, resulting in a time constant of approximately 9.8 ms.
13. The cells were immediately supplemented with 500 µL of room temperature S.O.C. medium, before being transferred to a cell culture tube and incubated at 37°C and 200 rpm for 4-5 hours.
14. Following incubation, 100-150 µL was plated on LB agar containing appropriate selection antibiotics.

    Note: If no transformants were observed, the remaining cell suspension was stored at room temperature overnight. A new plate was inoculated with 100-150 µL the following day.

2.28 Growth curve analysis with simultaneous fluorescence monitoring

Growth curve analysis with simultaneous fluorescence monitoring was conducted for both *B. licheniformis* and *L. plantarum* in order to quantify mCherry expression under the control of various promoters in order to assess promoter activity or compare the strength of fluorescence signals.

2.28.1 Growth curve analysis of *B. licheniformis*

Growth curves with simultaneous fluorescence monitoring were generated for mutants of *B. licheniformis* MW3 across various liquid media compositions, including LB, BHI, 2xSG, and LB supplemented with 2% of glycogen, glucose, fructose, or mannose.

Materials:

- Overnight cultures of bacterial strains
- Liquid media
- Sterile 96-well microplate
- Varioskan™ LUX multimode microplate reader

Protocol:

1. The optical density of each overnight culture was standardized to OD_{600} = 0.2 using the corresponding liquid medium.
2. 200 µL of the standardized inoculum from each strain was added to wells of a sterile 96-well microplate. Control wells containing only growth medium were included.
3. Continuous monitoring was performed using a Varioskan™ LUX multimode microplate reader, which was maintained at 37°C with continuous shaking at 180 rpm between readings. Optical density (OD) measurements at 600 nm and fluorescence measurements (excitation at 587 ± 12 nm, emission at 620 nm) were recorded at 15-minute intervals over a 24-hour period.

2.28.2 Growth curve analysis of *L. plantarum*

The pSIP expression vector is commonly utilized for protein expression in *LactoBacillus* spp., featuring an inducible promoter system regulated by an external peptide signal, sppIP. This configuration allows for precise control over gene expression levels. Growth curve experiments with continuous monitoring of mCherry fluorescence were conducted with *L. plantarum* to compare the fluorescence intensities of different mCherry fluorescent proteins.

Materials:

- Overnight cultures of bacterial strains
- Liquid media
- 15 mL tubes
- sppIP
- Sterile 96-well microplate
- Varioskan™ LUX multimode microplate reader

Protocol:

1. *L. plantarum* strains were grown at 37°C overnight in MRS medium containing appropriate antibiotics.
2. Overnight cultures were diluted in 10 mL prewarmed MRS medium to an OD_{600} of 0.13-0.15.
3. The cultures were incubated at 37°C until they reached an OD_{600} of 0.3, and gene expression was induced with 25 ng/mL SppIP.
4. 200 µL of each culture was added to wells of a 96-well microplate. Control wells containing only growth medium were included.
5. Continuous monitoring was performed using a Varioskan™ LUX multimode microplate reader, which was maintained at 37°C. OD measurements at 600 nm and fluorescence measurements (excitation at 587 ± 12 nm, emission at 620 nm) were recorded at 15-minute intervals over a 20-hour period.

2.29 Generation and purification of bacterial endospores

This protocol describes a method for cultivating endospores from *B. licheniformis*, adapted from the procedure outlined by Løvdal et al. (2013), which induces spore formation through nutrient depletion.

Materials:

- Glycerol stock of *B. licheniformis* DSM 13 */ B. spizizenii* TU-B-10
- Sporulation medium (Table 2.4)
- Sterile ice-cold H_2O
- Sterile 250 mL and 2 L baffled Erlenmeyer flasks
- 50 mL centrifugation tubes

Protocol:

1. 20 mL of sporulation medium was inoculated from a glycerol stock and incubated for 6 hours at 37°C.
2. Subsequently, 10 mL was transferred to 200 mL sporulation medium in a 2 L baffled Erlenmeyer flask.

3. The culture was incubated at 37°C for 24 hours for *B. spizizenii* or 3 days for *B. licheniformis*, after which they were regularly checked under a phase contrast microscope until >80% spores were observed.
4. The culture was heat-shocked at 65°C in a static incubator for 30 minutes to eliminate vegetative cells.
5. Endospores were harvested by centrifugation in 500 mL tubes at 6000 x g for 10 minutes at 4°C.
6. The resulting pellet was resuspended in 50 - 100 mL sterile H_2O and transferred to 50 mL centrifugation tubes.
7. At least three washes with 20-50 mL sterile H_2O were performed by centrifugation at 4500 x g for 15 minutes at 4°C, gradually increasing the volume to minimize spore loss.
8. After the final wash, the pellet was resuspended in 5 mL sterile H_2O and stored at 4°C.
9. The number of endospores in the resulting solution was quantified by measuring the OD_{600} and inspecting the spore count using a Bürker counting chamber (Section 2.29.1).

2.29.1 Quantification of bacterial endospores by hemocytometer

The Bürker chamber is a type of hemocytometer that was used as a reliable method for quantifying *Bacillus* spp. endospores.

Materials:

- Endospore suspension
- PBS Buffer (1x, pH 7.4)
- Bürker chamber
- Coverslip (0.4 mm)
- Phase contrast microscope

Protocol:

1. A 10,000x dilution of the endospore solution was prepared in PBS.
2. The Bürker chamber and cover glass were cleaned with ethanol and allowed to air dry completely.
3. A 0.4 mm thick cover glass was carefully positioned atop the counting chamber. To secure the cover glass, a small droplet of water was applied to each corner.
4. 10 µL of the diluted endospore suspension were applied to the counting chamber.
5. The endospores were allowed to settle before microscopic counting within the 0.05 x 0.05 mm squares was performed using a 40x objective lens. Endospores overlapping with the top and left borders of the squares were included in the count, while those overlapping with the bottom and right borders were excluded.
6. The counting process was replicated three times using independent dilutions of each endospore suspension.
7. The hemocytometer and cover glass were cleaned with ethanol.

8. Endospore density was determined using Equation 1.

$$(1)\quad Endospores\ per\ mL\ = \frac{Average\ endospores\ counted\ per\ square}{Volume\ of\ square\ (mm^3) \cdot 10^{-3}\ mL/mm^3}\ \cdot\ dilution\ factor$$

2.29.2 Schaeffer-Fulton endospore staining

The Schaeffer-Fulton method capitalizes on the differential staining properties of endospores and vegetative cells. Endospores, being highly resistant structures, are practically impenetrable to most chemicals. In this method, the primary stain is malachite green, which is driven into the endospores using heat. After cooling down, vegetative cells can be decolorized with water as malachite green has low affinity for cellular material, while the stain will be kept inside the endospores. Safranin can then be used as counterstain to give color to the vegetative cells. As a result, endospores retain the malachite green and appear green/blue, while vegetative cells appear red/pink.

Materials:

- Endospore suspension
- Microscope slide
- Malachite green (1% w/v)
- Bunsen burner
- Water bath
- Light microscope

Protocol:

1. A bacterial smear was prepared on a microscope slide and allowed to air-dry completely.
2. The dried smear was heat-fixed by gently passing the slide through the flame of a Bunsen burner several times, ensuring the proper adhesion of bacterial cells and endospores to the glass slide.
3. The heat-fixed smear was covered with a piece of porous paper.
4. The slide was flooded with a 1% (w/v) malachite green solution while being suspended cell-side up over a water bath, and steamed for about 5 minutes. Additional malachite green solution was continuously added to compensate for evaporation.
5. The slide was then allowed to fully cool before being rinsed with water to remove excess stain.
6. The slide was counterstained with safranin solution for approximately 1 minute, before rinsing with water to remove excess safranin.
7. The prepared slide was visualized under a light microscope, revealing green/blue endospores and red/pink vegetative cells.

2.30 Fluorescence microscopy

Fluorescence microscopy was utilized to interrogate the expression of mCherry within bacterial cells and endospores, enabling the visualization of fluorescent proteins within cellular environments. To immobilize the cells and ensure their stability during imaging, they were added into a thin layer of microscopy-grade agarose gel.

Materials:

- Zeiss LSM 700 Confocal Microscope
- Bacterial cultures
- PBS (1x)
- Molecular biology-grade agarose
- Microscope slide with reaction wells
- Cover glass

Protocol:

Protocol for sample preparation

1. Optical density at 600 nm (OD_{600}) of bacterial cultures was measured.
2. 500 µL of cultures corresponding to an OD_{600} of 1 was harvested by centrifugation at 5000 x g for 3 minutes.
3. The resulting pellets were washed with 500 µL of PBS and centrifuged again at 5000 x g for 3 minutes.
4. Cells were resuspended in 50 µL of PBS.

Protocol for fluorescence microscopy

1. Molecular biology-grade agarose (1.2% w/v) was dissolved in 10 ml of 1x PBS by repeated heating in a microwave. The solution was used immediately or stored in a water bath at 55°C until use, for up to 1-2 days.
2. Approximately 600 µL of the agarose solution was applied onto a multi-well microscopy slide.
3. Pressure was applied with a blank slide, and the mixture was allowed to set for 30 seconds to 1 minute.
4. The blank slide was gently removed to form a thin agarose layer.
5. 0.4 µL of cell suspension was added to each well on the multi-well slide.
6. The suspension was allowed to dry for less than 1 minute before long cover slips were positioned over the wells.
7. Pressure was applied to ensure proper adherence and remove air bubbles.
8. The slide was observed under suitable filter settings to visualize fluorescent cells.

2.31 Sodium dodecyl sulphate polyacrylamide gel electrophoresis

Sodium dodecyl sulfate polyacrylamide gel electrophoresis (SDS-PAGE) is a widely used technique for separating proteins based on their size. It serves various purposes, including protein detection, assessing sample purity, and estimating relative protein concentrations by comparing band intensities. The process involves denaturing proteins under reducing conditions, disrupting their three-dimensional structure to yield linearized forms. Denaturation is achieved by the reduction of disulfide bonds by the reductant dithiothreitol (DTT), followed by boiling with an anionic detergent like sodium dodecyl sulfate (SDS). SDS molecules uniformly bind to denatured proteins, imparting a negative charge proportional to their size. In the polyacrylamide gel, proteins migrate towards the anode, with smaller proteins migrating faster through the gel network. A protein ladder serves as a reference for band size estimation. The use of Stain-Free technology eliminates the need for traditional staining methods, where direct visualization of proteins within the gel can be achieved using UV light in a gel documentation system.

Materials:

- SDS-PAGE loading buffer (Table 2.3)
- Mini-PROTEAN® Tetra Electrode Assembly
- Mini-PROTEAN® TGX Stain-Free™ Gel and cassette
- Mini-PROTEAN® Tetra Cell
- 1X Tris-Glycine-SDS (TGS) buffer
- BenchMark™ Protein Ladder
- 1.5 mL Eppendorf or PCR tubes
- PowerPac3000 power supply
- Gel Doc™ EZ Imager
- Stain-Free Sample Tray

Protocol:

1. Equal volumes (1:1) of protein solution and SDS-PAGE sample buffer were combined in 1.5 mL Eppendorf or PCR tubes.
2. The protein-sample buffer mixture underwent denaturation at 95-100 °C for 10 minutes in a heat block or thermocycler to ensure complete protein denaturation.
3. Electrophoresis was performed using a Mini-PROTEAN® TGX Stain-Free™ Gel and cassette, mounted in a Mini-PROTEAN® Tetra Electrode Assembly.
4. The assembly was placed within a Mini-PROTEAN® Tetra Cell, filled with 1X Tris-Glycine-SDS (TGS) buffer in both internal and external chambers. Fresh buffer was used in the internal chambers to ensure optimal performance and minimize contamination, while pre-used buffer was used in the external chamber.

5. For gel application, 5-15 µL of BenchMark™ Protein Ladder and 10-20 µL of prepared protein samples were loaded into designated wells on the gel.
6. Electrophoresis was conducted at 270 V for 19 minutes using a PowerPac3000 power supply.
7. Upon completion, the gel was transferred to a Stain-Free Sample Tray for visualization using the Gel Doc™ EZ Imager.

2.32 Protein expression in *E. coli* BL21

Expression of LPMOs was performed through heterologous expression in *E. coli* BL21, transformed with vectors encoding *Bl*LPMO10A and *Bs*LPMO10A behind a signal peptide derived from *Serratia marcescens* (*Sm*LPMO10A). This signal peptide serves to direct the LPMOs to the periplasm, leveraging the periplasmic space present in gram-negative bacteria like *E. coli* for subsequent protein extraction via osmotic shock. The choice of using the signal peptide from *Sm*LPMO10A instead of the native signal peptides of the LPMOs was based on its known functionality. The vector carrying *Bl*LPMO10A (pRSET™B) facilitated constitutive expression, whereas the vector harboring *Bs*LPMO10A (pET-26b(+)) necessitated induction with isopropyl β-D-1-thiogalactopyranoside (IPTG). IPTG is a commonly used inducer that stimulates the expression of target proteins under the control of an inducible promoter.

Materials:

- Glycerol stocks containing *E. coli* BL21 transformed with pRSET™B_*Bl*LPMO10A and pET-26b(+)_*Bs*LPMO10A
- LB medium
- Ampicillin stock solution (50 mg/mL)
- 2 L baffled Erlenmeyer flask
- IPTG stock solution (1 mM)

Protocol:

Protocol for constitutive expression

1. A glycerol stock of *E. coli* BL21 carrying the pRSET™B_*Bl*LPMO10A plasmid with constitutive expression was used to inoculate 0.5 L LB medium supplemented with 100 µg/mL ampicillin in a 2 L baffled Erlenmeyer flask.
2. The culture was incubated at 37°C with shaking at 200 rpm for approximately 18 hours.
3. The culture was harvested by centrifugation at 4,000 x g for 20 minutes at 4°C in 500 mL centrifuge bottles.

Protocol for inducible expression

1. A glycerol stock of *E. coli* BL21 carrying the pET-26b(+)_*Bs*LPMO10A plasmid with inducible expression were cultured in 20 mL liquid BHI or LB overnight with 100 µg/mL ampicillin in a 100 mL Erlenmeyer flask.
2. 2 mL of the overnight culture transferred to 0.5 L pre-warmed LB medium supplemented with the appropriate selection antibiotics in a 2 L baffled Erlenmeyer flask and incubated at 37°C for 6 hours.
3. At the exponential phase (OD_{600} = 0.6-1), IPTG was added to a final concentration of 0.4 mM to induce protein expression.
4. The culture was further incubated for 6 hours at 37°C.
5. The culture was harvested by centrifugation at 4,000 x g for 20 minutes at 4°C in 500 mL centrifuge bottles.

2.33 Periplasmic extraction of proteins expressed in *E. coli* BL21

Following the expression of LPMOs in *E. coli* BL21, osmotic shock was employed to facilitate the selective release of periplasmic proteins, including the LPMOs. The process was initiated by immersing the cells in a hypertonic, high-sucrose solution supplemented with EDTA, prompting water efflux. This causes the cytoplasmic membrane to contract and the periplasmic space to expand, as the outer membrane is retained by the cell wall. EDTA plays a crucial role by chelating divalent cations that are critical for the stability of the outer membrane, thereby increasing its permeability. Subsequently, a hypotonic $MgCl_2$ solution is introduced, reversing the initial osmotic conditions and causing water to re-enter the cells. This rapid water influx drives the periplasmic proteins through the compromised outer membrane into the external medium, while the Mg^{2+} ions help stabilize cellular structures to prevent cell lysis. This technique not only ensures the efficient release of periplasmic proteins but also preserves cell integrity, thereby avoiding contamination from cytoplasmic components. While the periplasmic extract is the primary focus for obtaining periplasmic proteins, the sucrose fraction collected after centrifugation may also contain periplasmic proteins released due to the EDTA-mediated weakening of the outer membrane.

Materials:

- Harvested *E. coli* BL21 cells expressing *Bl*LPMO10A and *Bs*LPMO10A
- Ice-cold spheroplast buffer (Tris-buffered sucrose solution containing EDTA)
- Ice-cold MgCl2 (20 mM)
- Filter cup (0.22 µm)

Protocol:

1. Harvested pellets of *E. coli* BL21 expressing *Bl*LPMO10A and *Bs*LPMO10A were resuspended in 120 mL of ice-cold spheroplast buffer using a 5 mL pipette, while being kept on ice.
2. The resuspended pellets were transferred to 50 mL tubes and centrifuged at 8,000 x g for 20 minutes.
3. The supernatant, constituting the sucrose fraction, was retained and stored at 4°C for future analysis.
4. The pellet was incubated at room temperature for 30 minutes.
5. Subsequently, 30 mL of ice-cold 20 mM $MgCl_2$ was added to each tube, and the pellets were resuspended.
6. The resuspended pellets were centrifuged at 8,000 x g for 20 minutes.
7. The supernatant from this step constituted the periplasmic extract, which was sterile filtered through a 0.22 µm filter cup by vacuum filtration.
8. SDS-PAGE analysis was performed as detailed in Section 2.31, wherein samples of the pellet (collected with a toothpick and dissolved in 20 µL of SDS-buffer), sucrose fraction (10 µL), and periplasmic extract (10 µL) were analyzed to assess the distribution of the LPMOs.

2.34 Protein purification by chromatography

Protein purification is an essential process in molecular biology, enabling the isolation of target proteins for detailed analysis and various applications. This section of protocols involves exploiting the unique characteristics of different chromatographic techniques to selectively separate proteins based on factors such as size, charge, and binding affinity.

2.34.1 Chitin affinity chromatography

Chitin affinity chromatography is a specialized technique used for isolating and purifying chitin-binding proteins such as chitin-active LPMOs and was attempted for purification of *Bl*LPMO10A. This technique relies on the specific binding affinity between chitin beads in the stationary phase and the chitin-binding protein, allowing for selective retention. The introduction of ammonium sulfate optimizes this interaction, enhancing the retention of the target enzyme on the chromatographic matrix. Elution is achieved by using acetic acid at a low pH to disrupt binding interactions and release the protein of interest.

Materials:

- Econo-column®, 1.0 x 10 cm (BioRad)
- Econo-column® flow adapter
- Chitin resin
- BioLogic LP chromatography system
- Running Buffer (1 L): 1 M ammonium sulfate, 20 mM Tris, pH 8.0
- Elution Buffer (0.5 L): 20 mM acetic acid, pH 3.6
- Periplasmic extract of *Bl*LPMO10A: adjusted to 1 M ammonium sulfate, 20 mM Tris, pH 8.0

Protocol:

1. A 1.0 x 10 cm Econo-column® was packed with 10 mL chitin resin.
2. The column underwent an initial manual wash with running buffer by filling it to capacity and allowing the buffer to descend through the resin matrix, minimizing disturbance of the chitin beads. This cycle was repeated 4-5 times.
3. The column was connected to the BioLogic LP chromatography system and subjected to a wash with running buffer at a rate of 2 mL/min for 5 minutes.
4. The periplasmic extract, adjusted to contain 1M ammonium sulfate and 20 mM Tris pH8, was applied to the column at a flow rate of 1.0 mL/min.
5. Using a UV detector measuring absorption at 280 nm, non-binding proteins were eluted until the A280 signal stabilized.
6. After signal stabilization, the elution buffer was introduced to selectively elute *Bl*LPMO10A.
7. The eluate was collected in 50 mL blue cork bottles, and its composition was analyzed using SDS-PAGE (Section 2.31).
8. Elution continued for an additional 5-10 minutes post-peak emergence.
9. A wash with 20% ethanol was performed for 10 minutes.
10. The column was subsequently disconnected from the pump, and 20% ethanol was manually passed through the column multiple times while agitating the beads to ensure comprehensive washing.
11. The washed beads were transferred to a blue-capped tube containing 10% ethanol and stored at 4 °C for future purification of the same protein or discarded.

2.34.2 Anion-exchange chromatography

Ion-exchange chromatography (IEC) separates proteins based on their net surface charges by reversible binding to a specialized stationary phase with opposite charges. The choice between anion and cation exchangers depends on the protein's net charge, determined by its isoelectric point (pI). Anion exchangers are used when the experimental pH exceeds the protein's pI, inducing a net negative charge and interaction with positively charged resin, whereas cation exchangers are used when the pH is below the pI, resulting in a net positive

charge and interaction with negatively charged resin. During chromatography, proteins transiently bind to the resin through ionic interactions and are eluted by increasing the salt concentration; proteins bound by weak interactions elute at lower concentrations, while stronger bindings require higher salt concentrations for elution. Given the isoelectric points of *Bl*LPMO10A (5.89) and *Bs*LPMO10A (6.52), which indicate a net negative charge at the experimental pH of 8.0, an anion exchanger with a positively charged matrix was chosen for their purification using anion-exchange chromatography (AEC).

Materials:

- 5 mL HiTrap® QFF column
- ÄKTA Pure™ chromatography system
- Loading Buffer A: 50 mM Tris-HCl, pH 8.0
- Periplasmic extract (adjusted to 30 mM Tris-HCl, pH 8.0)
- Elution Buffer B: 50 mM Tris-HCl with 1 M NaCl, pH 8.0

Protocol:

1. The HiTrap® QFF column (5 mL) for ion-exchange chromatography was connected to the ÄKTA Pure™ chromatography system following the manufacturer's instructions.
2. The column was prepared by washing with 5 column volumes od MQ water at a flow rate of 2 mL/min.
3. For equilibration with buffer A, the column was initially treated with 100% buffer B until the conductivity stabilized, then switched to 0% buffer B until a low, stable conductivity was achieved. This process was maintained at a flow rate of 2 mL/min and repeated for two additional cycles.
4. Periplasmic extracts adjusted to 30 mM Tris-HCl (pH 8.0) were loaded onto the column at a flow rate of 1 mL/min while monitoring absorbance at 280 nm (A280).
5. Proteins were eluted through a linear NaCl gradient (0 M to 0.5 M) using buffer B at a flow rate of 2.5 mL/min over 100 minutes (equivalent to 50 column volumes).
6. Fractions containing the LPMO of interest were analyzed using SDS-PAGE (Section 2.31).
7. Fractions confirmed to contain only the target LPMO were pooled.
8. A buffer exchange was conducted on the pooled fractions (Section 2.35)

2.35 Concentration and buffer exchange of purified proteins

This protocol aims to increase the concentration of purified proteins while simultaneously adjusting them to an appropriate buffer. The selection of an appropriate buffer considers both the protein's isoelectric point to avoid precipitation and the specific requirements of downstream experimental conditions. The selection of the appropriate buffer considered the

protein's pI, maintaining a pH at least one unit above the pI to prevent precipitation, considering potential variations between actual and theoretical isoelectric points. Consequently, both *Bl*LPMO10A and *Bs*LPMO10A were buffer exchanged to 20 mM Tris-HCl, pH 8.0.

Materials:

- Purified *Bl*LPMO10A and *Bs*LPMO10A
- Tris-HCl, pH 8.0 (20 mM)
- Amicon® Ultra-15 Centrifugal Filter (3.0 kDa cut-off)

Protocol:

1. Purified enzymes were concentrated in a centrifugal filter with a kDa cut-off limit of 3.0 kDa through centrifugation at 4 000 x g at 10°C for 20-30 minutes, reaching a final volume of approximately 1 mL.
2. The resulting protein solution underwent dilution by adding 15 mL of 20 mM Tris-HCl, pH 8.0.
3. The diluted protein solution was centrifuged at 10 °C and 4 500 rpm until the volume reached approximately 500 µL.
4. Buffer washing was repeated three times with gentle inversion between each round to prevent precipitation by aggregation.
5. The resulting protein solution was transferred to an Eppendorf tube and stored at 4 °C for future use.

2.36 Copper saturation of LPMOs

Copper saturation of LPMOs is critical for activating their catalytic functions, as copper acts as a cofactor in the enzyme's active site and is essential for their oxidative activity. The saturation process involves incubating the LPMO with a three-fold molar excess of $CuSO_4$ to ensure copper binding to the active sites. Following this, any unbound copper is removed by a thorough washing procedure.

Materials:

- Purified, buffer exchanged *Bl*LPMO10A and *Bs*LPMO10A
- Tris-HCl, pH 8.0 (20 mM)
- CuSO4 stock solution (50 mM)
- Amicon® Ultra-15 Centrifugal Filter (3.0 kDa cut-off)

Protocol:

1. LPMO samples were copper saturated by incubating with a three-fold molar excess of $CuSO_4$ for 15 minutes at room temperature to ensure adequate copper binding.

2. After incubation, unbound copper was removed by adding 15 mL of 20 mM Tris-HCl (pH 8.0) and centrifuging at 4500 rpm at 10 °C until the volume was reduced to approximately 1.5 mL. The process was repeated until the amount of $CuSO_4$ was theoretically reduced to a final concentration in the range of 10^{-12}-10^{-9} M, assuming no binding to the LPMO and a tenfold dilution per wash.
3. Protein concentrations before and after copper saturation were determined using absorbance at 280 nm (A_{280}) and the Bradford assay (Section 2.37.2).
4. The copper-saturated protein solutions were then transferred to Eppendorf tubes and stored at 4 °C for future use.

2.37 Determination of protein concentration

The concentration of LPMO samples was measured using the A_{280} method, which assesses absorbance at 280 nm, and the Bradford assay, a colorimetric technique.

2.37.1 A_{280}

A_{280}, or absorbance at 280 nm, is a commonly used method that relies on the intrinsic absorbance of proteins, primarily driven by the presence of aromatic amino acids, primarily tryptophan and tyrosine. These residues exhibit characteristic absorbance patterns due to the conjugated π-electron systems within their aromatic rings. The fundamental principle underlying the A_{280} method is the Beer-Lambert law (Equation 2), which establishes that the absorbance of a sample is directly proportional to its concentration, the length of the light path through the sample, and the molar extinction coefficient.

$$(2) \quad A = \varepsilon \cdot c \cdot l$$

Where:
- A is the absorbance,
- ε is the molar extinction coefficient,
- c is the concentration of the protein,
- l is the path length of the light through the sample.

The molar extinction coefficient (ε) is a constant that represents the absorbance of a substance per unit concentration and path length. Since proteins vary in their content of aromatic amino acids, the molar extinction coefficient is an intrinsic property of each protein and is typically determined experimentally. However, in instances where experimental values are unavailable, an estimated theoretical extinction coefficient can be obtained based on the amino acid sequence from databases such as ExPASy ProtParam.

Materials:

- BioPhotometer® D30
- Uvette® disposable cuvettes, 1 cm
- Tris-HCl, pH 8.0 (20 mM)

Protocol:

1. The spectrophotometer was calibrated using 20 mM Tris-HCl (pH 8.0) as a blank.
2. Absorbance at 280 nm was measured for two independent dilutions, 50x and 100x, of each LPMO sample.
3. The concentration of each LPMO was calculated using the Beer-Lambert law based on the absorbance readings and the molar extinction coefficient estimated by ExPASy ProtParam.

2.37.2 Bradford assay

The Bradford utilizes Coomassie Brilliant Blue dye, which binds to proteins and triggers a color shift from brown (Abs_{max} = 465) to blue (Abs_{max} = 595) that can be quantified by spectrophotometry. The dye binds to protein carboxyl groups through van der Waals forces and to amino groups via electrostatic interactions, disrupting the protein structure and exposing hydrophobic pockets that bind non-covalently to the dye's non-polar regions. Unlike the A_{280} method, the Bradford assay is suitable for proteins low in aromatic amino acids, and offers specificity by reacting mainly with proteins, avoiding interference from other substances absorbing at 280 nm. Choosing between Bradford and A_{280} depends on the specific sensitivity and precision needs of the analysis.

Materials:

- Bradford reagent (Bio-Rad Protein Assay Dye Reagent Concentrate)
- BSA stock solution (20 mg/mL)
- 96-well plate
- Multichannel pipette

Protocol:

The Bradford protein assay was conducted per the manufacturer's instructions. Briefly:

1. BSA standards were prepared in the range of 2.5-50 µg/mL to a total volume of 160 in the wells of a 96-well plate, with dH_2O serving as a blank.
2. Three independent dilutions of each unknown protein were prepared, each to a total volume of 160 µL in wells of a 96-well plate.

3. 40 µL of Bradford reagent was added to each well with a multichannel pipette, ensuring thorough mixing by pipetting up and down.
4. The plate was incubated for a minimum of 5 minutes for color development to occur.
5. Absorbance at 595 nm was measured using a plate reader.
6. Protein concentrations were calculated from the BSA standard curve after adjusting for the blank by using SkanIt RE 7.0.2 software.

2.38 Standard LPMO reaction setup for activity assays

The activity of *Bl*LPMO10A and *Bs*LPMO10A was examined through activity assays using chitin and cellulose as substrates. In these assays, the breakdown of polysaccharides into smaller units, called oligosaccharides, was observed to evaluate lytic activity. The presence of these oligosaccharides served as indicators of enzymatic activity and was analyzed using mass spectroscopy. The substrates employed included β-chitin and phosphoric acid swollen cellulose (PASC), with ascorbic acid added to maintain the enzymes in their catalytically active Cu(I) state.

Materials:

- LPMO stock solution (50 µl)
- Ascorbic acid aliquot, or freshly prepared (100 mM)
- Tris-HCl, pH 8.0 (1 M)
- Substrates:
    - PASC (11.5 g/L)
    - β-chitin (20 g/L)

Protocol:

1. Reaction mixtures were prepared in 2 mL Eppendorf tubes according to the specifications listed in Table 2.24, with components added sequentially in the order indicated. Control reactions, including buffer-only, substrate-only, and reactions without ascorbic acid, were included.
2. The reactions were incubated overnight in a thermomixer set to 37°C with agitation at 800 rpm.
3. The reactions were either analyzed immediately for product formation or stored at -20°C for future analysis.

Table 2.24. LPMO activity assay reaction components.

Component	Volume (µL)	Final concentration
Buffer (Tris-HCl pH 8, 1 M)	10	50 mM

LPMO (50 µM)	6	1 µM
β-chitin (20 g/L); PASC (11.5 g/L)	150; 261	10 g/L
dH_2O	To 300	
Ascorbic Acid (100 mM)	3	1 mM

2.39 Matrix-Assisted Laser Desorption/Ionization Time-of-Flight

Analyzing the activity of LPMOs presents challenges due to the complexity of reaction products, reactant autooxidation, and the lack of standardized analytical methods, and their low catalytic turnover rate necessitate sensitive product detection methods (Eijsink et al., 2019). Mass spectrometry (MS) and liquid chromatography (LC) have emerged as crucial tools for assessing LPMO activity, with Matrix-Assisted Laser Desorption/Ionization Time-of-Flight (MALDI-ToF MS) standing out as a robust method for quickly assessing LPMO activity and substrate specificity. In MALDI-ToF MS, samples undergo pulsed laser ionization followed by ion acceleration, with ions separated based on their time-of-flight, reflecting the time each ion takes to travel a fixed distance in a flight tube to reach the detector. This separation is determined by the ions' mass-to-charge ratio (m/z), generating mass spectra for qualitative analysis, and is conducted under vacuum conditions to minimize interference from atmospheric ions. While MALDI-ToF MS provides qualitative insights into enzyme activity, it primarily functions as a qualitative method (Eijsink et al., 2019).

To assess the activity of *Bl*LPMO10A and *Bs*LPMO10A on β-chitin and PASC, the soluble fraction of standard LPMO reactions (Section 2.38) was mixed with an absorbing matrix consisting of 2,5-dihydroxybenzoic acid (DHB), and spotted onto a MALDI plate for selective laser irradiation. This process yielded mass spectra that were compared with a reference standard comprising A3-A6 oligosaccharides ($GlcNAc_{3-6}$ for chitin and Glc_{3-6} for cellulose) for accurate product identification.

Materials:

- LPMO reaction samples (Section 2.38)
- 2,5-dihydroxybenzoic acid matrix (DHB; 9 mg/mL)
- Chito-oligosaccharides or cello-oligosacchares standard solution (A3-A6; 50 µM) (Table 2.12)
- UltrafleXtreme mass spectrometer equipped with a Nitrogen 337-nm laser
- MTP 384 ground steel target plate TF

Protocol:

1. Reaction samples were centrifuged at 21 300 x g for 3 minutes.
2. Mixing of 1 µL of the resulting supernatant with 2 µL of DHB matrix was achieved by applying the matrix as a droplet onto a designated free spot on the MALDI plate, followed by thorough mixing of the reaction sample into the droplet by pipetting up and down. The same protocol was applied for the oligosaccharide standards. To prevent unnecessary drying before sample addition, the matrix was added to one or a few spots at a time.
3. Subsequent drying of the spotted samples was facilitated by applying a stream of warm air by using a hairdryer on low heat, ensuring the air stream was perpendicular to the plate to avoid droplet migration.
4. The plate was placed in the MS sample loader for MALDI-ToF-MS.
5. Calibration was performed using the A3-A6 oligosaccharide standard prior to sample analysis.
6. Data collection and analysis was performed using the Bruker FlexAnalysis software (Table 2.13).

2.40 Generation of vegetative cells of *B. licheniformis*

Vegetative cells of *B. licheniformis* were prepared as substrates for assays to evaluate the activity and binding efficacy of LPMOs to bacterial cell walls. This preparation involved cultivating the cells, before washing and adjusting to a standardized optical density (OD_{600}) of 2.5, resulting in uniform and ready-to-use aliquots for subsequent assays.

Materials:

- Glycerol stock of *B. licheniformis* DSM13
- LB medium
- 50 mM Tris-HCl, pH 8.0
- 20 mM Tris-HCl, pH 8.0

Protocol:

1. For cultivation, 50 mL of LB medium was inoculated from glycerol stocks and incubated overnight at 37°C, 230 rpm.
2. The culture was transferred to 50 mL Falcon tubes and cells were harvested by centrifugation at 10°C, 5000 rpm for 5 minutes.
3. The harvested cell pellet was washed with 20 mL of 50 mM Tris-HCl, pH 8.0.
4. The optical density (OD_{600}) was measured and adjusted to 2.5 using 20 mM Tris-HCl, pH 8.0.
5. The bacterial cells were aliquoted into Eppendorf tubes and stored at -20°C.

2.41 Assessing LPMO activity on vegetive cells of *B. licheniformis*

To assess the effect of LPMOs on vegetative cell walls, optical density at 600 nm (OD_{600}) assays were conducted. Lysozyme from hen-egg white (HEWL), a well-studied glycoside hydrolase that effectively degrades bacterial cell walls, served as a positive control. Lysozymes are a group of N-acetylmuramoylhydrolases that facilitate this degradation by cleaving the β-1,4-glycosidic linkages between N-acetylglucosamine (NAG) and N-acetylmuramic acid (NAM) within the peptidoglycan layer, resulting in bacterial cell lysis. This enzymatic action leads to a noticeable decrease in OD_{600} as cells lyse. The study aimed to determine if *Bl*LPMO10A and *Bs*LPMO10A could produce a similar reduction in OD_{600}, thereby indicating their potential to disrupt cell walls.

The impact of *Bl*LPMO10A and *Bs*LPMO10A on bacterial cell suspensions was monitored using a plate reader, with the reduction in absorbance at 600 nm (OD_{600}) serving as an indicator of lytic activity. Cells were treated with LPMO and ascorbic acid as a reductant while monitoring OD_{600}. To assess for synergistic effects with lysozyme, a low concentration of lysozyme was added to the pre-treated samples simultaneously, allowing observation of potential synergistic effects of LPMOs with lysozyme.

Materials:

- Washed *B. licheniformis* cell suspension (OD_{600} = 2.5) (section 2.40)
- LPMO stock solution (50 µM)
- Ascorbic acid aliquot, or freshly prepared (100 mM)
- Tris-HCl, pH 8 (1 M)
- 96-well plate
- Lysozyme from hen-egg white (HEWL) stock solution (80 g/L)

Protocol:

1. Reaction components, except for ascorbic acid and lysozyme, were added to the wells of a 96-well plate as outlined in Table 2.25. 2 g/L lysozyme was used as a positive control for cell lysis.
2. The prepared plate was placed in a preheated plate reader at 37°C.
3. An initial OD_{600} measurement was taken before adding ascorbic acid and lysozyme using a multichannel pipette.
4. OD_{600} readings were recorded every 2 minutes over an 8-hour period to monitor the effect of LPMOs on cell integrity.

Table 2.25. Reaction components used in OD_{600} activity assay with bacterial cells.

Reaction Component	Volume (µL)	Final Concentration
LPMO (50 µM)	20	5 µM
Cell suspension (OD_{600} ~ 2.5)	10	
dH_2O	To 200	
Ascorbic acid (100 mM)	2	1 mM

Assessing synergistic effects with lysozyme

To determine the impact of lysozyme on the integrity of cells pre-treated with LPMOs, 5 µL of lysozyme was added to each reaction at the end of the assay, achieving a final concentration of 0.1 or 0.01 g/L. Simultaneous introduction was achieved by using a multichannel pipette. Absorbance (OD_{600}) was subsequently recorded at 20-second intervals for 60 minutes to monitor changes in cell integrity.

2.42 Assessing LPMO effect on endospore germination assays based on TbDPA fluorescence, OD_{600} and microscopic analysis

To investigate the potential impact of LPMOs on the germination of endospores, germination assays were performed using purified endospores from *B. licheniformis* and *B. spizizenii*. At the initial phase of germination, endospores release dipicolinic acid (DPA) and undergo partial core hydration. Terbium (Tb) is able to form a specific complex with DPA, which significantly enhances its inherent luminescence under UV light (270_{ex} – 545_{em}), which is exploited to facilitate sensitive quantification of germination via fluorescence spectroscopy. Furthermore, the optical density at 600 nm (OD_{600}) in spore suspensions typically decreases by about 55% during complete germination (Kochan Travis et al., 2018), reflecting changes in the spore core's refractive index, water uptake, and core swelling. This reduction in OD_{600} serves as an additional germination indicator. The progression of germination was monitored by simultaneously measuring TbDPA fluorescence and OD_{600} using a plate reader, where the TbDPA-based method for assessing germination is adapted from Yi and Setlow's (2010) experiments on *B. subtilis*. Endpoints were further analyzed using phase-contrast microscopy to quantitatively assess the fraction of endospores that transitioned from phase-bright to phase-dark as they hydrated during the assay. LPMOs were added to the endospores prior to the assays to evaluate their influence on germination, with the addition of ascorbic acid ensuring the enzymes were in their catalytically active Cu(I) state. L-alanine, serving as a germinant and a

positive control, was used to validate germination and to test for synergistic effects with LPMOs.

Materials:

- Purified endospore suspension (10^{10} endospores/mL) from *B. licheniformis* (section 2.19)
- TbCl3 stock solution (150 mM)
- Dipicolinic acid (DPA) stock solution (1 mM)
- L-alanine stock solution (200 mM)
- LPMO stock solution (50 µM)
- Ascorbic acid (10 mM)
- Tris-HCl, pH 8 (1 M)
- 96-well plate

Protocol:

1. Endospores were added to a PCR or Eppendorf tube and were heat activated by incubating at 75°C for 15 minutes in a thermocycler or heating block.
2. Reaction components, except for ascorbic acid and L-alanine, were added to the wells of a 96-well plate as outlined in Table 2.26. Endospores with 100 mM L-alanine served as a positive control for germination.
3. The prepared plate was placed in a plate reader preheated to 37°C.
4. An initial measurement of OD_{600} and fluorescence at 270 nm excitation and 545 nm emission was taken before the addition of ascorbic acid.
5. Absorbance (OD_{600}) and fluorescence ($270_{ex} – 545_{em}$) measurements were recorded at 2-minute intervals over an 8-hour period.
6. Samples were analyzed by phase-contrast microscopy.

Assessing synergistic effects with L-alanine

For assessing synergistic effects with L-alanine, 100 µM L-alanine was added last to the reactions using a multichannel pipette to ensure simultaneous introduction. Absorbance (OD_{600}) and fluorescence ($270_{ex} – 545_{em}$) measurements were recorded at 2-minute intervals over a 90-minute duration.

Table 2.26. Reaction components used in germination activity assays.

Reaction Component	Volume (µL)	Final Concentration
LPMO (50 µM)	20	5 µM
Heat-activated endospore solution (10^{10} endospores/mL)	10	$5 \cdot 10^8$ endospores/mL

Ascorbic Acid (1 mM)	20	100 µM
TbCl3 (150 mM)	10	7.5 mM
dH_2O	To 200	

2.43 Decoating of endospores

Decoating of endospores was performed to remove the outer coat layers, thereby exposing the cortex and potentially enhancing any binding of LPMOs in subsequent assays. Decoating involved treating endospores with a solution containing several components, including dithiothreitol (DTT) and sodium dodecyl sulfate (SDS) used to denature proteins in SDS-PAGE analysis (Section 2.31). These components were used to collectively degrade and remove the proteinaceous outer coat of endospores.

Materials:

- Purified endospores
- Decoating solution (Table 2.3)

Protocol:

1. Purified endospores were added to an Eppendorf tube and centrifuged at 10,000 x g for 5 minutes at 4°C.
2. The endospores were then resuspended in 1 mL of decoating solution.
3. The tube was incubated at 70°C for 2 hours.
4. Following the incubation, the endospores were centrifuged at 10,000 x g for 5 minutes at room temperature.
5. The decoated endospores were washed by centrifuging at 10,000 x g for 5 minutes at room temperature. This washing step was repeated at least three times.

2.44 Substrate binding assays

Substrate binding assays provide insights into the substrate specificity and binding affinity of enzymes. In the context of this thesis, substrate binding assays were conducted to assess LPMO binding to β-chitin, cellulose, and decoated *B. licheniformis* endospores (Section 2.43). *Sm*LPLMO10A acted as a positive control for β-chitin binding assays, while *Sc*LPMO10C served as a positive control for cellulose binding assays. Substrate binding was quantified through the Bradford assay, a method for selectively quantifying proteins at 595 nm, and qualitatively verified by SDS-gel analysis. Controls featuring only the substrate functioned as blanks, while controls comprising only LPMO served to account for potential precipitation or binding to the PET filter.

Materials:

- Stock substrate solutions:
  - β-chitin (20 g/L)
  - PASC (11. g/L)
  - Decoated *B. licheniformis* endospore suspension (Section 2.43)
- LPMO stock solution (50 µM)
- Tris-HCl, pH 8 (1 M)
- 96-well plate
- 96-well filter plate
- SDS-buffer

Protocol:

1. Solutions were prepared 2 mL Eppendorf tubes, as detailed in Table 2.27. Wide-bore pipette tips were used to prevent clogging by the substrates. β-chitin was meticulously vortexed before each extraction to ensure consistent substrate concentration. Controls with only substrate and controls with only LPMO were included.
2. Solutions were incubated in a thermomixer at 37 °C, 800 rpm for 2 hours.
3. For protein concentration analysis, 100 µL from each solution was filtered using a 96-well filter plate. Subsequently, 20 µL of the filtered solution was used in the Bradford assay (Section 2.37.2).
4. For SDS-gel analysis, the remaining 200 µL was centrifuged at maximum speed for 3 minutes, and the supernatant was carefully set aside. The pellet was washed by resuspending it in 100 µL buffer, followed by centrifugation. This washing step was repeated three times. Subsequently, 10 µL of the washed pellet resuspended in 100 µL SDS-buffer, 10 µL of the first supernatant and 10 µL of controls containing only enzyme were boiled and loaded onto the SDS-gel (Section 2.31), allowing for comparison between total, bound, and non-bound enzyme.

Table 2.27. Components used in substrate binding assays.

Component	Volume (µL)	Final concentration
Tris-HCl, pH 8 (1 M)	4	20 mM
LPMO (50 µM)	20	5 µM
β-chitin (20 g/L); PASC (11.5 g/L)	100; 174	10 g/L
dH_2O	To 200	

3. Results

3.1. Fluorescence-based promoter screening

The aim of this study was to identify potential novel substrates for lytic polysaccharide monooxygenases (LPMOs). The research initially focused on the expression patterns of the LPMO in *Bacillus licheniformis* (*Bl*LPMO10A) during different growth phases and in response to various environmental factors to gain insights into function and substrate specificity. The *Bl*LPMO10A promoter was transcriptionally fused with the fluorescent reporter gene mCherry in a plasmid and transformed into *B. licheniformis*. This integrated the mCherry reporter gene under the control of the *Bl*LPMO10A promoter, allowing the expression of mCherry under varied conditions to be used as a proxy for LPMO expression in subsequent fluorescence-based screening assays.

3.1.1 Plasmid construction

An 1135 bp promoter-reporter fragment was designed by transcriptionally fusing the 400 bp region upstream of *Bl*LPMO10A to a 708 bp mCherry gene (Figure 3.2), which was codon-optimized for *B. licheniformis*. The DNA fragment was designed to include 15 bp overhangs that matched the ends of the linearized *E. coli*/*B. subtilis* shuttle vector pHT01E7 (Table 2.5, 2.6) to facilitate its integration via seamless In-Fusion cloning (Section 2.22.1).

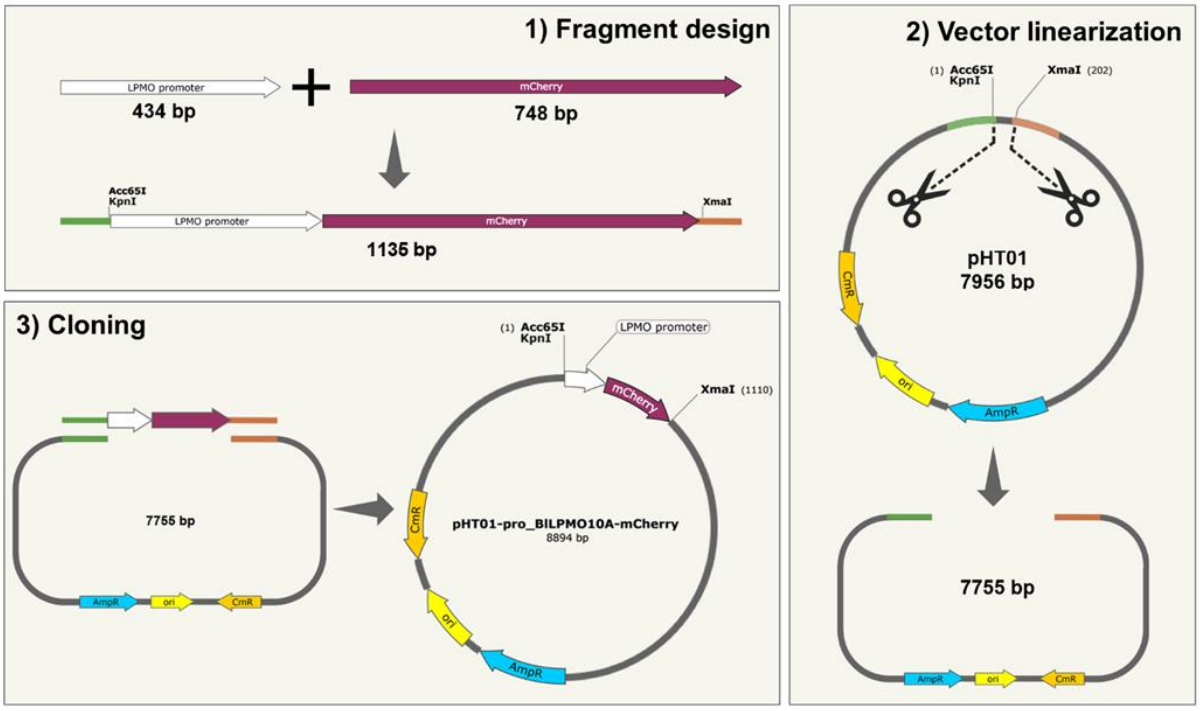

Figure 3.2. Schematic overview of plasmid construction for fluorescence-based promoter screening. **1) Fragment design**: Fusion of a 400 bp segment of the LPMO promoter region and a 708 bp mCherry reporter gene resulted in a 1135 bp Pro-mCherry synthetic fragment. The fragment includes 15 bp overhangs complementary to the ends of the linearized pHT01E7 vector, as indicated in orange and green, and includes Acc65I (KpnI) and XmaI restriction sites. **2) Vector linearization**: Double digestion of pHT01E7 at the corresponding Acc65I (KpnI) and XmaI restriction sites yields the linearized vector. **3) Cloning**: Cloning of the synthetic Pro-mCherry fragment into the linearized vector yields pPro-mCherry.

However, multiple attempts at In-Fusion cloning of the resulting 1135 bp Pro-mCherry fragment using Acc65I/XmaI-digested pHT01E7 did not result in colonies following transformation in *E. coli* (Section 2.23). In response, a revised strategy was attempted, replacing Acc65I with its isoschizomer, KpnI, and complete digestion was verified by agarose gel electrophoresis (Figure 3.3). However, this change led to insufficient overlap for InFusion cloning, necessitating a shift to traditional ligation (Section 2.22.2). The synthetic fragment was treated with KpnI/XmaI, and this revised approach yielded two *E. coli* colonies, confirmed by colony PCR (Figure 3.3).

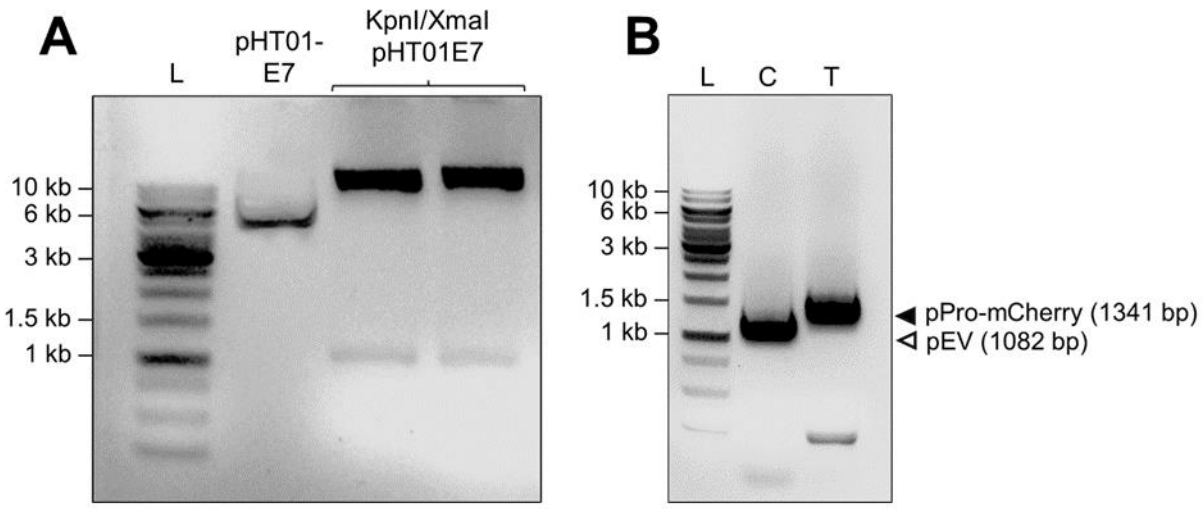

Figure 3.3. Verification of vector linearization and cloning by agarose gel electrophoresis. (A) DNA ladder (L) with corresponding molecular sizes in kilobases (kb); undigested pHT01-E7 vector; digestion of pHT01E7 with KpnI and XmaI. **(B)** Colony PCR verification of cloning. DNA ladder (L) with corresponding molecular sizes in kilobases (kb); control lane (C) showing the PCR result for undigested pHT07; transformant lane (T) displaying the colony PCR results for one of the transformants.

3.1.2 Sequence analysis of recombinant pPro-mCherry plasmids

Sanger sequencing (Section 2.24) of the two recombinant plasmids revealed an unexpected mutation in the mCherry gene, causing a K202E amino acid substitution (Figure 3.4 A). Despite being far downstream in the gene, this amino acid substitution was notable due to the distinct properties of lysine (positively charged) and glutamic acid (negatively charged), which could potentially affect protein function and might inhibit the production of a fluorescent signal. The mutation was present in both plasmids, suggesting it occurred during the initial PCR amplification.

Further efforts to construct the pPro-mCherry with the correct sequence included modifications to the vector-to-insert ratios, extension of incubation times, experimentation with various competent *Escherichia coli* strains, and exploration of additional restriction sites and cloning methods. Despite comprehensive troubleshooting, subsequent cloning attempts were unsuccessful in producing colonies.

3.1.3 Evaluation of K202E mutation effects on mCherry signal

Due to the failure of new cloning attempts, an *in silico* assessment was conducted to determine the potential impact of the K202E mutation on the mCherry signal. ProtParam (Table 2.13) analysis indicated an increase in the instability index (II) of mCherry from 33.58 to 36.17 due to the mutation, but the protein remained categorized as stable with a value below 40. Structural predictions of the K202E mCherry mutant using Alphafold Colab (Table 2.13) identified that the mutation resided on the surface of the β-barrel structure of the protein (Figure 3.4). Structural alignment with the wild-type mCherry protein indicated no significant changes in the overall three-dimensional conformation.

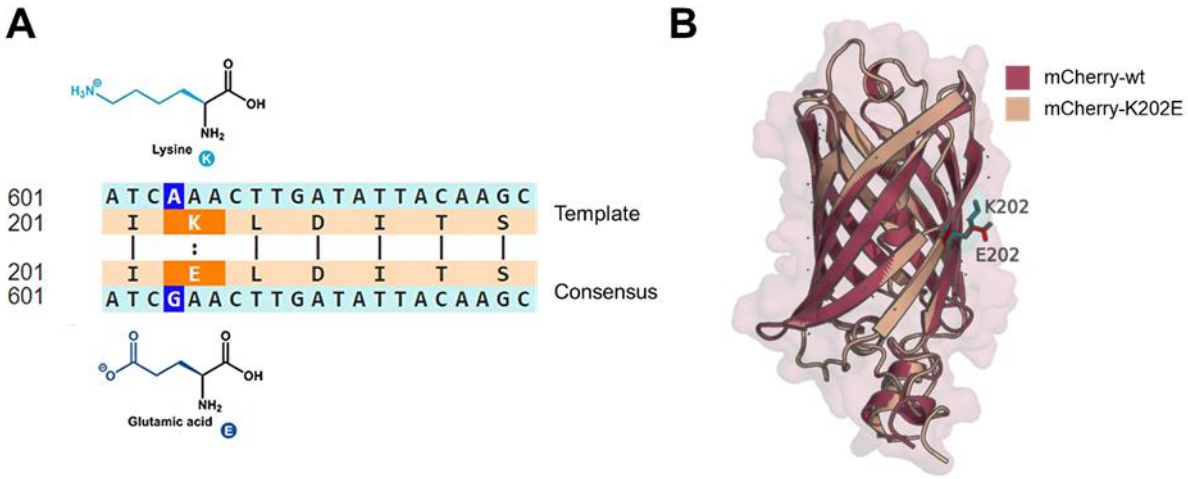

Figure 3.4. Characterization of the mCherry K202E mutation. (A) Alignment of nucleotide and corresponding amino acid sequences from the template and consensus sequences of the mCherry gene in recombinant pPro-mCherry plasmids. A highlighted base substitution (A to G) at nucleotide 601 corresponds to an amino acid substitution at position 202 (K202E). **(B)** Superimposed structures of wild-type mCherry (mCherry-wt) and the K202E mutant variant (mCherry-K202E) using PyMOL. The mutation site is highlighted in the shared β-barrel conformation, with the wild-type lysine (K202) in cyan and the mutant glutamic acid (E202) in red.

The impact of the K202E mutation on the fluorescence signal was evaluated by cloning the mutant mCherry gene into a pSIP vector with constitutive expression in *E. coli* and inducible expression in *Lactiplantibacillus plantarum*. This allowed for a direct comparison with an existing equivalent plasmid, pCherry, containing the wild-type mCherry gene (Table 2.5). The mCherry-K202E sequence was amplified using primers with tails complementary to the vector (Table 2.6). The vector was linearized through double digestion with HindIII and NdeI restriction enzymes (Section 2.21), followed by In-Fusion cloning of the PCR-amplified mCherry-K202E sequence, resulting in pCherry-K202E (Table 2.5). Sub-cloning into *E. coli*

TOP10 resulted in colonies with a promising pink hue, indicative of a functional mCherry protein.

Further analysis of the mCherry-K202E mutant signal was performed when expressed in *L. plantarum*. The plasmid was transformed into competent *L. plantarum* WCFS1 cells (Section 2.26), and successful integration of the plasmid was verified by colony PCR and sequencing. To quantify the fluorescence intensity of the mutant protein compared to the wild-type mCherry, growth curve experiments were performed with continuous monitoring of mCherry fluorescence post-induction by sppIP (Section 2.28.2). Figure 3.5 shows that mCherry-K202E exhibited a fluorescence signal 2-3 times lower than the wild-type mCherry. This experiment was repeated with consistent results.

The impact of the mutation on the excitation or emission spectrum of the mCherry protein was investigated to determine if it could explain the reduced signal intensity. The analysis indicated no significant shift in peak excitation or emission wavelengths (results not shown), showing that the decrease in fluorescence intensity for the mCherry-K202E mutant is likely due to alterations in protein stability or folding efficiency rather than changes in the spectral properties of the fluorophore.

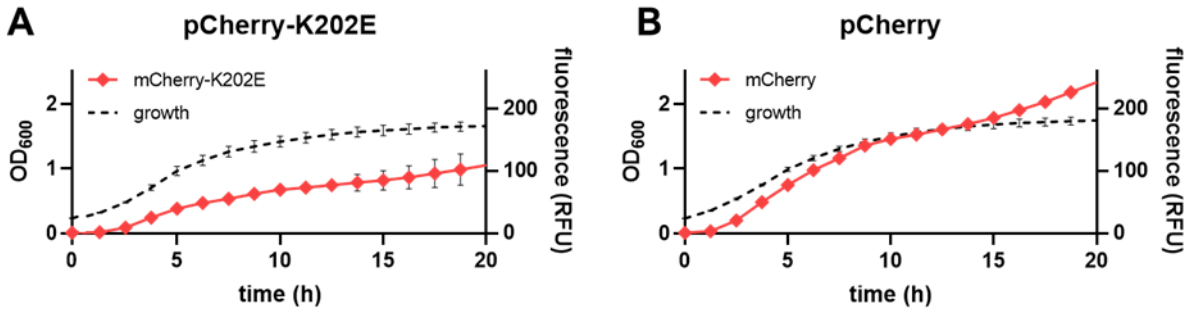

Figure 3.5. Comparing fluorescence intensities of wild-type and mutant mCherry. Growth (OD_{600}) and fluorescence signal (RFU) from mCherry expression induced by sppIP in *L. plantarum* transformed with **(A)** pCherry and **(B)** pCherry-K202E were continuously measured every 5 min for 20 hours. Every 15th datapoint is plotted as the mean of three technical replicates ± standard deviation.

3.1.5 MIC determination of chloramphenicol in *B. licheniformis*

Determining the Minimum Inhibitory Concentration (MIC) of chloramphenicol, the antibiotic selection for the pHT01 backbone in *Bacillus*, was critical for transforming the empty vector and recombinant pPro-mCherry-K202E plasmid into *B. licheniformis* MW3. The MIC is defined as the lowest concentration that inhibits the visible growth of the wild-type strain. After inoculation of *B. licheniformis* with chloramphenicol concentrations ranging from 0 to 45

µg/mL, an MIC of 10 µg/mL was determined through visual inspection. Based on these findings, a chloramphenicol concentration of 15 µg/mL was chosen for transformant screening and applied in all subsequent experiments involving *B. licheniformis* transformed with pHT01 derivatives.

3.1.6 Optimization of *B. licheniformis* transformation protocol

Historically, genetic studies and biotechnological applications of *B. licheniformis* have been hindered due to their restriction-modification system that degrades foreign DNA. The development of *B. licheniformis* MW3, a more transformable mutant derived from the fully sequenced type strain *B. licheniformis* DSM 13, has significantly mitigated these challenges (Veith et al., 2004; B. Waschkau et al., 2008). Due to its superior transformability, *B. licheniformis* MW3 was chosen as the target strain for promoter screening in this study.

The procedure for preparing electrocompetent cells and transforming *B. licheniformis* was new to this laboratory. Therefore, this study sought to refine and optimize existing transformation protocols for *B. licheniformis* (Løvdal et al., 2012). The optimization process primarily involved adjusting electroporation parameters including voltage (kV) and resistance (Ω).

To determine the optimal conditions for electroporation, various combinations of voltage settings (from 1.4 to 2.0 kV) and resistance values (400 Ω and 200 Ω) were tested by comparing the number of colonies observed (Figure 3.6). There was significant variation in the number of transformants achieved with different electroporation settings, with the highest number of transformants observed at 1.4 kV with a resistance of 400 Ω, and by using this configuration, both the recombinant pPro-mCherry-K202E plasmid and the empty vector were successfully introduced into electrocompetent *B. licheniformis* MW3 cells, as verified by colony PCR (data not shown).

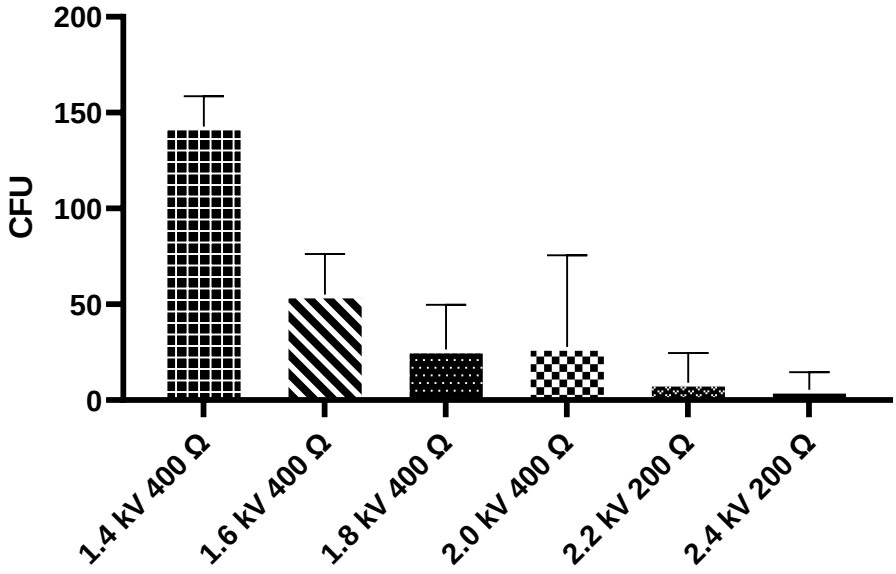

Figure 3.6. Optimization of electroporation conditions for *B. licheniformis* transformation. The number of colony-forming units (CFUs) obtained from electroporation of *B. licheniformis* under various voltage (kV) and resistance (Ω) settings is displayed. Each bar represents the mean of three technical replicates ± standard deviation.

3.1.7 Assessing promoter activation in response to various nutrient conditions

To investigate the impact of various growth media and additional carbon sources on LPMO expression, promoter screening assays by growth curve analysis with simultaneous fluorescence monitoring were conducted in *B. licheniformis* transformed with pPro-mCherry (Section 2.27). A plate reader was used to simultaneously measure growth and mCherry fluorescence of *B. licheniformis* over 20 hours using different nutrient media, including BHI and LB medium (Section 2.28.1). Additionally, LB medium was supplemented with 2% (w/v) of specific carbohydrates—glycogen, glucose, fructose, and mannose—to assess their potential influence on promoter activity.

B. licheniformis harboring the pPro-mCherry plasmid was monitored and compared to a control strain carrying the empty vector (pEV). Under conditions with glucose-supplemented LB (Figure 3.7), fluorescence intensities recorded showed no significant differences between cells harboring pPro-mCherry and pEV. Similar results, indicating no differences in fluorescence intensity, were observed in assays for all other media compositions tested (data not shown). These findings suggest a lack of promoter activity under these conditions, indicating that the promoter does not exhibit constitutive activity nor respond to the nutrients in the growth media. The analyses were reproducible in independent biological replicates.

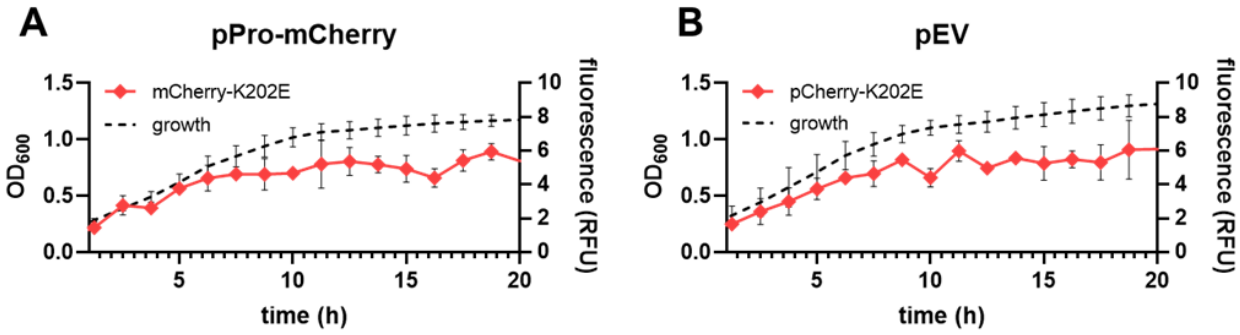

Figure 3.7. LPMO promoter activity in *B. licheniformis* grown in glucose-supplemented LB. Growth (OD_{600}) and mCherry fluorescence signal (RFU) in *B. licheniformis* transformed with (A) pPro-mCherry and (B) pEV were continuously measured every 15 min for 20 hours. Every fifth datapoint is plotted as the mean of three technical replicates ± standard deviation.

3.1.8 Assessing promoter activation during sporulation and germination

The central hypothesis of this study was that *Bl*LPMO10A could play a role in the germination processes of *B. licheniformis*, contributing to the identification of novel substrates for LPMOs. Given that germination-specific lytic enzymes (GSLEs) are expressed during sporulation and stay inactive until germination (Setlow et al., 2001), it was hypothesized that if *Bl*LPMO10A is involved in germination, it would likely be expressed during sporulation or possibly during germination itself if it has a role in later stages. To investigate this, promoter screening assays were conducted using a plate reader to assess potential changes in LPMO expression during both sporulation and germination.

Growth and mCherry fluorescence were monitored over 36 hours in sporulation medium to observe the sporulation process (Figure 3.8 A and B). The observed decrease in optical density at 600 nm (OD_{600}) after approximately 10 hours signifies the transition from vegetative growth to endospore formation. This decrease occurs as the vegetative mother cells are lysed, giving way to the smaller endospores and consequently a lower optical density. Between cells harboring pEV and pPro-mCherry, no difference in fluorescence signal was detected during sporulation, with consistent results across independent replicates (data not shown).

In germination assays, endospores underwent heat activation and were treated with L-alanine to initiate germination (Section 2.42). Germination was measured over 1.5 hours by monitoring the increase in fluorescence signal from the addition of terbium chloride (TbCl3) (Figure 3.8 C and D). This fluorescence occurs as terbium (Tb) binds to dipicolinic acid (DPA), which is released from the endospores during germination. A distinct increase in TbDPA fluorescence

was observed, indicating germination, while mCherry fluorescence did not increase. This suggested that mCherry expression was not induced during germination, with consistent results across independent biological replicates.

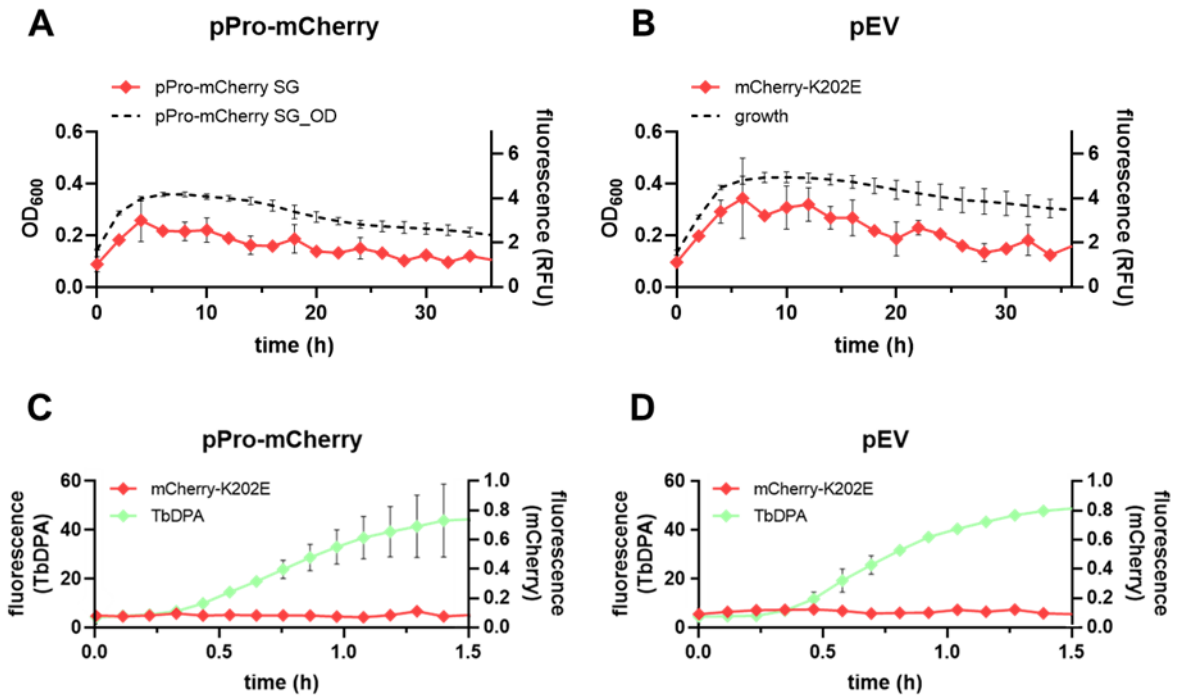

Figure 3.8. LPMO promoter activity during *B. licheniformis* sporulation and germination. Growth (OD_{600}) and mCherry fluorescence signal (RFU) in vegetative cells of *B. licheniformis* transformed with **(A)** pPro-mCherry and **(B)** pEV were continuously measured every 15 min for 36 hours in sporulation medium. Every eight datapoint is plotted as the mean of three technical replicates ± standard deviation. TbDPA fluorescence (RFU) and mCherry fluorescence signal (RFU) in *B. licheniformis* endospores transformed with **(C)** pPro-mCherry and **(D)** pEV were continuously measured every 2 min for 1.5 hours after addition of 100 mM L-alanine. Every third datapoint is plotted as the mean of three technical replicates ± standard deviation.

3.1.9 Promoter screening in sporulating cells by fluorescence microscopy

To investigate whether the absence of detectable mCherry fluorescence in growth assays could be attributed to its expression in only a limited subset of cells, fluorescence microscopy was performed for *B. licheniformis* to assess mCherry expression in individual cells. Fluorescence microscopy (Section 2.30) was carried out at various stages of sporulation, with Figure 3.9 presenting a representative sample from day 2 of endospore generation (described in Section 2.29). During these stages, a faint but discernible mCherry signal was detected in endospores, which was absent in vegetative cells and more pronounced in mature endospores compared to prespores. However, this faint signal was observed in strains harboring both pPro-mCherry-K202E and pEV, suggesting that the fluorescence was not due to promoter-driven mCherry expression but rather an inherent autofluorescence of the endospores. This is illustrated in

Figure 3.9 which shows vegetative cells, prespores within mother cells, and mature endospores, with comparable fluorescence observed in cells harboring pEV and pPro-mCherry.

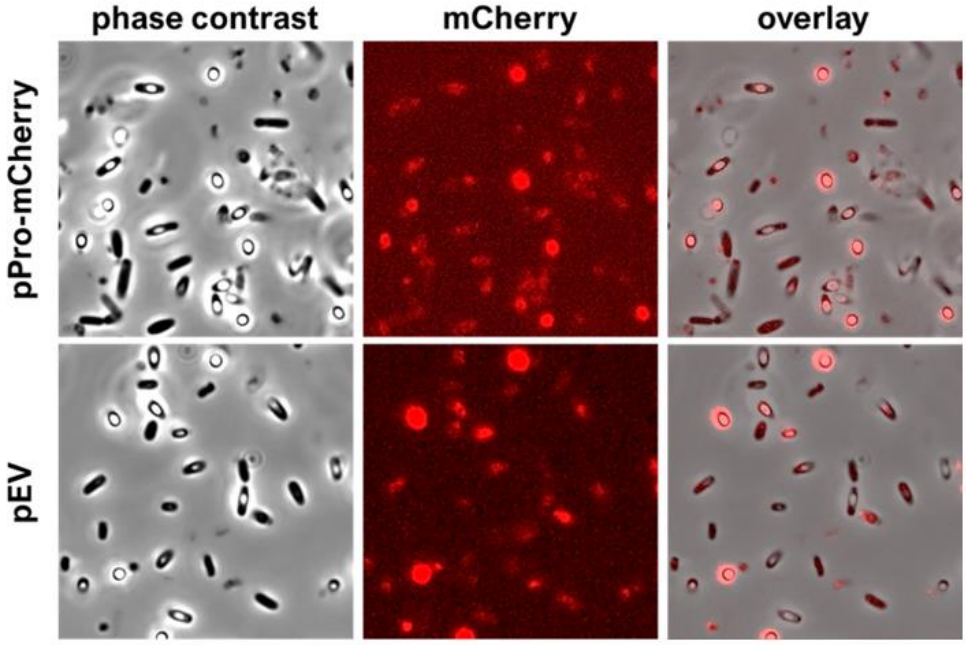

Figure 3.9. Fluorescence microscopy for assessing LPMO promoter activity in *B. licheniformis* endospores. Phase-contrast (left), mCherry fluorescence (center), and merged images (right) of *B. licheniformis* transformed with pPro-mCherry (upper panel) and pEV (lower panel). Images were analyzed in Fiji (Table 2.13)

3.2 Characterization of *Bs*LPMO10A and exploration of novel LPMO functions in *Bacillus* spp.

As initial promoter screening assays gave no indications of LPMO promoter activity in *B. licheniformis*, the focus of the study transitioned towards the structural and functional characterization of a previously unexplored LPMO from the closely related *Bacillus spizizenii* TU-B-10 (*Bs*LPMO10A). The objective was to assess activity on various substrates, and this was conducted in parallel with the already characterized chitin-active *Bl*LPMO10A (Forsberg, Røhr, et al., 2014; Manjeet et al., 2013) for a comparative analysis.

In silico structure prediction and structural alignments was initially performed to compare *Bs*LPMO10A with previously characterized LPMOs. This was followed by heterologous expression, extraction, purification, and copper saturation to yield mature holo-enzymes of both *Bs*LPMO10A and *Bl*LPMO10A. Chitinolytic activity was first assessed to verify the activity of the produced enzymes, and their binding affinity to chitin was evaluated. Potential activity of

*Bs*LPMO10A on cellulose was also explored, followed by an assessment of the potential roles of these LPMOs in cell wall modification and germination of endospores.

3.2.1 Assessing genomic potential for chitin degradation

LPMOs are typically recognized for their synergistic activity with chitinases (Harris et al., 2010; Vaaje-Kolstad, Horn, et al., 2005), which are predominantly categorized under the glycoside hydrolase family 18 (GH18). However, the roles of GH18 enzymes extend beyond chitin degradation, exhibiting various activities across different species, as documented in the CAZy database. Given the established synergistic activity of characterized LPMOs with GH18 chitinases, the parent strains of *Bs*LPMO10A and *Bl*LPMO10A, namely *B. spizizenii* TU-B-10 and *B. licheniformis* DSM13, were investigated to identify any putative GH18 genes. By comparing these genes with homologous enzymes with annotated functions in other species, this preliminary analysis aimed to gain insights into the potential activities of GH18s, which might involve synergistic interactions with their corresponding LPMO.

According to the CAZy database, *B. spizizenii* TU-B-10 harbors genes encoding three putative GH18 family chitinases, while *B. licheniformis* has genes encoding four putative GH18 family chitinases. To gain insights into their potential functions, these genes were compared by multiple sequence alignment in a multigenome browser (BioCyc; Table 2.13) with the well-annotated *Bacillus subtilis* 168, in order to infer the activities of potential homologues present in this strain (**Feil! Fant ikke referansekilden.**).

The analysis revealed that *B. licheniformis* has two GH18 genes annotated as chitinases (**Feil! Fant ikke referansekilden.** A), organized in an operon, with no homologues observed in either *B. spizizenii* or the analyzed *B. subtilis* strains. Both *B. spizizenii* and *B. licheniformis* appear to share two common GH18 genes (**Feil! Fant ikke referansekilden.** B and C), which seem to be homologous to GH18s in *B. subtilis* annotated as a spore peptidoglycan N-acetylglucosaminidase (yaaH) and a spore cortex peptidoglycan hydrolase (SclL).

Interestingly, *B. spizizenii* possesses a GH18 gene not found in *B. licheniformis* (**Feil! Fant ikke referansekilden.** D), homologous with a GH18 in *B. subtilis* annotated as a putative sporulation-specific glycosylase (ykvQ). The last GH18 gene encoded by *B. spizizenii* (**Feil! Fant ikke referansekilden.**), as specified in the CAZy database, appears to be homologous with a gene in *B. subtilis* annotated as a putative epimerase involved in the modification of

peptidoglycan (yvbX). However, in *B. spizizenii*, this gene is divided into two pseudogenes by an IS3 family transposase.

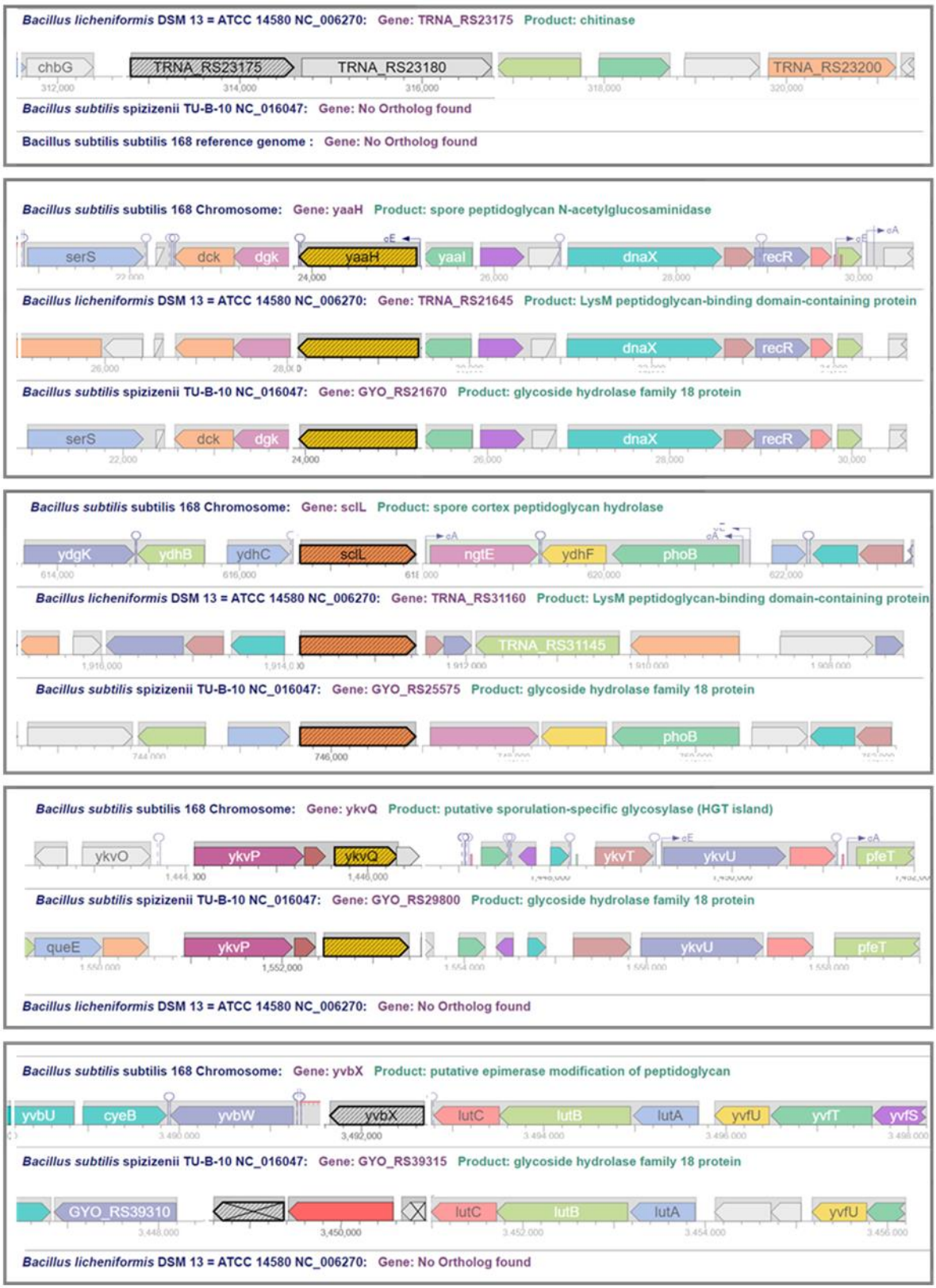

Figure 3. 10. **Comparative genomic analysis of GH18 family chitinases in *Bacillus* spp**. Multiple sequence alignment of GH18 genes identified in *B. spizizenii* TU-B-10 and *B. licheniformis* DSM13 with *B. subtilis* 168 in a multigenome browser, displaying **(A)** the operon organization of two GH18 chitinase genes in *B. licheniformis*, absent in *B. spizizenii* and *B. subtilis*; **(B)**, homologues of a spore peptidoglycan N-acetylglucosaminidase (*yaaH*); **(C)** homologues of spore cortex peptidoglycan hydrolase (*SclL*); **(D)** *B. spizizenii* homologue of a sporulation-specific glycosylase (*yvbX*), not present in *B. licheniformis*, and split by a IS3 family transposase, yielding two pseudogenes. Analysis performed using BioCyc (Table 2.13).

3.2.1 *In silico* structural analysis of *Bs*LPMO10A

The structure of an LPMO's catalytic domain can yield key insights into substrate specificities. *Bs*LPMO10A, which comprises a single catalytic AA10 domain, similar to the chitin-active *Bl*LPMO10A and the extensively studied *Sm*LPMO10A from *Serratia marcescens*, was subjected to in silico structural prediction. Although the structure of *Bl*LPMO10A has previously been determined by NMR (Courtade et al., 2015), its structure was also predicted in silico to generate a structure more analogous to those determined by crystallography.

Mature protein sequences of *Bs*LPMO10A (179 aa; WP_003220432.1) and *Bl*LPMO10A (172 aa; AAU39477.1, retrieved from GenBank, were structurally predicted using AlphaFold Colab (Table 13). Structural comparison of the catalytic domain of previously characterized AA10 LPMOs was conducted using the DALI server (Table 13), with two AA9 LPMOs serving as an outgroup. The resulting structural similarity dendrogram was visualized using Interactive Tree Of Life (iTOL).

As shown in Figure 3.11 A, the dendrogram and excerpt of the structural similarity matrix (DALI Z-scores) reveal that *Bs*LPMO10A is, as expected, most structurally similar to other LPMOs from the *B. subtilis* group. In particular, it displays the greatest structural similarity to *Ba*LPMO10A (Z-score of 35.4), followed by *Bl*LPMO10A (Z-score of 30.8). Interestingly, the structural similarity of *Bs*LPMO10A to *Bl*LPMO10A did not significantly surpass the similarity observed with other more distantly related LPMOs.

Comparative analysis of *Bs*LPMO10A with *Bl*LPMO10A and *Sm*LPMO10A (Figure 3.11 B), which was used as a reference for high-affinity binding to chitin later in the study (Section 0), revealed a slightly less negatively charged and what appeared to be a less flat substrate-binding surface in *Bs*LPMO10A. Structural diversity in AA10 LPMOs is largely confined to the L2 loop region, which forms a large protuberance and contributes to at least half of the putative substrate-binding surface (Book et al., 2014; Borisova et al., 2015; Forsberg, Mackenzie, et al., 2014; Vaaje-Kolstad et al., 2017). Notably, the L2 loop observed in *Bs*LPMO10A is significantly larger than those in *Sm*LPMO10A and *Bl*LPMO10A.

Key residues involved in chitin binding were observed to be present in *Bs*LPMO10A (Figure 3.11 C), but with variations in the specific residues compared to *Bl*LPMO10A and *Sm*LPMO10A. Notably, the conserved aromatic residue involved in enzyme-carbohydrate interactions (Aachmann et al., 2012), represented by Tyr54 in *Sm*LPMO10A and Tyr30 in *Bl*LPMO10A, was constituted by Trp23 in *Bs*LPMO10A.

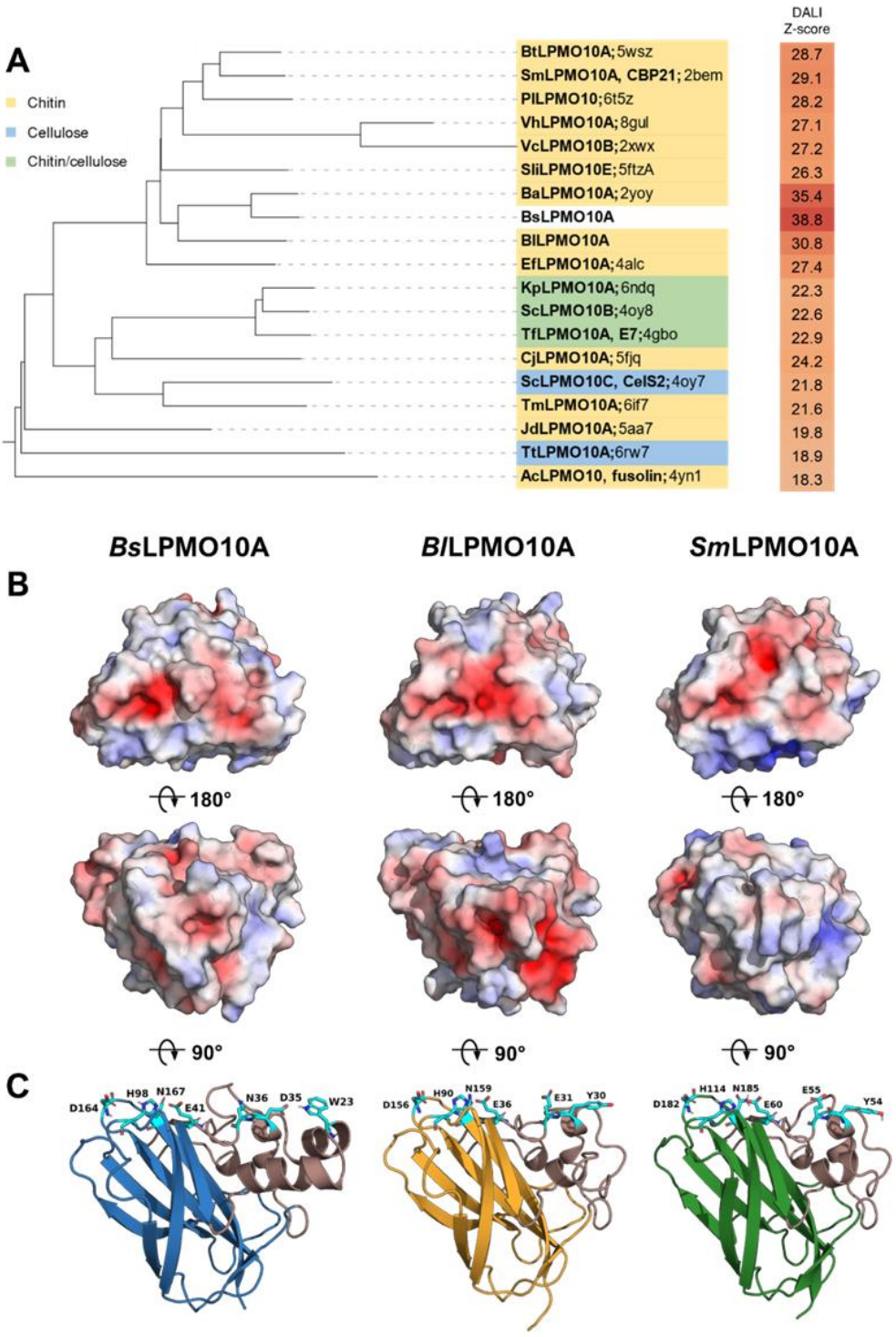

Figure 3.11. Comparative structural analysis of *Bs*LPMO10A with *Bl*LPMO10A and *Sm*LPMO10A. (A) Dendrogram based on structural similarity (DALI Z-scores) illustrating the relationships between *Bs*LPMO10A and characterized AA10 LPMOs, with Z-scores indicating the degree of structural similarity. **(B)** Electrostatic surface potential maps of *Bs*LPMO10A, *Bl*LPMO10A, and *Sm*LPMO10A, highlighting differences in substrate-binding surface charge and topography. Top panels show surfaces as they would appear to the substrate, while lower panels show a 180° rotation. **(C)** Structural models displaying the secondary structures of *Bs*LPMO10A, *Bl*LPMO10A, and *Sm*LPMO10A, with L2 loop regions colored in beige. Key residues involved in chitin binding are indicated in cyan and labeled, with the conserved aromatic residue involved in enzyme-carbohydrate interactions shown as Trp23 in *Bs*LPMO10A, Tyr30 in *Bl*LPMO10A, and Tyr54 in *Sm*LPMO10A. Note that residue numbering includes the signal peptide in *Sm*LPMO10A but only the mature sequences in *Bs*LPMO10A and *Bl*LPMO10A. Figure created using iTOL and PyMOL 2.

3.2.3 Expression and extraction of *Bl*LPMO10A and *Bs*LPMO10A

Heterologous expression, extraction, purification and copper saturation of *Bl*LPMO10A and *Bs*LPMO10A were performed to produce mature holo-enzymes in order to investigate their substrate specificity, affinity, and catalytic functions.

For enzyme production, p*Bs*LPMO10A and p*Bl*LPMO10A (Table 2.5) were transformed into *E. coli* BL21, and the LPMOs were expressed with an N-terminal signal peptide directing them to the periplasm. *Bl*LPMO10A expression, controlled by a constitutive promoter, was conducted at 37°C overnight, while *Bs*LPMO10A expression was induced with 0.4 mM IPTG upon reaching the exponential growth phase (OD_{600} 0.75) (Section 2.32) with expression tested at both 30°C and 37°C for 6 hours.

Cell fractionation was performed using the cold osmotic shock method (Section 2.33), involving the suspension of harvested cells in a high-sugar buffer, followed by an ice-cold water wash. This process partially disrupted the outer membrane while maintaining the integrity of the cytoplasmic membrane, leading to the release of periplasmic proteins into the supernatant without contamination from cytoplasmic proteins.

The periplasmic extracts, sugar fractions, and cell pellets obtained were analyzed using SDS-PAGE to assess the presence and distribution of *Bl*LPMO10A and *Bs*LPMO10A (Figure 3.12). Distinct protein bands corresponding to the estimated weights of approximately 20 kDa for *Bs*LPMO10A (Figure 3.12 A) and 19 kDa for *Bl*LPMO10A (Figure 3.12 B) were observed. Bands for *Bs*LPMO10A appeared in both the cell pellet and sugar fraction but were faint compared to the intense bands in the periplasmic extracts, indicating high levels of expression. *Bl*LPMO10A was almost undetectable in the sugar fraction and absent in the cell pellet, suggesting effective periplasmic extraction without cell lysis. *Bs*LPMO10A expression at 37°C yielded notably higher levels than at 30°C, as evidenced by the more pronounced band in the periplasmic extract.

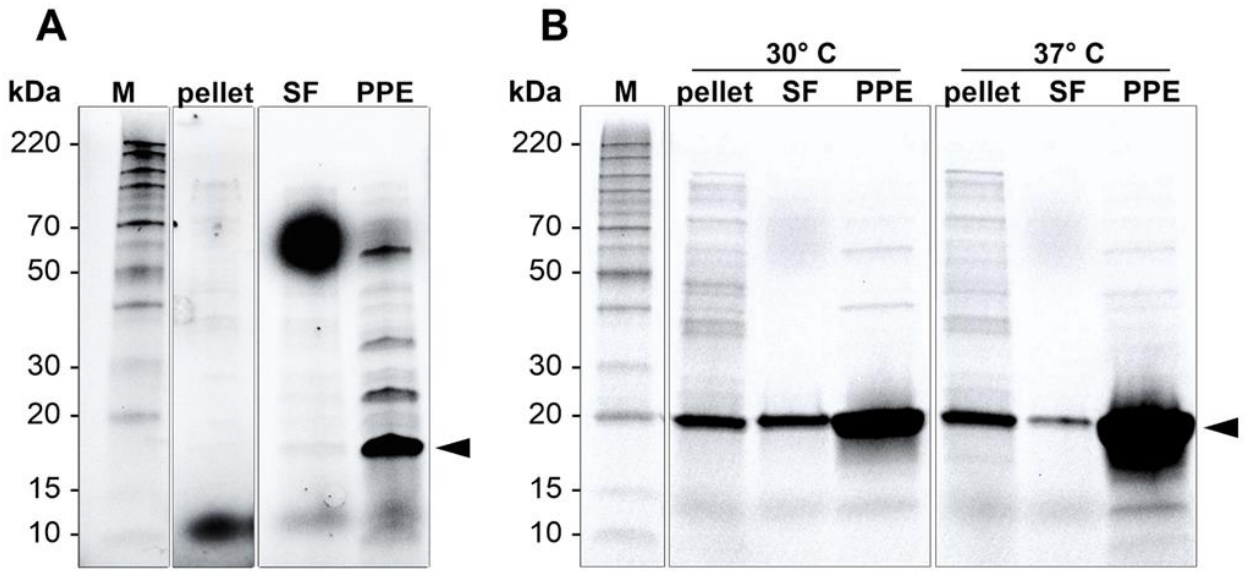

Figure 3.12. SDS-PAGE analysis of *Bl*LPMO10A and *Bs*LPMO10A extraction. SDS-PAGE analysis comparing the protein content in the pellet, sucrose fraction and periplasmic extract resulting from the extraction process of **(A)** *Bl*LPMO10A after overnight expression at 37°C and **(B)** *Bs*LPMO10A after induced expression for 6 hours at 30°C and 37°C. The black sphere observed in the sucrose fraction in (A) represents an artifact. M; marker, SF; sucrose fraction, PPE; periplasmic extract.

3.2.4 Purification of *Bl*LPMO10A and *Bs*LPMO10A

An attempt was made to purify *Bl*LPMO10A from the periplasmic extract using affinity chromatography, where chitin beads were used as the stationary phase (Section 2.34.1). LPMO elution was achieved using acetic acid at pH 3.6. A significant portion of *Bl*LPMO10A was present in the flow-through fraction (Figure 3.13), suggesting that the binding of *Bl*LPMO10A to the chitin beads was not sufficient for effective purification.

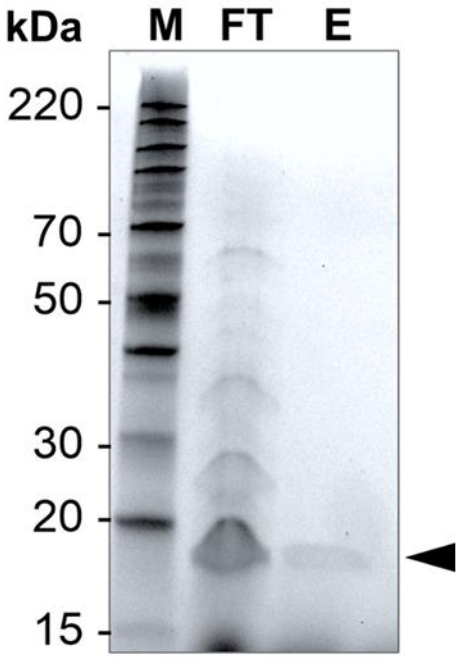

Figure 3.13. Purification of *Bl*LPMO10A using chitin affinity chromatography. SDS-PAGE analysis of flowthrough and eluate fractions resulting from chitin affinity chromatography of *Bl*LPMO10A. M; marker, FT; flowthrough, E; eluate.

Anion exchange chromatography (AEC) was subsequently attempted to purify *Bl*LPMO10A and *Bs*LPMO10A, based on previously successful purification of *Bl*LPMO10A by this approach (Courtade et al., 2015; Forsberg, Røhr, et al., 2014). Given the theoretical isoelectric points (pI) of *Bl*LPMO10A and *Bs*LPMO10A (5.9 and 6.5, respectively), indicating a net negative charge under the experimental conditions (pH 8.0), The periplasmic extracts were adjusted with 20 mM Tris-HCl pH 8.0 buffer and loaded onto the column, before A280 was continuously monitored to track the chromatographic separation of proteins. Non-bound proteins were collected as flow-through in 10 mL fractions, before proteins bound to the column were eluted in 3 mL fractions using a linear salt (NaCl) gradient.

The chromatogram obtained from the purification of *Bl*LPMO10A (Figure 3.14 A) displayed three distinct peaks in A280 absorbance units (mAU), with one prominent peak at 1012 mAU. SDS-PAGE analysis of fractions covering each peak was performed to assess the presence and purity of *Bl*LPMO10A (Figure 3.14 C). *Bl*LPMO10A was primarily detected in the second peak, with elution starting at approximately 5% conductivity and peaking at approximately 12.5% conductivity. Another weak band was observed at >20kDa, which might represent a non-processed version of *Bl*LPMO10A with a non-cleaved signal peptide, corresponding to its predicted size of approximately 22 kDa. Based on the SDS-PAGE analysis, fractions 34-40

were sufficiently pure for downstream applications without requiring additional purification steps such as size exclusion chromatography (SEC). These fractions were pooled, while fractions displaying additional bands (fractions 30-32 and fractions from the third peak) were excluded.

Following successful purification of *Bl*LPMO10A, the same approach was employed for *Bs*LPMO10A (Figure 3.14 B). The chromatogram revealed three distinct peaks, with a notable peak in A280 (1558 mAU) observed in the flow-through. SDS-PAGE analysis of selected fractions (Figure 3.14 D) indicated that *Bs*LPMO10A was primarily present in the flow-through, as shown by a band of approximately 20 kDa, whereas only a faint band was observed in the eluted fractions. Notably, no additional bands were observed above the 20 kDa band for *Bs*LPMO10A, suggesting the absence of non-processed enzyme. Flow-through fractions 4-6 were considered sufficiently pure for downstream applications without necessitating further purification steps.

Following the purification process, pooled fractions of both *Bl*LPMO10A and *Bs*LPMO10A were concentrated, buffer-exchanged to 20 mM Tris-HCl pH 8.0 (Section 2.35), and copper saturated (Section 2.36) to yield high-concentration stock solutions of the holo-enzyme to be used in subsequent activity assays.

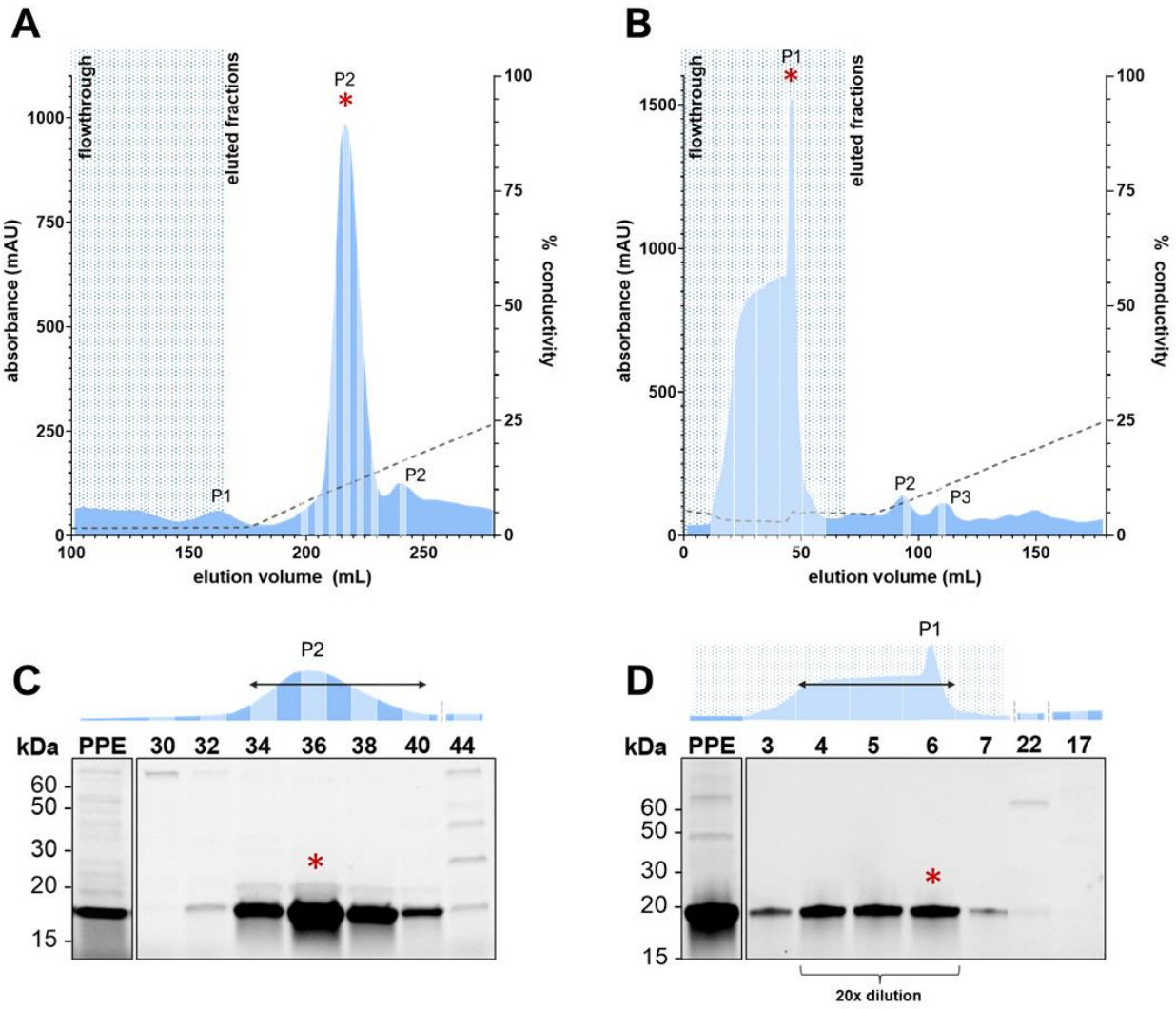

Figure 3.14. Purification of *Bl*LPMO10A and *Bs*LPMO10A using anion exchange chromatography. The chromatogram for **A)** *Bl*LPMO10A and **B)** *Bs*LPMO10A depicts the volume (mL) of solution passing through the column on the x-axis. The left y-axis represents the UV absorbance at 280 nm (A280; blue graph), while the right y-axis indicates the % conductivity as a dotted line. Flowthrough fractions are shaded in gray. Fractions subjected to SDS-PAGE analysis are marked by vertical bars. Peaks are labeled as P1-P3, with the maximum absorbance peak marked by a red asterisk (*). The SDS-PAGE analysis of selected fractions for **C)** *Bl*LPMO10A and **D)** *Bs*LPMO10A display the periplasmic extract (PPE) applied to the column and the analyzed fractions corresponding to vertical bars in the expanded chromatograms displayed above, where arrows span the pooled fractions. The fraction with the maximum absorbance at 280 nm is marked with a red asterisk (*) on the gel. Corresponding protein sizes in kDa are labeled to the left. Note that fractions 4-6 for *Bs*LPMO10A in D) were subjected to a 20x dilution before being applied to the gel, as indicated.

3.2.6 Characterization of *Bs*LPMO10A chitin oxidation by MALDI-ToF MS

Matrix-Assisted Laser Desorption/Ionization-Time of Flight (MALDI-ToF) mass spectrometry (MS) was used to assess the activity of purified *Bs*LPMO10A on β-chitin using *Bl*LPMO10A as a control, using ascorbic acid (AscA) as a reductant.

The resulting MALDI-ToF chromatograms for *Bs*LPMO10A and *Bl*LPMO10A (Figure 3.15 A) showed that the introduction of AscA led to a series of distinct peaks corresponding to the mass of chito-oligosaccharides, specifically those with degrees of polymerization (DP) ranging from 4 to 8. These peaks matched the expected mass-to-charge (m/z) values for oligomers of N-acetylglucosamine (GlcNAc) units, incremented by m/z 203. The degradation profiles observed for *Bs*LPMO10A were consistent with those for *Bl*LPMO10A.

The detailed mass spectra within each peak revealed cation adducts with ionized oligosaccharides, exhibiting peaks for sodium ($[M + Na^+]$) and potassium ($[M + K^+]$) adducts of N-acetylglucosamine oligomers and their C1-oxidized forms. This adduct formation, which is common in MALDI analysis, is due to interactions between cations in the reaction environment and the ionized products, leading to observable shifts in the mass spectrum.

The expanded spectra (Figure 3.15 B) displayed ions indicative of aldonic acid forms with a +16 m/z increase and lactonic forms with a -2 m/z decrease, consistent with C1-oxidized chitooligosaccharides. Conclusively, *Bs*LPMO10A was characterized as chitin-active and C1-oxidizing.

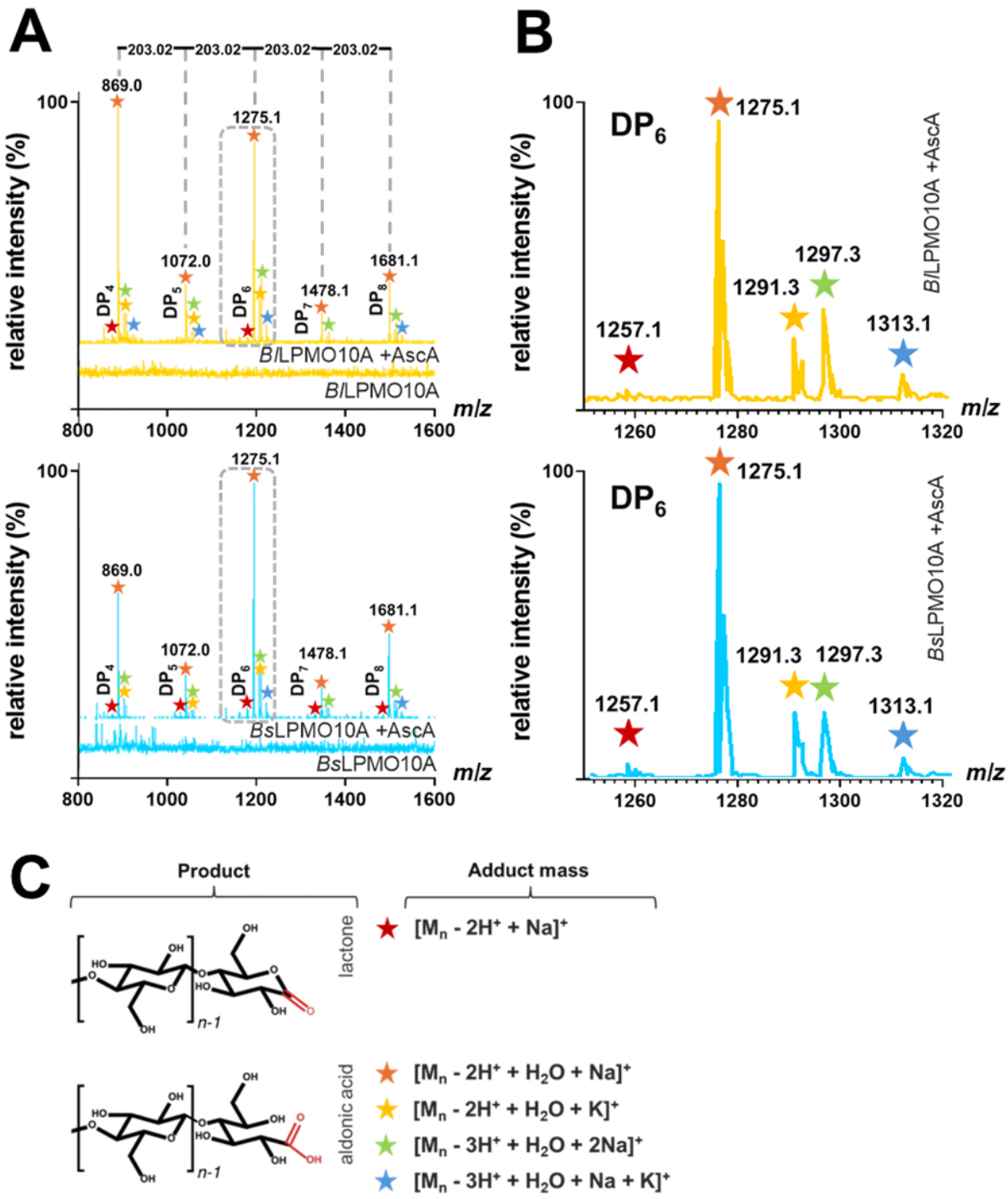

Figure 3.15. MALDI-ToF MS analysis of LPMO activity on β-chitin. Panel **(A)** shows MALDI-ToF mass spectra displaying native and oxidized chitooligosaccharides (DP4-DP8) produced by 1 µM of *Bl*LPMO10A (yellow) and *Bs*LPMO10A (blue) incubated with 10 g/L β-chitin and 1 mM ascorbic acid (AscA), with lower spectra representing control reactions without added AscA. The x-axis represents m/z values ranging from 800 to 1600 with relative intensities on the y-axis. Grey dashed rectangles highlight DP series expanded in Panel B. Masses denoted above peaks correspond to the highest observed intensities within each series, representing the sodium adducts of the aldonic acid form. Panel **(B)** presents an expanded view of the DP6 peak series corresponding to the m/z range of 1250–1320. Peaks are annotated with colored stars corresponding to the various product and adduct forms as detailed in (C), with the mass of each peak labeled accordingly. **(C)** Key for selected C1-oxidized oligosaccharide product forms observed in the mass spectra. Red star: sodium adduct of lactone; orange star: sodium adduct of aldonic acid; yellow star: potassium adduct of aldonic acid; green star: disodium adduct of aldonate; blue star: combined sodium-potassium adduct of the aldonate.

3.2.7 Assessing *Bs*LPMO10A oxidation of cellulose by MALDI-ToF MS

Given that some chitinolytic LPMOs also display activity on cellulosic substrates (Figure 3.11), the enzymatic activity of *Bs*LPMO10A towards phosphoric acid swollen cellulose (PASC) was assessed. *Bl*LPMO10A, previously determined as solely active on chitin (Forsberg, Røhr, et al., 2014), was used as a negative control, whereas the well-characterized ScLPMO10A from *S. coelicolor*, known for its cellulolytic activity and C1 regioselective oxidation of cellulose substrates such as PASC (Forsberg, Mackenzie, et al., 2014), was used as a positive control.

As expected, MALDI-ToF mass spectrometry profiles revealed significant activity of ScLPMO10A on PASC (Figure 3.15 A). Upon addition of AscA, a series of pronounced peaks with m/z values increased by increments of 162 were observed, corresponding to the expected mass-to-charge (m/z) values for oligomers of glucose (Glc) units. Peaks corresponding to m/z 1029.4, 1191.4, 1353.5, and 1515.5 were attributed to sodium adducts ([M + Na+]) of cello-oligosaccharides ranging from Glc4 to Glc8, along with their C1-oxidized counterparts, confirming the presence of both aldonic acid (+16 m/z) and lactone (-2 m/z) forms.

The mass spectra for *Bs*LPMO10A (Figure 3.15 B) showed no comparable peaks upon addition of AscA, similar to the negative control *Bl*LPMO10A (Figure 3.15 C). The absence of the characteristic oligosaccharide peaks seen in the positive control suggests *Bs*LPMO10A did not catalyze the cleavage of cellulose under the tested conditions.

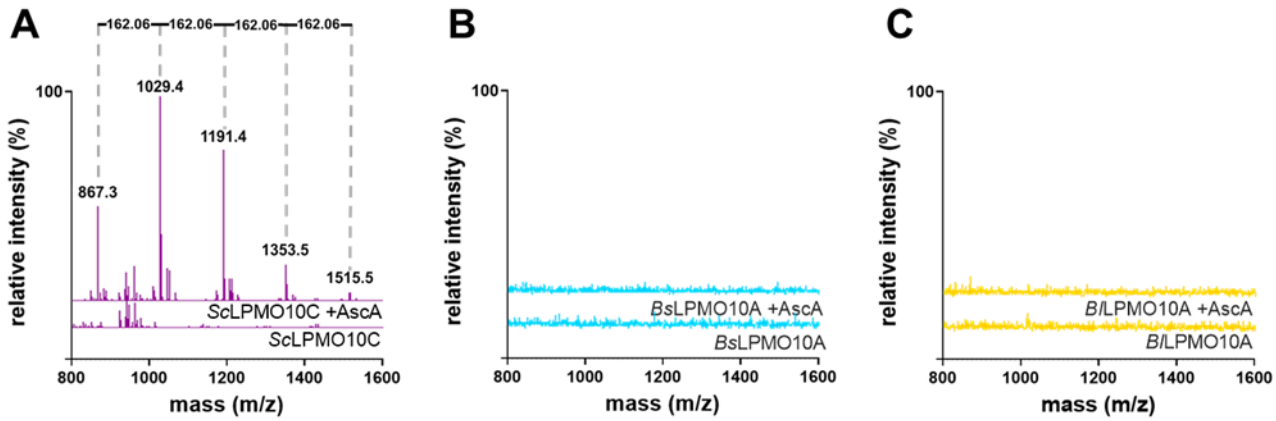

Figure 3.16. MALDI-ToF MS analysis of LPMO activity on PASC. MALDI-ToF mass spectra of soluble fractions after incubation of 1 µM (A) ScLPMO10A, (B) *Bs*LPMO10A and (C) *Bl*LPMO10A with 10 g/L PASC and 1 mM ascorbic acid (AscA), with lower spectra representing control reactions without added AscA. The x-axis represents m/z values ranging from 800 to 1600 with relative intensities on the y-axis.

3.2.8 Assessing LPMO binding affinities to β-chitin and PASC

Substrate binding assays were performed to determine affinities of *Bs*LPMO10A and *Bl*LPMO10A to β-chitin and PASC. *Sm*LPMO10A served as a reference for high-affinity binding (Vaaje-Kolstad, Houston, et al., 2005), whereas BSA served as a control for no binding. Each protein was incubated with β-chitin for 2 hours, and subsequently filtrated to separate bound from non-bound protein. The Bradford assay (Section 2.37.2) was used to quantify the amount of unbound proteins in the filtered supernatant (Figure 3.17 A). Additionally, SDS-PAGE analysis provided qualitative verification of binding by visualizing protein distribution between the pellet and the supernatant fraction after centrifugation (Figure 3.17 B).

Compared to *Sm*LPMO10A, *Bs*LPMO10A and *Bl*LPMO10A showed lower binding capacities to β-chitin. As expected, *Sm*LPMO10A demonstrated high binding affinity, with approximately 95.2% of the protein bound to β-chitin. Conversely, *Bs*LPMO10A demonstrated moderate binding, with about 65.7% of the protein bound. *Bl*LPMO10A showed the lowest binding affinity, with an estimated 56.0% of the protein bound (Figure 3.17 A). Given that no BSA was present in the bound fraction, this confirmed that the observed binding was not due to inadequate pellet washing or other experimental artifacts. No binding affinity was observed for either *Bs*LPMO10A or *Bl*LPMO10A using PASC as a substrate (data not shown).

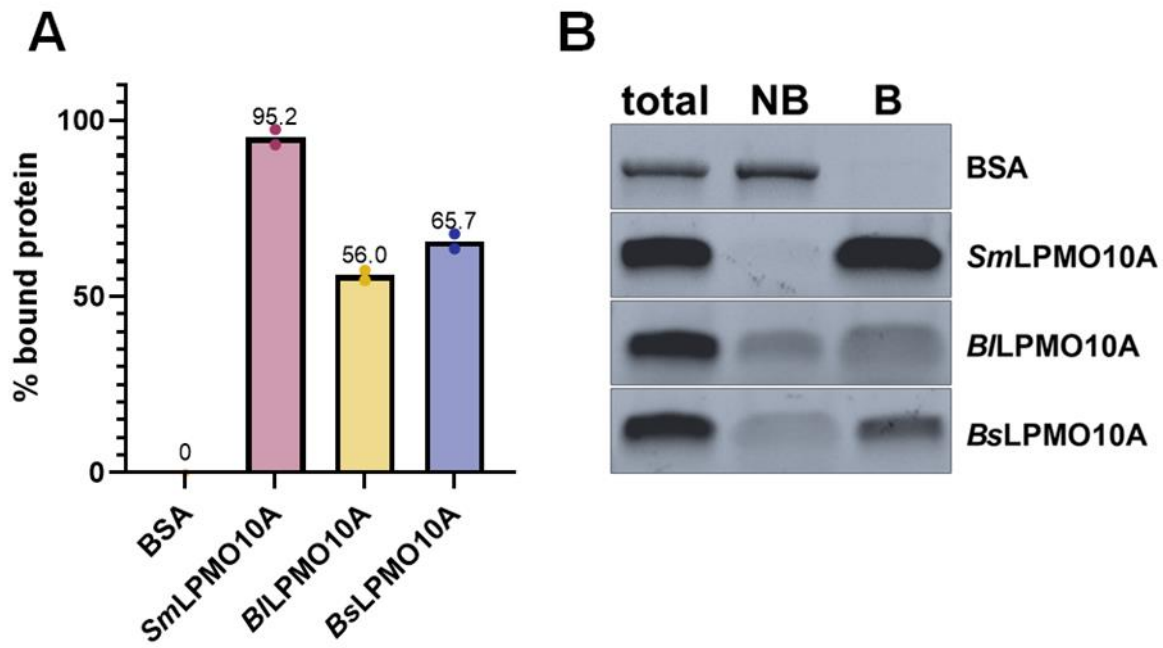

Figure 3.17. Binding affinity of LPMOs to β-chitin. (A) The bar graph presents the quantitative binding affinities of BSA, *Sm*LPMO10A (red), *Bl*LPMO10A (yellow), and *Bs*LPMO10A (blue) to β-chitin, represented as the percentage of bound protein. Each bar represents the mean of two independent experiments, with the average value depicted above each bar and with the individual experiment values indicated by colored points.

(B) Qualitative analysis by SDS-PAGE illustrating protein distribution between non-bound protein in the supernatant (NB) and the bound protein in the pellet (B) fractions. Control samples without β-chitin is shown in the 'total' lane.

3.3. OD_{600} assay effects of LPMOs on *B. licheniformis* cell integrity

In an effort to identify biological activity and potential novel substrates, the study initially examined the potential activity of *Bl*LPMO10A and *Bs*LPMO10A on *B. licheniformis* vegetative cells. An optical density (OD) assay was performed to assess the influence of LPMOs on the integrity of vegetative cells (Section 2.41), with a decrease in OD at 600 nm (OD_{600}) being indicative of cell lysis. *Bl*LPMO10A and *Bs*LPMO10A were added at concentrations of 5 µM to standardized cell suspensions with an OD_{600} of approximately 2.5. Ascorbic acid (AscA) was added as a reductant to ensure the LPMOs were in their catalytically active Cu(I) state, and to compare any effects with inactive LPMOs, control experiments without the addition of ascorbic acid were included.

OD_{600} was continuously monitored over a period of 4 hours (Figure 3.18). Cells displayed a less pronounced OD decline upon the addition of both *Bs*LPMO10A and *Bl*LPMO10A. Furthermore, both LPMOs showed an even less pronounced effect upon the addition of AscA, suggesting that the LPMOs did not significantly impact the integrity of the cells under the conditions tested.

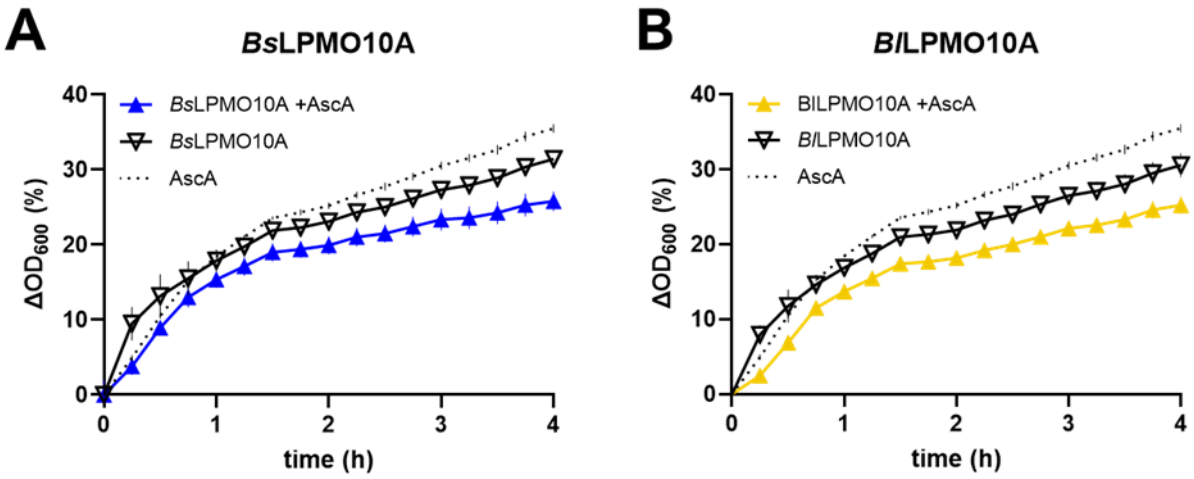

Figure 3.18. Effect of LPMOs on OD_{600} of vegetative *B. licheniformis* vegetative cells. Optical density (OD_{600}) of *B. licheniformis* cells treated with 5 µM of (A) *Bs*LPMO10A and (B) *Bl*LPMO10A in the presence (triangles) or absence (inverted triangles) of 1 mM ascorbic acid were continuously measured every 5 min for 4 hours. Every third datapoint, expressed as relative change (%) in optical density (ΔOD_{600}), is plotted as the mean of three technical replicates ± standard deviation.

After assessing the impact of LPMOs on integrity of *B. licheniformis* vegetative cells, the study proceeded to investigate potential synergistic effects with lysozyme. Initially, a dose-response assay was conducted to evaluate the lytic efficacy of lysozyme on *B. licheniformis* vegetative cells, aiming to establish an effective concentration range for future synergistic assays with LPMOs. Lysozyme concentrations from 0.01 to 2.00 g/L were introduced to standardized cell suspensions with an OD_{600} of approximately 2.5, and the lytic activity was continuously monitored over a 60-minute period. An increase in cell lysis, indicated by a more pronounced decrease in OD_{600}, was observed with each increment in lysozyme concentration (Figure S1A). Figure S1B depicts the dose-response relationship after a 20-minute incubation period. For further experiments involving LPMOs, the two lowest lysozyme concentrations tested (0.01 and 0.1 g/L) were selected to potentially enhance the discernment of any additive or synergistic effects.

To evaluate potential synergistic effects of lysozyme and LPMOs on *B. licheniformis* cell walls, the cells were pre-incubated with 5 µM *Bl*LPMO10A and *Bs*LPMO10A for 8 hours in both the presence and absence of 1 mM AscA, BSA served as a protein control to exclude non-specific protein effects on cell lysis. This was followed by the addition of 0.01 or 0.1 mg/mL lysozyme (Figure 3.19). Cells treated with *Bl*LPMO10A and *Bs*LPMO10A in the presence of AscA exhibited a slight decline in optical density at 600 nm relative to without AscA after addition of 0.1 mg/mL lysozyme. This observation may suggest that *B. licheniformis* cell suspensions pre-incubated with reduced *Bl*LPMO10A and *Bs*LPMO10A exhibited subtle increases in lytic activity following lysozyme treatment, compared to those pre-treated in the absence of ascorbic acid or with BSA.

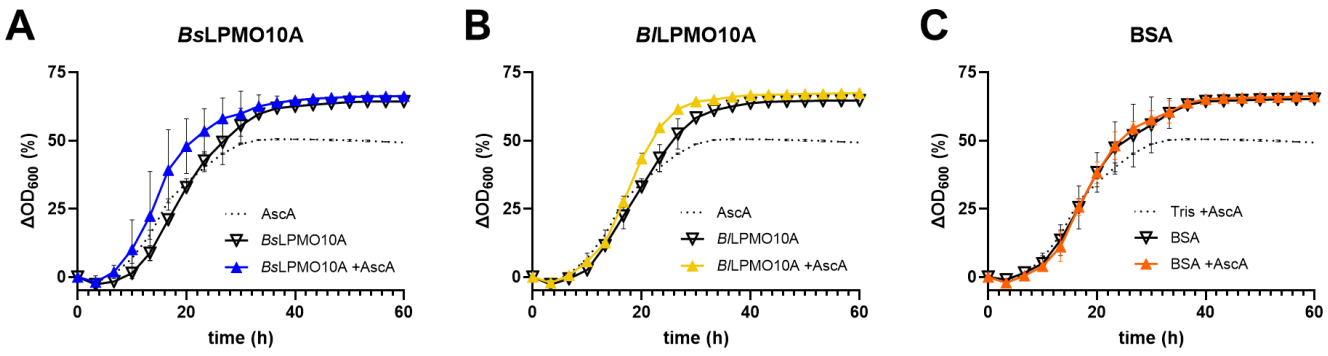

Figure 3.19. Effect of LPMO pre-treatment on lysozyme-induced lysis of *B. licheniformis* cells. Optical density (OD_{600}) of *B. licheniformis* cells pre-treated for 8 hours with 5 µM of (A) *Bs*LPMO10A, (B) *Bl*LPMO10A or (C) BSA in the presence (triangles) or absence (inverted triangles) of 1 mM ascorbic acid was continuously measured every 20 seconds for 60 minutes after exposure to 0.1 g/L lysozyme. Every third datapoint, expressed as relative change (%) in optical density (ΔOD_{600}), is plotted as the mean of three technical replicates ± standard deviation.

3.4. Assessment of endospore germination by measuring DPA release

After assessing the potential activity of *Bs*LPMO10A and *Bl*LPMO10A on vegetative cells and their synergistic interactions with lysozyme, the study shifted its focus towards examining the possibility that these LPMOs could influence the germination of *B. licheniformis* endospores. This hypothesis was informed by a recent study by Qezellou (2023), which suggested a potential role for ScLPMO10D, a β-chitin-active LPMO from *S. coelicolor*, in promoting the germination efficiency and viability of *B. subtilis* endospores.

The germination of *B. licheniformis* endospores was assessed through measuring the release of dipicolinic acid (DPA) marking the onset of germination, leveraging its complexation with terbium (Tb) to generate a fluorescent signal (Section 2.41). Spectral analysis of the fluorescent terbium-dipicolinic acid (TbDPA) complex displayed peak fluorescence at 546 nm emission and 271 nm excitation (Figure S2 A and B). The fluorescence intensity showed a direct linear correlation (R2=0.9991) with DPA concentrations in the tested range (0-250 µM DPA) (Figure S2C). This supported the use of TbCl3 for DPA quantification in subsequent endospore germination assays.

3.4.1. Generation of *B. licheniformis* endospores

The generation of endospores for the assay (outlined in Section 28.1) involved monitoring the growth of *B. licheniformis* (Figure S3 A). A decrease in OD_{600}, signaling the commencement of sporulation, was observed approximately 12 hours after inoculation, as the lysis of vegetative mother cells resulted in a lower optical density. The sporulation process was documented by phase contrast and brightfield microscopy following Schaeffer-Fulton-staining (Figure S3 B and C). Endospores were harvested 3-4 days post-inoculation once over 80% of cells had transitioned to endospores. Endospores were thoroughly washed, and a quantitative assessment of the resulting suspensions revealed concentrations of approximately 1010 endospores per milliliter with over 99% purity, as determined by hemocytometer counting (Section 2.28.1). Unless otherwise specified, the subsequent germination assays used purified *B. licheniformis* endospores (final concentration $5*10^8$ endospores/uL) that had been heat-activated at 75°C for 15 minutes to synchronize germination (Section 2.41).

3.4.2. Effect of LPMOs on endospore germination

The influence of LPMOs on endospore germination was analyzed by real-time fluorescence monitoring of TbDPA. Initial experiments involved incubating heat-activated endospores with 5 µM LPMOs for 4 hours, either alone or in the presence of 1 mM AscA. BSA was employed as a protein control to account for non-specific effects. As depicted in Figure 3.20, samples treated with both LPMOs and AscA demonstrated a significant increase in the fluorescent signal compared to those incubated with LPMOs alone. This increase was similarly observed for both *Bl*LPMO10A and *Bs*LPMO10A. In contrast, control samples treated with BSA showed only minimal fluorescence enhancement, suggesting a specific role of active LPMOs in amplifying the fluorescent signal.

However, the fluorescence signals of all samples containing AscA was significantly significantly lower compared to corresponding samples without AscA at the start of the experiment, which may be due to interference with the signal. The experiment was replicated multiple times and produced consistent results.

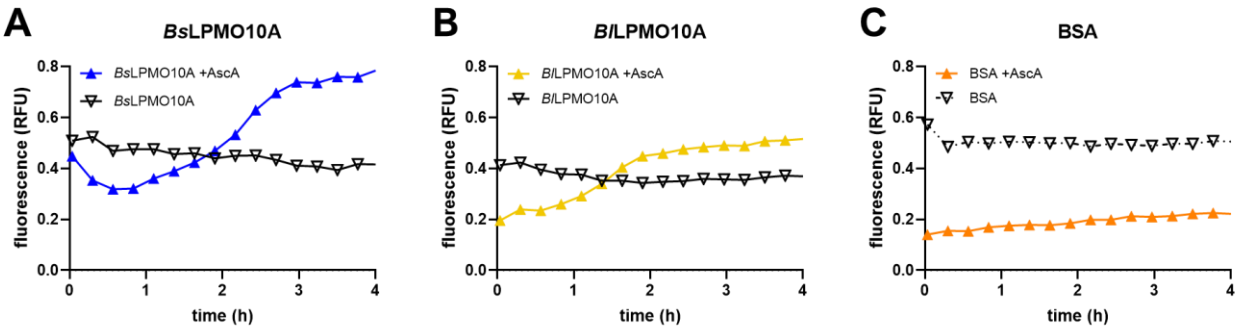

Figure 3.20. Effect of LPMOs on fluorescence response of endospores. TbDPA fluorescence (RFU) of *B. licheniformis* cells treated with 5 µM of (A) *Bs*LPMO10A, (B) *Bl*LPMO10A and (C) BSA in the presence (triangles) or absence (inverted triangles) of 1 mM ascorbic acid was continuously measured every 2 min for 4 hours. Every eighth datapoint is plotted based on a single experimental run.

3.4.3. Effect of ascorbic acid on TbDPA fluorescence

In light of the observed differences in fluorescence signals in initial germination assays between samples with and without AscA, it was necessary to further investigate the potential interaction between AscA and the TbDPA fluorescence. The potential influence of ascorbic acid (AscA) on TbDPA fluorescence was examined by titrating AscA (0-1000 µM) while maintaining the DPA level constant at 250 µM (Figure 3.21 A). This analysis revealed an inverse correlation between AscA concentration and fluorescence intensity, indicating a quenching effect.

Further investigation into the spectral properties of AscA identified a pronounced absorption peak at 265 nm, which extensively overlapped with the excitation spectrum of the TbDPA complex (Figure 3.21 B). This overlap suggested that competitive absorption could have led to a diminished fluorescence signal for samples containing AscA in the initial TbDPA germination assays. These findings highlighted the dual role of AscA in both promoting LPMO activity and suppressing fluorescence signals, which added complexity to the interpretation of results. As a result, modifications to the experimental protocol were necessary to circumvent this issue.

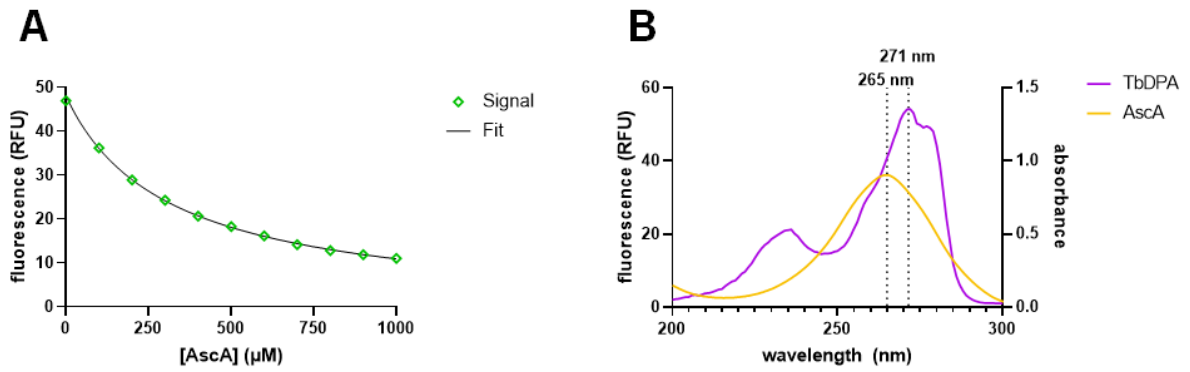

Figure 3.21. Interference of ascorbic acid on TbDPA fluorescence. (A) Dose-response curve showing the effect of increasing concentrations of ascorbic acid (AscA) on the TbDPA fluorescence signal. The data points (diamonds) represent the measured signal, while the solid line indicates the fitted trend demonstrating the inverse relationship. **(B)** Comparison of absorbance spectra between TbDPA and AscA. The TbDPA complex displays a peak at 271 nm, while AscA displays maximum absorbance at 265 nm. The purple line represents the TbDPA excitation spectrum, while the orange line corresponds to AscA absorbance spectrum. The absorbance spectrum of AscA is attained from Yang et al. (2006).

3.4.4. Reducing AscA concentrations: implications for LPMO effect on TbDPA fluorescence

The quenching effect of ascorbic acid (AscA) on TbDPA fluorescence signals instigated an exploration of alternative reductants such as DTT, L-cysteine, and gallic acid at varying concentrations. These alternatives, however, either showed unpredictable effects on fluorescence signals or, in the case of L-cysteine, exhibited dual functionality as both reductants and endospore germinants, complicating assay interpretation (data not shown). Consequently, AscA was examined more closely with a reduced concentration from 1 mM to 100 µM to investigate whether the quenching effect could be mitigated while attempting to maintain sufficient LPMO activation.

This adjustment effectively lessened the pronounced quenching effect previously observed with 1 mM AscA (Figure 3.20) and the initial discrepancy in fluorescence signal between samples with and without AscA. However, at this lower AscA concentration, the signal increase

previously associated with LPMOs plateaued more rapidly. The dependency of the initial signal increase on AscA concentration suggested that it might be predominantly due to LPMO-mediated AscA oxidation rather than an increase in DPA release during germination.

While the initial fluorescence increase observed with LPMOs and AscA was attributed to AscA depletion, the signal intensity in these samples exceeded control levels without AscA, indicating potential enhanced germination.

This was further supported when additional experiments incorporating L-alanine revealed potential synergistic effects. Similar to assessing synergy with lysozyme on cell integrity in Section 3.3, 50 µM L-alanine was found to induce observable but minimal germination and was selected to potentially enhance the discernment of any additive or synergistic effects. This revealed heightened fluorescence signals observed with LPMOs and AscA compared to samples containing either L-alanine alone or only LPMOs and L-alanine.

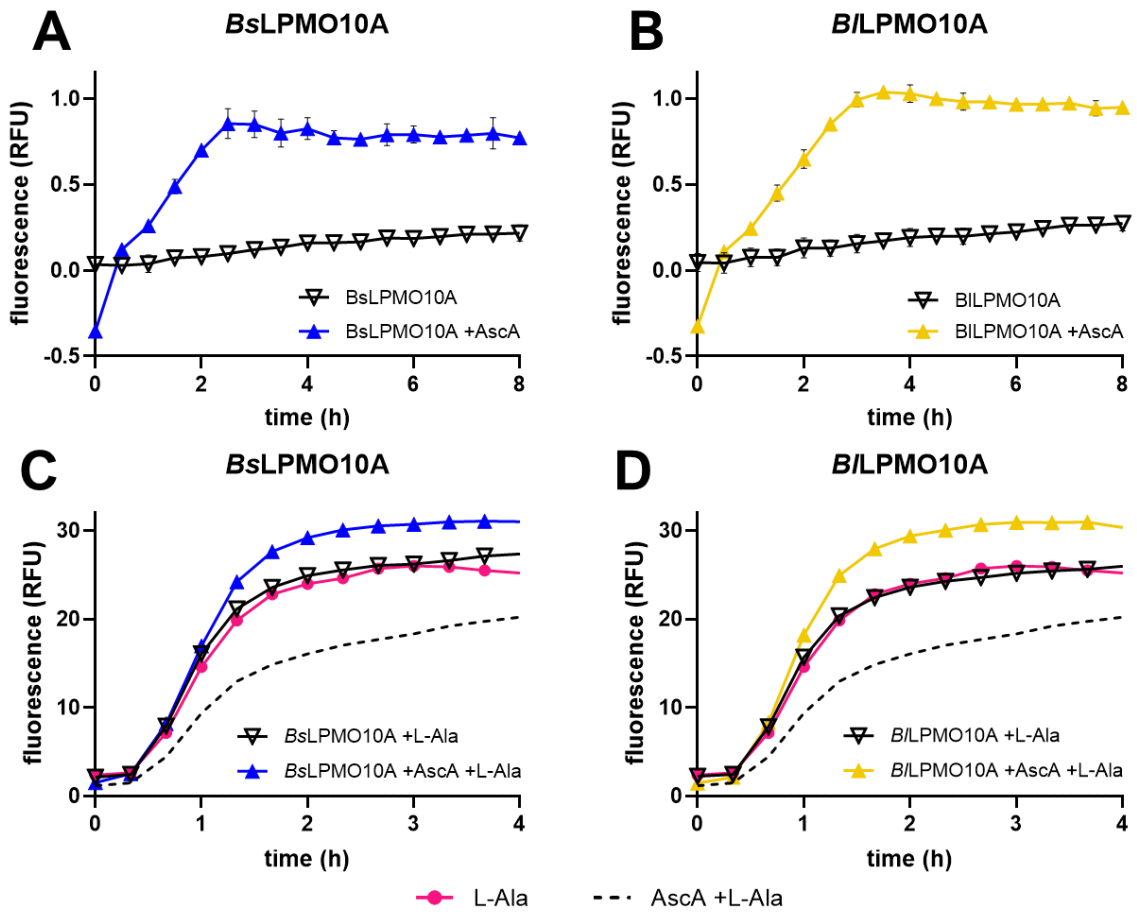

Figure 3.22. Fluorescence monitoring of LPMO effect on endospore germination at 100 µM AscA. TbDPA fluorescence (RFU) of endospores treated with 5 µM of (A) *Bs*LPMO10A or (B) *Bl*LPMO10A in the presence (triangles) or absence (inverted triangles) of 1 mM ascorbic acid was continuously measured every 2 min for 8 hours. Every 15th datapoint is plotted based on a single experimental run. TbDPA fluorescence (RFU) of endospores treated with 100 µM L-alanine (L-Ala) and 5 µM of (A) *Bs*LPMO10A or (B) *Bl*LPMO10A in the

presence (triangles) or absence (inverted triangles) of 1 mM ascorbic acid was continuously measured every 2 min for 4 hours. Every 10th datapoint is plotted based on a single experimental run. All results are blank-subtracted using the signal obtained from endospores alone.

3.4.5. Differentiating between AscA depletion and endospore germination impact on fluorescence increase

The increased signal intensity observed in TbDPA germination assays for endospores treated with LPMOs and AscA might be influenced by factors other than DPA release from endospores and the reduced quenching effect as AscA is consumed by LPMOs. Other factors, such as H_2O_2 formation, copper release from LPMOs, or AscA decomposition products, could artificially inflate the fluorescence signal if absorbing at the TbDPA emission wavelength (545 nm). To differentiate between fluorescence increases specific to endospore germination and those potentially due to an accumulation of assay-specific byproducts, β-chitin was used as a substrate in place of endospores.

A baseline fluorescence signal for β-chitin samples was established by adding 50 µM DPA, resulting in a signal intensity comparable to that seen with untreated endospores, before adding 100 µM AscA and monitoring fluorescence over 1.5 hours (Figure 3.23). The results showed that samples containing *Bs*LPMO10A and AscA exhibited an initial rapid increase in signal before plateauing (Figure 3.23), similar to that observed in germination assays (Figure 3.20 and Figure 3.22). However, no further fluorescence increase was observed when *Bs*LPMO10A was combined with AscA and β-chitin, in contrast to that observed with AscA and endospores. Similar results were seen when using PASC as a substrate and with *Bl*LPMO10A in place of *Bs*LPMO10A (results not shown). Due to the low concentrations of AscA used, its unikely that the plateauing in signal is due to LPMO inactivation and is rather due to complete depletion of AscA. These findings suggest that the enhanced fluorescence not explained by reduced quenching due to AscA consumption is likely related to DPA release from endospores. However, the potential influence of assay-specific byproducts on the germination process itself was not determined.

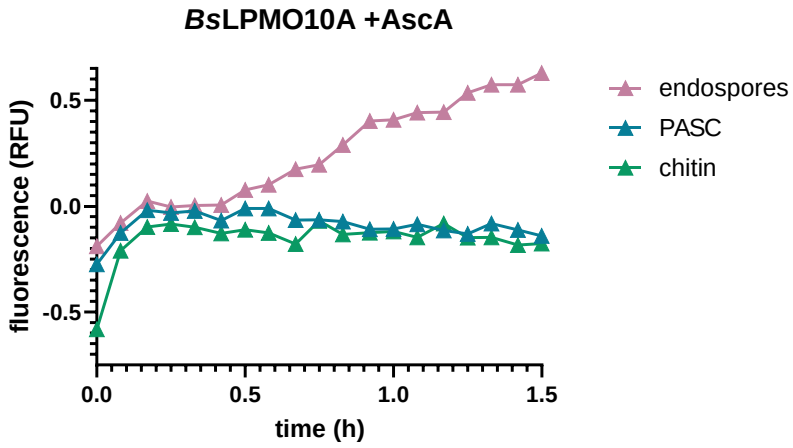

Figure 3.23. Real-time fluorescence monitoring of TbDPA fluorescence with various substrates treated with *Bs*LPMO10A in the presence of 100 µM AscA. TbDPA fluorescence (RFU) of 5 µM *Bs*LPMO10A treatment of endospores (pink), PASC + 50 µM DPA (blue), and β-chitin + 50 µM DPA (green) in the presence of 100 µM ascorbic acid was continuously measured every minute for 1.5 hours. Every fifth datapoint is plotted based on a single experimental run. All results are blank-subtracted using the corresponding signal obtained from samples in the absence of LPMOs and AscA.

3.5. Assessing potential LPMO binding via ascorbic acid consumption

The quenching effect of ascorbic acid (AscA) on the TbDPA signal was repurposed to assess binding and potential activity of *Bs*LPMO10A and *Bl*LPMO10A on endospores and other substrates. As outlined in Section 1.1.2, reduced LPMOs autocatalytically inactivate at a higher rate in the absence of a substrate, which leads to the release of copper from the active site. Using AscA as a reductant results in an accelerated inactivation of LPMOs due to the rapid oxidation of AscA by the free copper, which produces H_2O_2 as an LPMO co-substrate. As more LPMOs are inactivated and more copper is released, AscA consumption increases (Kuusk & Väljamäe, 2021; Stepnov et al., 2022; Stepnov et al., 2021). There is a clear link between substrate affinity and LPMO inactivation rate, and enzyme inactivation can be detected by analyzing the rate of AscA consumption (Bissaro & Eijsink, 2023; Forsberg & Courtade, 2023; Østby et al., 2023). This led to the hypothesis that the concentration of AscA could be determined by quantifying the decrease in TbDPA signal due to the quenching effect of AscA, and the rate of AscA consumption could be used to assess potential substrate binding by LPMOs. Accurate AscA quantification was ensured by a dose-response curve showing predictable signal quenching across the typically used concentration range of 0-1 mM (Figure 3.21 A; $R^2 = 0.9988$).

The approach of indirectly assessing binding affinity by measuring the rate of AscA consumption was initially tested for *Sm*LPMO10A combined with AscA and consistent DPA

concentrations, with β-chitin as a positive control for binding and PASC as a negative control. Results indicated an accelerated depletion of AscA in the presence of PASC compared to β-chitin (data not shown), potentially reflecting the differential binding capacities of CBP21 to these substrates.

After initial tests demonstrated that AscA depletion assessed by TbDPA quenching accurately reflected substrate affinities for *Sm*LPMO10A, further tests were conducted using *Bl*LPMO10A and *Bs*LPMO10A (Figure 3.24). These tests aimed to examine potential binding to endospores over 10 hours, using β-chitin as a positive control and no substrate or PASC as negative controls. To minimize the influence of spontaneous or potential LPMO-induced germination on the signal, non-heat-activated endospores were used at a higher concentration (10^9 spores/uL) before the addition of 1 mM AscA. The results revealed rapid AscA depletion after approximately 2.5 hours in samples without substrate or with PASC, but slower depletion in samples with β-chitin or endospores, potentially reflecting LPMO binding to these substrates. After 10 hours, no significant differences in depletion rates were observed between β-chitin and endospores, indicating no observed substrate preference. Concurrent OD_{600} measurements suggested that germination effects, which could potentially result in artificially low estimated AscA concentrations in endospore samples due to DPA-specific signal increase, did not significantly influence the fluorescence measurements.

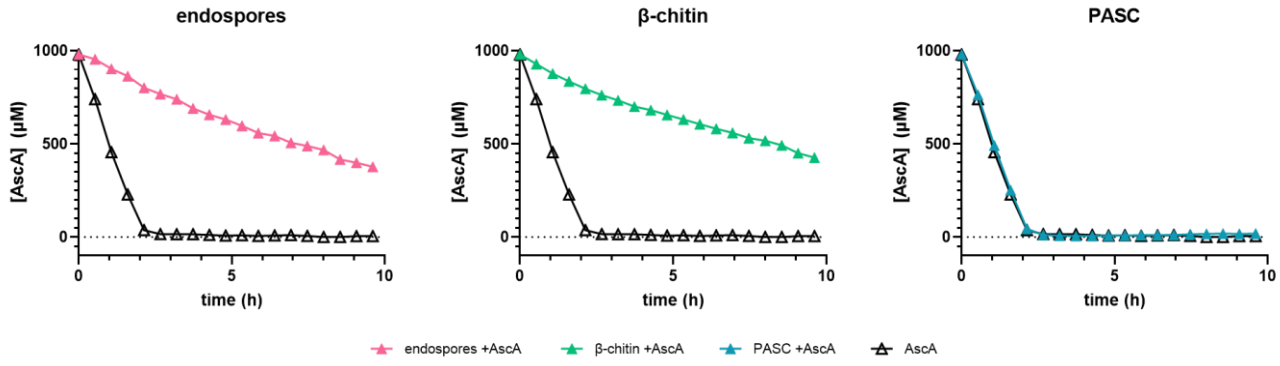

Figure 3.24. AscA consumption profiles of *Bs*LPMO10A with different substrates. TbDPA fluorescence of 1 µM *Bs*LPMO10A incubated with endospores (pink), β-chitin + 50 µM DPA (green), PASC + 50 µM DPA (blue), or 50 µM DPA (black) in the presence of 1 mM ascorbic acid was continuously measured every 2 min for 10 hours. Every 16th datapoint, expressed as estimated AscA concentrations based on a dose-response curve (Figure 3.21), is plotted based on a single experimental run.

3.6. Optical density assay for assessing LPMO effect and L-Alanine synergistic effects during endospore germination

An optical density assay was conducted to further examine the effect of LPMOs on bacterial endospore germination and potential synergistic effects with L-alanine. OD_{600} reduction corresponds to endospore germination, characterized by the transition from phase dark to phase bright, with complete population germination resulting in approximately 55% reduction (Kochan Travis et al., 2018)

The decrease in OD_{600} was monitored over 1.5 hours after the addition of *Bs*LPMO10A, *Bl*LPMO10A, and *Sm*LPMO10A, in both the presence and absence of ascorbic acid (AscA) (Figure 3.25). No-protein controls exhibited no significant difference in OD_{600} reduction between those with (84.6%) and without (82.2%) AscA (data not shown), indicating that AscA alone did not significantly influence germination or the OD_{600} signal.

In the absence of AscA, the addition of *Sm*LPMO10A, *Bs*LPMO10A, and *Bl*LPMO10A led to a more pronounced OD_{600} reduction (74.8%, 72.2%, and 63.1% respectively) compared to the no-protein controls. This reduction was most noticeable with *Bl*LPMO10A. this was also observed for BSA (data not shown) although to a lesser degree. since LPMOs are inactive Cu(II) version, this decrease in OD_{600} might represent effects not attributed to LPMO activity, but to other effects such as increased clustering/clumping of endospores, potentially due to LPMO binding either specifically or through non-specific interactions such as hydrophobic effects.

In the presence of 100 uM AscA, a slight further reduction in OD_{600} was observed for endospores treated with *Bs*LPMO10A and *Bl*LPMO10A (64.9% and 60.9% respectively), but not for *Sm*LPMO10A (76.8%). This reduction upon addition of AscA was most noticeable with *Bs*LPMO10A. as this was observed only for these LPMOs and not *Sm*LPMO10A; it might suggest a reduction in OD specific to the activity of these LPMOs.

Similar to lysozyme in Section 3.3, 50 µM L-alanine was found to induce observable but minimal germination and was selected to potentially enhance the discernment of any additive or synergistic effects.

The addition of 100 µM L-alanine to the assay brought about varied effects on OD_{600} (Figure 3.25 D-F). The non-protein controls with L-alanine exhibited no significant difference in OD_{600} reduction between those with (65.1%) and without (66.8%) AscA (data not shown), further indicating that AscA alone did not significantly influence germination or the OD_{600} signal. Upon addition of L-alanine, *Sm*LPMO10A, *Bs*LPMO10A, and *Bl*LPMO10A in the absence of AscA

led to a further endospore OD_{600} reduction (65.1%, 55.1%, and 51.5% respectively) compared to non-protein controls with L-alanine, most prominent with *Bl*LPMO10A. With both L-alanine and AscA, a further slight decrease in OD_{600} was observed for endospores treated with *Bs*LPMO10A and *Bl*LPMO10A (52.7% and 51.7% respectively), but not for *Sm*LPMO10A (69.5%). The most noticeable reduction upon addition of AscA compared to without AscA was observed with *Bs*LPMO10A. however, the difference observed between presence and absence of AscA was greater in the absence of L-alanine, suggesting…

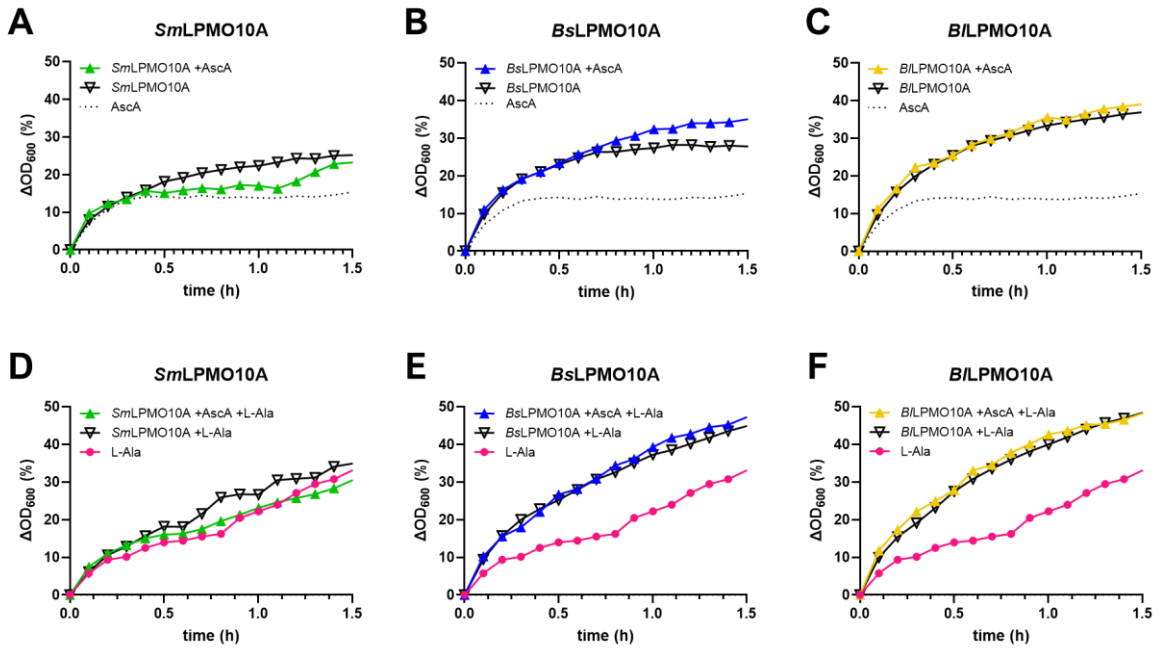

Figure 3.25. Effect of LPMOs on OD_{600} of endospores and on L-Alanine-induced germination. Optical density (OD_{600}) of endospores treated with 5 µM of **(A)** *Sm*LPMO10A, **(B)** *Bs*LPMO10A, or **(C)** *Bl*LPMO10A, and OD_{600} following germination induced by 100 µM L-Alanine (L-Ala) after addition of 5 µM of **(D)** *Sm*LPMO10A, **(E)** *Bs*LPMO10A, or **(F)** *Bl*LPMO10A was continuously measured every 2 min for 1.5 hours. Treatments in the presence (triangles) or absence (inverted triangles) of 1 mM ascorbic acid were compared. Every third datapoint, expressed as relative change (%) in optical density (ΔOD_{600}), is plotted based on a single experimental run.

3.7. Microscopic observation of LPMO impact on endospore germination

Microscopic evaluation was conducted to further investigate the potential effect of LPMOs on bacterial endospore germination. The addition of L-alanine to endospores served as a positive control for visualizing the transition of endospores from a phase-bright to a phase-dark state, a condition indicative of germination. This transition, observable under a microscope, is associated with the initial stages of spore core hydration and DPA release.

Comparative analysis was performed on untreated spores and those treated with LPMOs either with or without AscA following overnight incubation at 37°C (Figure 3. 26). Results showed that endospores treated with 5 mM L-alanine turned phase-dark as expected, with some endospores still phase bright, and were observed to be larger than untreated endospores. This increase in size is likely due to the swelling of endospores as they undergo hydration (Setlow et al., 2017). Endospores treated with LPMOs in the absence of AscA appeared similar to untreated endospores in terms of brightness and size, whereas endospores treated with LPMOs in the presence of AscA remained phase-bright but appeared to exhibit reduced brightness and were comparable in size to endospores treated with L-alanine. Interestingly, what appeared to be cellular debris, visible to some extent in the figure, was strictly observed for endospores treated with LPMOs in the presence of AscA. Representative microscopic images are shown for endospores treated with *Bs*LPMO10A, with similar results obtained for endospores treated with *Bl*LPMO10A (results not shown).

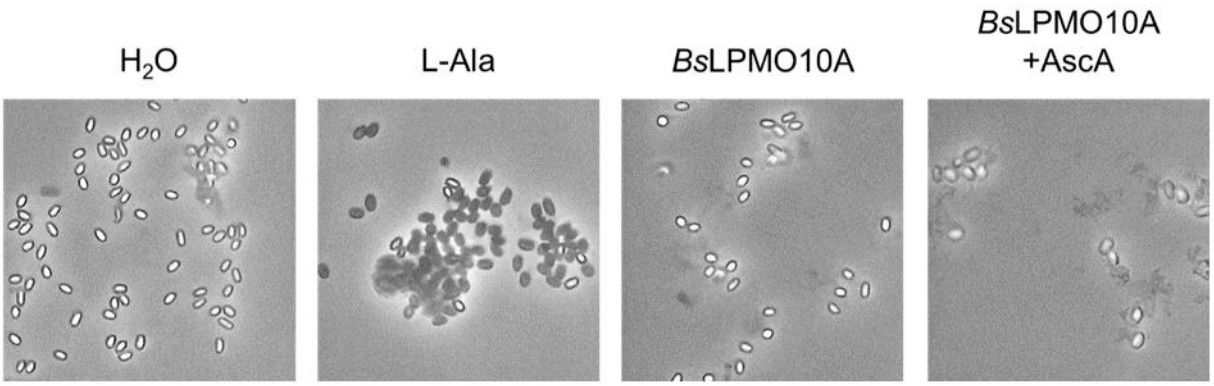

Figure 3. 26. Microscopic analysis of LPMO impact on endospore germination. Comparative analysis of untreated endospores, endospores treated with L-alanine, and endospores treated with LPMOs with or without AscA following overnight incubation at 37°C.

3.8. Assessing binding of LPMOs to endospores

A binding assay was conducted to assess the specificity and affinity of *Bs*LPMO10A and *Bl*LPMO10A for bacterial endospores. To expose the spore cortex and enhance its availability for potential binding, endospores were decoated with an SDS-containing solution (Section 2.43). The cellulose-active *Sc*LPMO10C, representing an LPMO derived from a non-*Bacillus* species, was employed as a reference, and BSA was used as a control for nonspecific binding.

As depicted in Figure 3. 27, the LPMOs demonstrated differential binding affinities for the decoated endospores. BsPMO10A exhibited the highest binding, with 19.8% of the protein

bound, closely followed by *Sc*LPMO10C at 17.3% and *Bl*LPMO10A at 13.6%. However, BSA was also present at a relatively high degree in the bound fraction (8.2%), suggesting the potential contribution of nonspecific interactions to the observed binding. The results may also have been influenced by any residual spore coat proteins present in the decoated endospore solution.

While further insights could have been gained from SDS-PAGE analysis, this approach was not employed in this experiment. It should be noted that these results are based on a single experimental run, and thus the reproducibility of these findings remains to be confirmed in future studies.

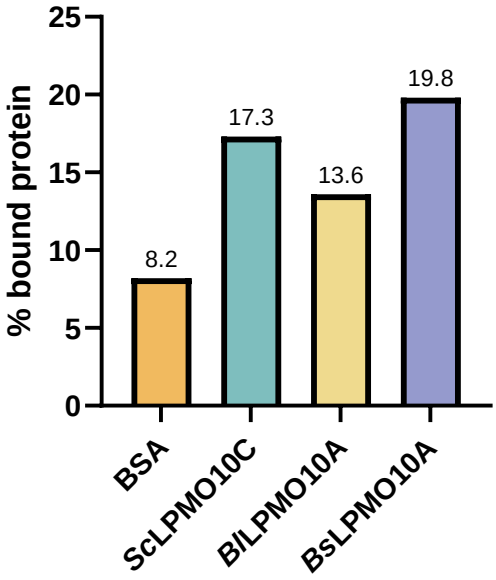

Figure 3. 27. Binding affinity of LPMOs to β-chitin. (A) The bar graph presents the quantitative binding affinities of BSA (orange), *Sc*LPMO10C (green), *Bl*LPMO10A (yellow), and *Bs*LPMO10A (blue) to endospores decoated with an SDS-containing decoating solution, represented as the percentage of bound protein. Each bar represents data obtained from a single experimental run.

4. Discussion

4.1. Fluorescence-based promoter screening in *B. licheniformis*

The study aimed to analyze the expression patterns of LPMO from *Bacillus licheniformis* DSM13 and identify environmental factors influencing its expression using a fluorescence-based promoter screening strategy. Due to the transformants obtained carried a mutation in mCherry that reduced its fluorescence intensity 2-3-fold due to an assumed decrease in protein stability or folding efficiency, recreating of the plasmid without the mutation was attempted. This was attempted several times but proved unsuccessful. This could be due to factors such as the efficiency of In-Fusion cloning, which is influenced by the length and sequence of homology arms. In this study, 15 bp homology arms were used, which are considered optimal for In-Fusion cloning. However, the presence of any secondary structures or repetitive sequences in the homology arms can reduce cloning efficiency. Future work could involve analyzing these homology arms for such features if reattempted cloning remains unsuccessful. Ligation conditions could also contribute to the issue, where factors such as the vector-to-insert ratio and DNA concentration can influence cloning efficiency. Despite extensive trials with different ratios and amounts in this study, it may still be necessary to further optimize these conditions to achieve successful cloning.

The screening therefore proceeded with the mutant mCherry, but promoter activity was not observed under various growth conditions in *B. licheniformis*, including growth in BHI and LB medium, as well as in LB medium supplemented with 2% of various carbohydrates including glycogen, glucose, fructose and mannose, as well as during sporulation and germination of endospores. Previous studies have indicated transcriptional activation of *Bl*LPMO10A under fermentation conditions (Wiegand et al., 2013), suggesting that the promoter might be more responsive under such conditions. Future studies could therefore focus on exploring promoter activity in fermentation settings to gain further insights into LPMO expression regulation in *B. licheniformis*.

The potential toxicity of mCherry-K202E was considered as a factor that might influence the observed lack of signal in *B. licheniformis*. However, this was deemed unlikely due to comparable growth observed in *B. licheniformis* transformed with both pPro-mCherry-K202E and the empty vector (Figure 3.7). Yet, the possibility that the mutation might have a greater impact on protein folding and stability in *B. licheniformis* than in *Lactiplantibacillus plantarum*,

which could potentially account for the observed lack of mCherry expression, cannot be discounted.

4.2. Functional divergence of GH18 chitinases in *B. spizizenii* and *B. licheniformis*

Lytic polysaccharide monooxygenases (LPMOs) are recognized for their synergistic activity with GH18 chitinases, but the functions of these enzymes can significantly vary across different species. Many chitinases also have bacteriolytic activity, owing to the structural similarity between the carbohydrate backbones of peptidoglycan and chitin (Ramos & Malcata, 2011), and an analysis of putative GH18 genes encoded by *B. spizizenii* and *B. licheniformis* revealed that the GH18 enzymes identified may primarily function in germination rather than chitin degradation.

However, *B. licheniformis* DSM 13 was observed to host two additional GH18 not observed in *B. spizizenii* that were putatively involved in chitin degradation, which might rather indicate a role for *Bl*LPMO10A in chitin degradation. However, in a previous study by Manjeet et al. (2013), the expected synergistic interaction between *Bl*LPMO10A and one of these chitinases was not observed. This lack of synergy was not attributed to a deficiency in LPMO activity on chitin, but rather to the enhanced efficacy of the chitinase itself, which demonstrated superior performance on chitin substrates compared to chitinases from *Bacillus thuringiensis* and *Serratia proteamaculans* (Manjeet et al., 2013). The high efficacy of the chitinase and lack of synergy with LPMOs in *B. licheniformis* suggest a chitinolytic system that may function optimally without the need for LPMO enhancement. But it cannot be excluded that *Bl*LPMO10A perhaps is involved in chitin degradation in *B. licheniformis*, not unlikely given the high presence of fungi-derived chitin in soil, and furthermore it could possess dual substrate specificity in acting on both chitin and the cortex of endospores.

The observations made from analyzing the putative GH18 genes encoded by *B. spizizenii* and *B. licheniformis* support the main hypothesis of this study that the LPMOs in *B. spizizenii* and perhaps also in *B. licheniformis* may have evolved to perform roles beyond chitin degradation and might be involved in the germination of endospores.

4.3. Structural analysis of *Bs*LPMO10A reveals similarities with *Ba*LPMO10A from *B. amyloliquefaciens*

The study turned its focus towards the structural elucidation and alignment of *Bs*LPMO10A, a previously uncharacterized LPMO from *B. spizizenii*. Structural alignment of *Bs*LPMO10A with characterized AA10 LPMOs highlighted its similarity with chitin-active LPMOs, including conservation of substrate-binding surface residues shared with other chitin-active LPMOs.

*Bs*LPMO10A exhibited higher structural similarity with *Ba*LPMO10A from *Bacillus amyloliquefaciens* DSM 7 than with *Bl*LPMO10A.This is in line with *Bs*LPMO10A and *Ba*LPMO10A's closer phylogenetic relationship, as established by multiple sequence alignment of the 16S sequences of the strains from which these LPMOs are derived (data not shown). Still, *Bs*LPMO10A exhibited a relatively high structural divergence from *Bl*LPMO10A based on what might have been anticipated given their close phylogenetic relationship compared to the other characterized LPMOs, many of which exhibited similar levels of scored similarity. This might reflect what has previously been observed in phylogenetic studies that the LPMO phylogenetic tree does not seem to follow taxonomy-based classification (Voshol et al., 2019).

Further structural comparison provided insights into the potential factors leading to the observed structural divergence between *Bs*LPMO10A and *Bl*LPMO10A (Figure 3.11), particularly notable by the larger L2 loop in *Bs*LPMO10A compared to both *Bl*LPMO10A and *Sm*LPMO10A. This is a characteristic that has previously been described in *Ba*LPMO10A (2YOY) (Forsberg, Mackenzie, et al., 2014), likely explaining much of their increased structural similarity. In addition, *Bs*LPMO10A features an alternative aromatic residue – specifically a tryptophan instead of a tyrosine – situated slightly upstream in the amino acid sequence compared to the tyrosine found in the other compared LPMOs. This is equivalent to what was previously observed in *Ba*LPMO10A, where Trp23 in the larger L2 loop of *Bs*LPMO10A corresponds to Trp50 in *Ba*LPMO10A (Forsberg, Mackenzie, et al., 2014). These variations, namely a larger L2 loop and a different aromatic residue, might indicate unique evolutionary adaptations in *Bs*LPMO10A and *Ba*LPMO10A compared to *Bl*LPMO10A.

4.4. Heterologous expression and purification of *Bl*LPMO10A and *Bs*LPMO10A achieved by anion exchange chromatography

*Bl*LPMO10A and *Bs*LPMO10A were successfully expressed in *Escherichia coli* and fractionated using cold osmotic shock to extract periplasmic LPMOs. Initial attempts to purify *Bl*LPMO10A using chitin affinity chromatography were suboptimal, suggesting low binding of *Bl*LPMO10A to the chitin beads and that this approach may not be the most effective purification strategy for *Bl*LPMO10A.

Subsequently, anion exchange chromatography (AEC) was used to purify both proteins, informed by their theoretical isoelectric points (pI) of 5.9 for *Bl*LPMO10A and 6.5 for *Bs*LPMO10A being below the experimental pH of 8.0 used. Although SDS-PAGE confirmed successful purification of *Bl*LPMO10A, it revealed another larger protein, likely the non-processed form with a non-cleaved signal peptide. This suggests it might originate from the intracellular space due to potential cell lysis during extraction, and highlights the importance of optimizing extraction protocols to minimize contamination from intracellular contents, ensuring that the purification process yields mature, functionally relevant proteins for downstream applications.

*Bs*LPMO10A, although successfully purified, did not bind well to the column despite being expected to exhibit a net negative charge, and was mainly found in the flow-through, possibly influenced by its higher theoretical pI as illustrated by its less negative surface charge compared to *Bl*LPMO10A, and the actual pI of a protein might deviate substantially from its theoretical pI. Additionally, the high expression levels of *Bs*LPMO10A observed might have overloaded the column, where the amount of protein exceeds its binding capacity, leading proteins ending up in the flow-through.

4.5. Experimental validation of *Bs*LPMO10A chitinolytic activity but suboptimal binding

*Bs*LPMO10A demonstrated activity on chitin but showed suboptimal binding affinity compared to *Sm*LPMO10A. This was similar to *Bl*LPMO10A, which exhibited low binding to chitin as illustrated in both affinity chromatography and substrate-binding assays. However, the presence of non-processed *Bl*LPMO10A with a signal peptide could affect binding properties and potentially lead to an underestimation of binding affinity than if pure mature enzyme had been used. Nonetheless, the low binding affinity of *Bl*LPMO10A for both α- and β-chitin has been

previously demonstrated (Manjeet et al., 2013), suggesting the estimated low affinity is likely accurate.

Despite the lack of observed cellulose activity from *Bs*LPMO10A and *Bl*LPMO10A, it cannot be definitively ruled out that they could influence cellulose degradation. This notion is informed by recent findings concerning the closely related BaLPMO10 from *B. amyloliquefaciens* H-1. Despite originating from a different strain than the one structurally characterized, it shares more than 97% protein sequence identity with *Ba*LPMO10A used in the structural alignment in Figure 3.11, and as previously discussed, *Ba*LPMO10A exhibits substantial structural similarity with *Bs*LPMO10A. Although BaLPMO10 demonstrated a strong preference for chitin and exhibited no activity on cellulose alone, it was shown to slightly enhance cellulose degradation when synergistically paired with cellulases, resulting in a 7% increase in the reducing sugar yield (Guo et al., 2022). This finding suggests that *Bs*LPMO10A might have the potential to aid in cellulose breakdown when combined with cellulases, despite the absence of degradation products from its individual effect in this study, and presents a potential avenue for future research.

4.6. LPMOs could potentially enhance lysozyme-mediated peptidoglycan breakdown in vegetative cells

Given the structural similarity between the carbohydrate backbones of peptidoglycan and chitin, and the observation that many chitinases also have bacteriolytic activity (Ramos & Malcata, 2011), its natural to speculate LPMOs may play a role in the controlled degradation of peptidoglycan, which is crucial for cell growth, division, and remodeling, as recently demonstrated in *S. coelicolor* (Zhang et al., 2022). In experiments with vegetative *B. licheniformis* cells, LPMOs did not enhance degradation under the tested conditions. However, when cells were pretreated with LPMOs and AscA, what might indicate a potential enhancement of lysozyme's lytic effect was observed that suggested the active, reduced form of LPMO might contribute to increased lytic activity.

However, the potential of H_2O_2 and reactive oxygen species (ROS) production – byproducts of AscA consumption enhanced by LPMO activity – in potentially oxidative damage of cells and increased rate of spontaneous lysis was hypothesized to play a role in the observed results. Such an accumulation of ROS could potentially destabilize vegetative cells. Future experiments should aim to clarify the specific oxidative effects on vegetative cells attributable to H_2O_2 and

ROS in order to provide a clearer understanding of whether the observed decreases in OD_{600} in assays with vegetative cells are due to specific LPMO activity or oxidative damage resulting from H_2O_2 and ROS accumulation.

In conclusion, although a slight but significant difference in rate of OD decline was observed between the active and inactive forms of LPMOs, these results are preliminary and require further testing and controls to determine the specificity of LPMO activity. Future research should focus on optimizing conditions to observe potential specific LPMO-induced effects on peptidoglycan breakdown more clearly.

4.7. LPMOs may enhance germination of endospores

Building on the findings with vegetative cells, the study further explored the potential role of LPMOs in facilitating cortex peptidoglycan degradation during the germination of *Bacillus* endospores. This was inspired by a recent study by Qezellou (2023), suggesting a potential role for ScLPMO10D, a β-chitin-active LPMO from *S. coelicolor*, in enhancing the germination efficiency and viability of *Bacillus subtilis* endospores. Additionally, the discovery that GH18 present in *B. spizizenii* and *B. licheniformis* are putatively involved in endospore germination led to the hypothesis that their LPMOs could assist these glycosidases in cortex degredation during germination.

4.7.1. Insights gained from TbDPA germination assays

Initial assays utilizing terbium dipicolinic acid (TbDPA) suggested an increase in fluorescence upon LPMO treatment, which was initially interpreted as a direct effect on endospore germination. However, subsequent analysis revealed that this signal enhancement was likely influenced by the consumption of ascorbic acid (AscA) by LPMOs during the reduction from their Cu(II) state to their active Cu(I) state. As ascorbic acid significantly quenches the fluorescent signal generated by the TbDPA complex, and is consumed more rapidly in the presence of LPMOs, these factors considerably complicated the interpretation of the results. Despite these challenges, a slight but consistent fluorescence increase was observed with AscA, indicating a potential effect of LPMOs on germination.

Further investigations explored the potential synergistic effects of LPMOs and L-alanine, hypothesizing that L-alanine could potentially improve LPMO accessibility to the endospore

cortex, or LPMO activity could enhance L-alanine accessibility to germinant receptors. In the presence of AscA, LPMOs seemed to enhance the fluorescence resulting from L-alanine-induced germination (Figure 3.22), which might suggest such a hypothesized cooperative effect in endospore germination, which could potentially enhance both the rate and extent of germination, and might provide an explanation for the observed results.

Despite ambiguities in TbDPA-based germination assays due to AscA quenching, the observation that the enhanced fluorescence was specific to endospore assays and not observed when performed with chitin or PASC as substrates further supported the hypothesis that LPMOs facilitating dipicolinic acid (DPA) release and germination.

Although experiments with alternative substrates confirmed that the fluorescence increase was specific to endospore-containing samples, they also revealed that fluorescence continued to rise even after AscA depletion. Experiments with chitin or PASC indicated that the signal increase specific to AscA consumption subsided after 10-15 minutes when using 100 µM AscA, and as it was assumed this plateau was not due to LPMO inactivation, it was rather attributed to the complete depletion of AscA. Consequently, the persistent fluorescence increase in endospore assays prompted further investigation into how LPMOs could possibly facilitate germination after AscA, its presumed only source for continued reduction of LPMOs from their Cu(II) to Cu(I) states, is depleted. Recent findings suggest that the spontaneous degradation of dehydroascorbic acid (DHA), the oxidized form of AscA, produces redox-active derivatives that generate hydrogen peroxide, thereby sustaining LPMO activity (Stepnov et al., 2022). This degradation could thus maintain LPMO activity on endospores. Another possibility is that the release of calcium dipicolinate (Ca^{2+}DPA) or peptidoglycan fragments from germinating spores potentially catalyzed by LPMO activity might stimulate germination in neighboring endospores even after LPMO activity subsides due to AscA depletion.

The increase in signal observed in TbDPA-based germination assays, which was specific to samples containing endospores, indicated DPA release potentially due to endospore germination. However, the definitive cause of DPA release from spores remained elusive. The hypothesis considering the role of H_2O_2 and reactive oxygen species (ROS) in potentially damaging vegetative cells was extended to endospores, where the triggering of DPA release independently of germination due to ROS accumulation was investigated. Given the robust resistance of endospores to oxidative stress, it was hypothesized that the potential for H_2O_2 and ROS to independently trigger DPA release from endospores would be minimal. This idea was

supported by the experimental setup, which at most would generate H_2O_2 levels significantly below those required to compromise endospore viability.

Extensive literature further supports this conclusion. Even when subjected to lethal H_2O_2 concentrations, the inner membrane permeability barriers of endospores remains largely intact, with only minimal DPA release (Setlow et al., 2003). Moreover, it has been shown that endospores treated with hydrogen peroxide can still initiate the initial steps of germination, although at a reduced pace (Setlow et al., 2003). This suggests that oxidative damage resulting from unproductive LPMO activity is unlikely to enhance any spontaneous germination of endospores in the assay. Given these observations, it appears plausible that the potential oxidative stress induced by LPMO activity, specifically through the accumulation of H_2O_2 and ROS, may not significantly affect DPA release from endospores.

4.7.2. Insights into potential LPMO-induced effects on germination by measuring the rate of OD_{600} reduction

In the continued exploration of whether LPMOs might influence the germination of *Bacillus* endospores, monitoring the decrease in OD_{600} as endospores germinated was performed, correlating to the transition of endospores from phase bright to phase dark states. *Bl*LPMO10A and *Bs*LPMO10A were observed to contribute to a more pronounced decline in OD_{600} compared to *Sm*LPMO10A, representing an LPMO derived from a non-*Bacillus* species, both in the absence and presence of L-alanine, and was observed in independent repetitions of the experiment. The effect in the presence of ascorbic acid compared to its absence was potentially slightly more pronounced for *Bs*LPMO10A while slightly reduced for *Sm*LPMO10A, and apparently unaffected for *Bl*LPMO10A. For *Bs*LPMO10A, this might suggest an increased decline in OD specific to the active version of the enzyme. However, given that the differences observed are minimal and based on a single replicate, definitive conclusions cannot be drawn about whether the active reduced version of the LPMO specifically contributed to the observed decline in OD_{600}.

Still, the effect of both active and inactive versions of *Bs*LPMO10A and *Bl*LPMO10A compared to *Sm*LPMO10A might be worth investigating. One possible explanation for the greater decline in OD_{600} in the presence of *Bs*LPMO10A and *Bl*LPMO10A compared to *Sm*LPMO10A concerns enzyme hydrophobicity and its impact on interactions between LPMOs and endospores. Surface hydrophobicity might affect how LPMOs and endospores aggregate or disperse in solution, influencing OD measurements. This hypothesis aligns with findings from

Aspholm et al., who suggested that the initial decrease in absorbance was due to spore clustering. However, in silico analyses showed that *Bl*LPMO10A is more hydrophilic than *Sm*LPMO10A, while *Bs*LPMO10A has similar hydrophobicity to *Sm*LPMO10A, indicating that hydrophobicity alone might not be the primary factor in the observed OD_{600} decline. This is especially true considering that *Bl*LPMO10A, which has a more hydrophilic surface, showed the most pronounced decrease in OD along with *Bs*LPMO10A. Therefore, it might be hypothesized that the enhanced reduction in OD_{600} could be due to specific binding interactions with endospores to the endospores, leading to increased clustering and promoting a more pronounced decline in OD_{600}.

4.7.3. Microscopic evaluation might illustrate the effects of LPMOs on endospore germination

The microscopic evaluation of *Bacillus* endospores treated with LPMOs provided crucial insights into the potential effects of these enzymes on endospore germination. The observation that endospores treated with L-alanine as a germinant transitioned from phase-bright to phase-dark, indicating successful germination and core hydration, served as an effective positive control. Endospores treated with LPMOs in the absence of AscA did not exhibit significant changes in endospore brightness or size, suggesting that LPMO treatment alone does not trigger germination, supporting the lack of signal increase observed in TbDPA germination assays, and suggesting the enhance OD_{600} decline in the presence of LPMOs without AscA was not due to increased germination. However, when endospores were treated with LPMOs in the presence of AscA, endospores remained phase-bright but showed reduced brightness and an increased size similar to those treated with L-alanine, appearing similar to what is denoted phase-gray in initial cortex hydrolysis (figure in introduction). This indicated that the reduced phase brightness of endospores and observed size increase was specific to the reduced Cu(I) version of the LPMOs. The observation of what appeared to be cellular debris in samples treated with LPMOs and AscA suggested that LPMO activity could possibly lead to partial degradation or structural disruption of endospore components.

These findings imply that LPMO activity might facilitate germination as evidence by the reduction in phase brightness and the breakdown of endospore structures as evidenced by what appeared to be cellular debris, both observations possibly explained by targeting the cortex peptidoglycan. The results indicate a potential role for LPMOs in facilitating endospores germination by facilitating degradation of cortex peptidoglycan.

4.7.4.. LPMOs could exhibit binding affinity for decoated endospores

A binding assay using decoated endospores was conducted to gain further insights into whether *Bs*LPMO10A and *Bl*LPMO10A might bind to the exposed cortex of endospores. The results revealed that *Bs*LPMO10A demonstrated the highest binding affinity (19.8%), followed by *Sc*LPMO10C and *Bl*LPMO10A. This suggests that these LPMOs might bind to endospore components after decoating with SDS.

The relatively high binding of BSA (8.2%), used as a control for non-specific interactions, indicates that some of the observed binding may be due to non-specific interactions, interference from residual spore coat proteins, or potential effects of SDS on the stability of these proteins. Specifically, possible remains of SDS after washing decoated endospores could differentially denature the proteins and affect their binding properties, potentially influencing the estimated binding affinities, while residual spore coat proteins might artificially increase the protein concentration in filtrated fractions. These factors raise important considerations for interpreting the results, emphasizing the need to account for potential artifacts introduced by the decoating process of endospores. Furthermore, these results are based on a single experimental run, and their reproducibility remains to be confirmed.

Future studies should include controls to differentiate between specific and non-specific binding or artifacts, such as using endospores without SDS treatment or alternatively employing proteases for the decoating of endospores. Overall, the binding assay results suggest a potential for the LPMOs tested to interact with endospore components, but careful experimental design and additional controls are necessary to clarify the specificity of these apparent interactions.

4.7.5. Measuring the rate of AscA depletion as an indirect marker of LPMO inactivation

Initially, the quenching effect of ascorbic acid (AscA) on the terbium dipicolinic acid (TbDPA) signal posed a challenge for accurately monitoring LPMO activity during endospore germination. However, this turned into an opportunity to measure AscA depletion as an indirect marker of LPMO activity. LPMO activity involves homolytic cleavage of H_2O_2, generating a hydroxyl radical that, in the absence of substrate, leads to nonproductive reactions such as oxidative damage to the enzyme. This self-oxidation, accelerating in the absence of substrate,

may cause copper to be released from the enzyme, leading to faster Cu(II)-catalyzed AscA oxidation and increased H_2O_2 production, leading to further self-oxidation of the LPMO.

The hypothesis of whether AscA quantification by measuring its quenching effect on the TbDPA signal could be used to infer LPMO inactivation by measuring the rate of AscA consumption, was initially tested using *Sm*LPMO10A, which showed faster AscA depletion in the presence of PASC compared to chitin, perhaps reflecting its lack of binding to PASC leading to enhanced self-oxidative damage and LPMO inactivation observable by the increased rate of AscA consumption. This approach was extended to *Bs*LPMO10A, where slower AscA consumption with chitin and endospores potentially indicated effective enzyme-substrate interactions with both chitin and endospores, protecting the LPMO from rapid inactivation. The rate of AscA depletion was slightly increased for endospores compared to chitin, potentially indicating differences in binding affinity, kinetics, or the availability of binding sites. Although the potential release of DPA from endospores could account for the slight signal increase observed compared to that for chitin, which would artificially elevate the calculated rate of AscA depletion, concurrent OD measurements suggested negligible germination.

However, an alternative explanation for the slower AscA depletion rate for *Bl*LPMO10A in the presence of endospores could potentially relate to the inherent properties of the spores themselves rather than LPMO binding to endospores. Endospores are known for their robust defenses against oxidative stress, partly due to enzymes like catalase present in their outer coat layers, which can decompose hydrogen peroxide into water and oxygen. Thus, the slower depletion of AscA in the presence of endospores might not accurately reflect LPMO binding but could also be influenced by the catalytic breakdown of hydrogen peroxide by spore-associated catalases. This breakdown potentially protects LPMOs in the solution from oxidative damage, thereby slowing the rate of copper release and AscA depletion (Stepnov et al., 2021). Binding assays or product analysis using purified endospore cortex as a substrate could potentially determine whether the decreased rate of AscA depletion observed is due to binding and potential activity on endospores.

4.1. A potential use of TbDPA fluorescence in facilitating substrate screening by allowing quantification of AscA

Preliminary findings suggest that monitoring AscA depletion by its quenching effect on the TbDPA signal could potentially be used as a real-time assay, and might offer advantages over

conventional methods. The measurement of AscA depletion has recently been employed to explore the inactivation dynamics of LPMOs, including investigations into how varying levels of copper saturation impact enzyme activity and AscA depletion (Kuusk et al., 2024; Østby et al., 2023). These studies typically measured absorbance at 265 nm using spectrophotometer cuvettes or in expensive UV-transparent 96-well plates for real-time monitoring to track AscA consumption. In contrast to these absorbance-based methods, the proposed fluorescence-based approach for AscA quantification allows the use of standard 96-well plates due to UV light not having to pass through the plate in order to measure fluorescence, which not only reduces operational costs but also broadens the accessibility of the approach.

Unlike absorbance-based quantification of AscA, which is susceptible to interference, a fluorescence-based TbDPA approach for AscA quantification could provide a more specific and sensitive method with reduced interference for quantification of AscA. These properties might facilitate substrate screening for potential LPMO interactions by enabling AscA quantification in the presence of substrates, and thereby allowing monitoring of differential rates of AscA consumption by LPMOs in the presence of various substrates.

However, interpreting results from this method requires careful calibration due to the non-linear relationship between AscA concentration and signal quenching. Accurate interpretation, particularly in determining whether signal flatlining is due to AscA depletion or LPMO inactivation, necessitates controls showing background fluorescence without AscA and replacing LPMOs with free copper. Variations in LPMO preparations can affect observed rates, so comparisons between different LPMOs and across different batches should be approached with caution. Despite these complexities, the AscA depletion assay might hold promise as an approach to facilitate LPMO substrate screening, could potentially complement existing techniques and open new possibilities for exploring enzyme-substrate interactions in a more effective and accessible manner. Assessing the stability of LPMOs is of utmost importance for their application in biotechnological valorization of lignocellulosic biomass, and fast and specific LPMO assay would simplify substrate screening and affinity for uncharacterized or engineered LPMOs and accelerate biochemical characterization.

4.8. Concluding remarks and implications for future research

The results of this study provide several key insights into the potential roles and interactions of LPMOs derived from *B. spizizenii* and *B. licheniformis* with bacterial cell walls and endospores.

These findings establish a foundation for future investigations that could further clarify the biological functions of these LPMOs, potentially widespread in other bacteria.

While the data suggest that these *Bacillus*-derived LPMOs might enhance lysozyme-mediated peptidoglycan breakdown in vegetative cells, definitive conclusions about whether LPMO activity increases the rate of cell lysis by lysozyme were not made. Future studies should assess the impact of LPMO-mediated reactive oxygen species (ROS) accumulation on the integrity of vegetative cells under the conditions used in this assay.

Moreover, this research offers several indications that *Bs*LPMO10A and *Bl*LPMO10A may facilitate the germination of *Bacillus* endospores. The potential involvement of their GH18s in endospore germination substantiates the hypothesis that the LPMOs under study may assist GH18s in this process. Although using TbDPA fluorescence to monitor germination did not align well with standard LPMO activity assays due to the quenching effect of ascorbic acid, it provided some evidence of LPMO involvement in endospore germination. Optimizing this assay could involve testing alternative reductants to ascorbic acid or using OD_{600} assays, despite the potential sensitivity of OD_{600} measurements to effects like endospore clustering.

A significant indicator of LPMO involvement in endospore germination was observed through phase contrast microscopy, where LPMO-treated endospores appeared phase-gray and showed an apparent size increase. Further investigation could include a more detailed microscopic analysis to compare the number of phase-dark or phase-gray endospores to phase-bright endospores across different treatments for a quantitative assessment.

Future research should explore in greater depth how these LPMOs contribute to endospore germination. This might include assessing endospore viability after LPMO treatment by plating and colony counting, conducting growth curves with LPMO-treated endospores to determine if the rate of outgrowth increases or is initiated earlier. Additionally, the activity of these LPMOs on cortex peptidoglycan can be definitively established by using mass spectrometry or high-performance liquid chromatography for product analysis after treating purified cortex peptidoglycan, and perhaps evaluating their synergistic effects with GH18s involved in cortex degradation. Further insights could be obtained through transcriptomic and proteomic studies, more in-depth promoter screening, and by conducting knockout and overexpression experiments.

Although AscA introduced complexities in germination assays due to its quenching effect on TbDPA fluorescence, employing terbium dipicolinic acid (TbDPA) to monitor ascorbic acid

depletion as an indirect measure of LPMO activity showed promise. Refining this method may result in an indirect but robust, real-time approach for assessing LPMO activity, and could facilitate potential screening of substrates and provide insights into LPMO-substrate interactions.

The findings from this study point to multiple directions for future research that could elucidate the roles and mechanisms of *Bs*LPMO10A and *Bl*LPMO10A in their natural environments and potentially and potentially engineered applications. This may be particularly relevant given the significant roles of *Bacillus* endospores in food preservation and pathogenicity. Pursuing these research avenues could lead to a comprehensive understanding of LPMO functionality, their interactions with bacterial cell walls and endospores, and their potential applications in biotechnology and industrial processes. As research progresses, integrating these findings into broader studies could help to uncover the complex roles of LPMOs in nature and their potential industrial applications, enhancing our knowledge of these enzymes and contributing to innovative solutions for challenges in health, industry, and environmental management.

5. References

Aachmann, F. L., Sørlie, M., Skjåk-Bræk, G., Eijsink, V. G. H., & Vaaje-Kolstad, G. (2012). NMR structure of a lytic polysaccharide monooxygenase provides insight into copper binding, protein dynamics, and substrate interactions. *Proceedings of the National Academy of Sciences*, *109*(46), 18779-18784. https://doi.org/10.1073/pnas.1208822109

Askarian, F., Uchiyama, S., Masson, H., Sørensen, H. V., Golten, O., Bunæs, A. C., Mekasha, S., Røhr Å, K., Kommedal, E., Ludviksen, J. A., Arntzen, M., Schmidt, B., Zurich, R. H., van Sorge, N. M., Eijsink, V. G. H., Krengel, U., Mollnes, T. E., Lewis, N. E., Nizet, V., & Vaaje-Kolstad, G. (2021). The lytic polysaccharide monooxygenase CbpD promotes Pseudomonas aeruginosa virulence in systemic infection. *Nat Commun*, *12*(1), 1230. https://doi.org/10.1038/s41467-021-21473-0

Baek, M., DiMaio, F., Anishchenko, I., Dauparas, J., Ovchinnikov, S., Lee, G. R., Wang, J., Cong, Q., Kinch, L. N., Schaeffer, R. D., Millán, C., Park, H., Adams, C., Glassman, C. R., DeGiovanni, A., Pereira, J. H., Rodrigues, A. V., van Dijk, A. A., Ebrecht, A. C., . . . Baker, D. (2021). Accurate prediction of protein structures and interactions using a three-track neural network. *Science*, *373*(6557), 871-876. https://doi.org/10.1126/science.abj8754

Bissaro, B., & Eijsink, V. G. H. (2023). Lytic polysaccharide monooxygenases: enzymes for controlled and site-specific Fenton-like chemistry. *Essays Biochem*, *67*(3), 575-584. https://doi.org/10.1042/ebc20220250

Bissaro, B., Forsberg, Z., Ni, Y., Hollmann, F., Vaaje-Kolstad, G., & Eijsink, V. G. H. (2016). Fueling biomass-degrading oxidative enzymes by light-driven water oxidation. *Green Chemistry*, *18*(19), 5357-5366. https://doi.org/10.1039/c6gc01666a

Bissaro, B., Røhr, Å. K., Müller, G., Chylenski, P., Skaugen, M., Forsberg, Z., Horn, S. J., Vaaje-Kolstad, G., & Eijsink, V. G. H. (2017). Oxidative cleavage of polysaccharides by monocopper enzymes depends on H2O2. *Nature Chemical Biology*, *13*(10), 1123-1128. https://doi.org/10.1038/nchembio.2470

Book, A. J., Yennamalli, R. M., Takasuka, T. E., Currie, C. R., Phillips, G. N., & Fox, B. G. (2014). Evolution of substrate specificity in bacterial AA10 lytic polysaccharide monooxygenases. *Biotechnology for Biofuels*, *7*(1), 109. https://doi.org/10.1186/1754-6834-7-109

Borisova, A. S., Isaksen, T., Dimarogona, M., Kognole, A. A., Mathiesen, G., Várnai, A., Røhr, Å. K., Payne, C. M., Sørlie, M., Sandgren, M., & Eijsink, V. G. H. (2015). Structural and Functional Characterization of a Lytic Polysaccharide Monooxygenase with Broad Substrate Specificity. *Journal of Biological Chemistry*, *290*(38), 22955-22969. https://doi.org/10.1074/jbc.m115.660183

Calvio, C., Celandroni, F., Ghelardi, E., Amati, G., Salvetti, S., Ceciliani, F., Galizzi, A., & Senesi, S. (2005). Swarming differentiation and swimming motility in Bacillus subtilis are controlled by swrA, a newly identified dicistronic operon. *Journal of Bacteriology*, *187*(15), 5356-5366.

Ciano, L., Davies, G. J., Tolman, W. B., & Walton, P. H. (2018). Bracing copper for the catalytic oxidation of C–H bonds. *Nature Catalysis*, *1*(8), 571-577. https://doi.org/10.1038/s41929-018-0110-9

Cihan, A. C., Tekin, N., Ozcan, B., & Cokmus, C. (2012). The genetic diversity of genus Bacillus and the related genera revealed by 16s rRNA gene sequences and ardra analyses isolated from geothermal regions of turkey. *Braz J Microbiol*, *43*(1), 309-324. https://doi.org/10.1590/s1517-838220120001000037

Courtade, G., & Aachmann, F. L. (2019). Chitin-Active Lytic Polysaccharide Monooxygenases. In (pp. 115-129). Springer Singapore. https://doi.org/10.1007/978-981-13-7318-3_6

Courtade, G., Balzer, S., Forsberg, Z., Vaaje-Kolstad, G., Eijsink, V. G., & Aachmann, F. L. (2015). (1)H, (13)C, (15)N resonance assignment of the chitin-active lytic polysaccharide monooxygenase BlLPMO10A from Bacillus licheniformis. *Biomol NMR Assign*, *9*(1), 207-210. https://doi.org/10.1007/s12104-014-9575-x

Debroy, S., Dao, J., Söderberg, M., Rossier, O., & Cianciotto, N. P. (2006). Legionella pneumophila type II secretome reveals unique exoproteins and a chitinase that promotes bacterial persistence in the lung. *Proceedings of the National Academy of Sciences*, *103*(50), 19146-19151. https://doi.org/10.1073/pnas.0608279103

Egan, A. J. F., Cleverley, R. M., Peters, K., Lewis, R. J., & Vollmer, W. (2017). Regulation of bacterial cell wall growth. *The FEBS Journal*, *284*(6), 851-867. https://doi.org/10.1111/febs.13959

Eijsink, V. G. H., Petrovic, D., Forsberg, Z., Mekasha, S., Røhr, Å. K., Várnai, A., Bissaro, B., & Vaaje-Kolstad, G. (2019). On the functional characterization of lytic polysaccharide monooxygenases (LPMOs). *Biotechnology for Biofuels*, *12*(1). https://doi.org/10.1186/s13068-019-1392-0

Errington, J. (2010). From spores to antibiotics via the cell cycle. *Microbiology*, *156*(1), 1-13. https://doi.org/10.1099/mic.0.035634-0

Finn, R. D., Bateman, A., Clements, J., Coggill, P., Eberhardt, R. Y., Eddy, S. R., Heger, A., Hetherington, K., Holm, L., Mistry, J., Sonnhammer, E. L. L., Tate, J., & Punta, M. (2014). Pfam: the protein families database. *Nucleic Acids Research*, *42*(D1), D222-D230. https://doi.org/10.1093/nar/gkt1223

Fittolani, G., Djalali, S., Chaube, M. A., Tyrikos-Ergas, T., Dal Colle, M. C. S., Grafmüller, A., Seeberger, P. H., & Delbianco, M. (2022). Deoxyfluorination tunes the aggregation of cellulose and chitin oligosaccharides and highlights the role of specific hydroxyl groups in the crystallization process. *Organic & Biomolecular Chemistry*, *20*(42), 8228-8235. https://doi.org/10.1039/d2ob01601j

Forsberg, Z., & Courtade, G. (2023). On the impact of carbohydrate-binding modules (CBMs) in lytic polysaccharide monooxygenases (LPMOs). *Essays in Biochemistry*, *67*(3), 561-574. https://doi.org/10.1042/ebc20220162

Forsberg, Z., Mackenzie, A. K., Sørlie, M., Røhr Å, K., Helland, R., Arvai, A. S., Vaaje-Kolstad, G., & Eijsink, V. G. (2014). Structural and functional characterization of a conserved pair of bacterial cellulose-oxidizing lytic polysaccharide monooxygenases. *Proc Natl Acad Sci U S A*, *111*(23), 8446-8451. https://doi.org/10.1073/pnas.1402771111

Forsberg, Z., Røhr, A. K., Mekasha, S., Andersson, K. K., Eijsink, V. G., Vaaje-Kolstad, G., & Sørlie, M. (2014). Comparative study of two chitin-active and two cellulose-active AA10-type lytic polysaccharide monooxygenases. *Biochemistry*, *53*(10), 1647-1656. https://doi.org/10.1021/bi5000433

Foster, S. J., & Johnstone, K. (1990). Pulling the trigger: the mechanism of bacterial spore germination. *Molecular Microbiology*, *4*(1), 137-141. https://doi.org/10.1111/j.1365-2958.1990.tb02023.x

Fowler, C. A., Sabbadin, F., Ciano, L., Hemsworth, G. R., Elias, L., Bruce, N., McQueen-Mason, S., Davies, G. J., & Walton, P. H. (2019). Discovery, activity and characterisation of an AA10 lytic polysaccharide oxygenase from the shipworm symbiont Teredinibacter turnerae. *Biotechnol Biofuels*, *12*, 232. https://doi.org/10.1186/s13068-019-1573-x

Frederiksen, R. F., Paspaliari, D. K., Larsen, T., Storgaard, B. G., Larsen, M. H., Ingmer, H., Palcic, M. M., & Leisner, J. J. (2013). Bacterial chitinases and chitin-binding proteins as virulence factors. *Microbiology (Reading)*, *159*(Pt 5), 833-847. https://doi.org/10.1099/mic.0.051839-0

Garcia-Gonzalez, E., Poppinga, L., Fünfhaus, A., Hertlein, G., Hedtke, K., Jakubowska, A., & Genersch, E. (2014). Paenibacillus larvae Chitin-Degrading Protein PlCBP49 Is a Key

Virulence Factor in American Foulbrood of Honey Bees. *PLoS Pathogens*, *10*(7), e1004284. https://doi.org/10.1371/journal.ppat.1004284

Garcia-Santamarina, S., Probst, C., Festa, R. A., Ding, C., Smith, A. D., Conklin, S. E., Brander, S., Kinch, L. N., Grishin, N. V., Franz, K. J., Riggs-Gelasco, P., Lo Leggio, L., Johansen, K. S., & Thiele, D. J. (2020). A lytic polysaccharide monooxygenase-like protein functions in fungal copper import and meningitis. *Nature Chemical Biology*, *16*(3), 337-344. https://doi.org/10.1038/s41589-019-0437-9

Gonçalves, A. P., Heller, J., Span, E. A., Rosenfield, G., Do, H. P., Palma-Guerrero, J., Requena, N., Marletta, M. A., & Glass, N. L. (2019). Allorecognition upon Fungal Cell-Cell Contact Determines Social Cooperation and Impacts the Acquisition of Multicellularity. *Curr Biol*, *29*(18), 3006-3017.e3003. https://doi.org/10.1016/j.cub.2019.07.060

Gordon, R. (1981). One hundred and seven years of the genus Bacillus. *The aerobic endospore-forming bacteria: classification and identification*, 1-15.

Guo, X., An, Y., Jiang, L., Zhang, J., Lu, F., & Liu, F. (2022). The discovery and enzymatic characterization of a novel AA10 LPMO from Bacillus amyloliquefaciens with dual substrate specificity. *International Journal of Biological Macromolecules*, *203*, 457-465. https://doi.org/https://doi.org/10.1016/j.ijbiomac.2022.01.110

Harris, P. V., Welner, D., McFarland, K. C., Re, E., Navarro Poulsen, J.-C., Brown, K., Salbo, R., Ding, H., Vlasenko, E., Merino, S., Xu, F., Cherry, J., Larsen, S., & Lo Leggio, L. (2010). Stimulation of Lignocellulosic Biomass Hydrolysis by Proteins of Glycoside Hydrolase Family 61: Structure and Function of a Large, Enigmatic Family. *Biochemistry*, *49*(15), 3305-3316. https://doi.org/10.1021/bi100009p

Hemsworth, G. R., Davies, G. J., & Walton, P. H. (2013). Recent insights into copper-containing lytic polysaccharide mono-oxygenases. *Current Opinion in Structural Biology*, *23*(5), 660-668. https://doi.org/10.1016/j.sbi.2013.05.006

Hemsworth, G. R., Taylor, E. J., Kim, R. Q., Gregory, R. C., Lewis, S. J., Turkenburg, J. P., Parkin, A., Davies, G. J., & Walton, P. H. (2013). The Copper Active Site of CBM33 Polysaccharide Oxygenases. *Journal of the American Chemical Society*, *135*(16), 6069-6077. https://doi.org/10.1021/ja402106e

Holm, L., Laiho, A., Törönen, P., & Salgado, M. (2023). DALI shines a light on remote homologs: One hundred discoveries. *Protein Science*, *32*(1). https://doi.org/10.1002/pro.4519

Hosono, C., Matsuda, R., Adryan, B., & Samakovlis, C. (2015). Transient junction anisotropies orient annular cell polarization in the Drosophila airway tubes. *Nat Cell Biol*, *17*(12), 1569-1576. https://doi.org/10.1038/ncb3267

Jones, S. M., Transue, W. J., Meier, K. K., Kelemen, B., & Solomon, E. I. (2020). Kinetic analysis of amino acid radicals formed in H ₂ O ₂ -driven Cu ^I LPMO reoxidation implicates dominant homolytic reactivity. *Proceedings of the National Academy of Sciences*, *117*(22), 11916-11922. https://doi.org/10.1073/pnas.1922499117

Jumper, J., Evans, R., Pritzel, A., Green, T., Figurnov, M., Ronneberger, O., Tunyasuvunakool, K., Bates, R., Žídek, A., Potapenko, A., Bridgland, A., Meyer, C., Kohl, S. A. A., Ballard, A. J., Cowie, A., Romera-Paredes, B., Nikolov, S., Jain, R., Adler, J., . . . Hassabis, D. (2021). Highly accurate protein structure prediction with AlphaFold. *Nature*, *596*(7873), 583-589. https://doi.org/10.1038/s41586-021-03819-2

Kawada, M., Chen, C.-C., Arihiro, A., Nagatani, K., Watanabe, T., & Mizoguchi, E. (2008). Chitinase 3-like-1 enhances bacterial adhesion to colonic epithelial cells through the interaction with bacterial chitin-binding protein. *Laboratory Investigation*, *88*(8), 883-895. https://doi.org/10.1038/labinvest.2008.47

Khanna, K., Lopez-Garrido, J., & Pogliano, K. (2020). Shaping an Endospore: Architectural Transformations During Bacillus subtilis Sporulation. *Annual Review of Microbiology*, *74*(1), 361-386. https://doi.org/10.1146/annurev-micro-022520-074650

Kochan Travis, J., Shoshiev Michelle, S., Hastie Jessica, L., Somers Madeline, J., Plotnick Yael, M., Gutierrez-Munoz Daniela, F., Foss Elissa, D., Schubert Alyxandria, M., Smith Ashley, D., Zimmerman Sally, K., Carlson Paul, E., & Hanna Philip, C. (2018). Germinant Synergy Facilitates Clostridium difficile Spore Germination under Physiological Conditions. *mSphere*, *3*(5), 10.1128/msphere.00335-00318. https://doi.org/10.1128/msphere.00335-18

Kuusk, S., Kont, R., Kuusk, P., Heering, A., Sørlie, M., Bissaro, B., Eijsink, V. G. H., & Väljamäe, P. (2019). Kinetic insights into the role of the reductant in H2O2-driven degradation of chitin by a bacterial lytic polysaccharide monooxygenase. *Journal of Biological Chemistry*, *294*(5), 1516-1528. https://doi.org/10.1074/jbc.ra118.006196

Kuusk, S., & Väljamäe, P. (2021). Kinetics of H(2)O(2)-driven catalysis by a lytic polysaccharide monooxygenase from the fungus Trichoderma reesei. *J Biol Chem*, *297*(5), 101256. https://doi.org/10.1016/j.jbc.2021.101256

Letunic, I., & Bork, P. (2024). Interactive Tree of Life (iTOL) v6: recent updates to the phylogenetic tree display and annotation tool. *Nucleic Acids Research*, gkae268. https://doi.org/10.1093/nar/gkae268

Li, Y., Liu, X., Liu, M., Wang, Y., Zou, Y., You, Y., Yang, L., Hu, J., Zhang, H., Zheng, X., Wang, P., & Zhang, Z. (2020). Magnaporthe oryzae Auxiliary Activity Protein MoAa91 Functions as Chitin-Binding Protein To Induce Appressorium Formation on Artificial Inductive Surfaces and Suppress Plant Immunity. *mBio*, *11*(2). https://doi.org/10.1128/mbio.03304-19

Liu, B. (2019). *Dissecting function and catalytic mechanism of fungal lytic polysaccharide monooxygenases* https://pub.epsilon.slu.se/16247/7/liu_b_190723.pdf

Liu, X., Ma, X., Lei, C., Xiao, Y., Zhang, Z., & Sun, X. (2011). Synergistic effects of Cydia pomonella granulovirus GP37 on the infectivity of nucleopolyhedroviruses and the lethality of Bacillus thuringiensis. *Arch Virol*, *156*(10), 1707-1715. https://doi.org/10.1007/s00705-011-1039-3

Logan, N. A., & De Vos, P. (2009). Genus I. bacillus. *Bergey's manual of systematic bacteriology*, *3*, 21-128.

Løvdal, I. S., From, C., Madslien, E. H., Romundset, K. C. S., Klufterud, E., Rosnes, J. T., & Granum, P. E. (2012). Role of the gerA operon in L-alanine germination of Bacillus licheniformisspores. *BMC Microbiology*, *12*(1), 34. https://doi.org/10.1186/1471-2180-12-34

Manjeet, K., Purushotham, P., Neeraja, C., & Podile, A. R. (2013). Bacterial chitin binding proteins show differential substrate binding and synergy with chitinases. *Microbiological Research*, *168*(7), 461-468. https://doi.org/10.1016/j.micres.2013.01.006

Mirdita, M., Schütze, K., Moriwaki, Y., Heo, L., Ovchinnikov, S., & Steinegger, M. (2022). ColabFold: making protein folding accessible to all. *Nature Methods*, *19*(6), 679-682. https://doi.org/10.1038/s41592-022-01488-1

Mummery-Widmer, J. L., Yamazaki, M., Stoeger, T., Novatchkova, M., Bhalerao, S., Chen, D., Dietzl, G., Dickson, B. J., & Knoblich, J. A. (2009). Genome-wide analysis of Notch signalling in Drosophila by transgenic RNAi. *Nature*, *458*(7241), 987-992. https://doi.org/10.1038/nature07936

Munzone, A., Eijsink, V. G. H., Berrin, J. G., & Bissaro, B. (2024). Expanding the catalytic landscape of metalloenzymes with lytic polysaccharide monooxygenases. *Nat Rev Chem*, *8*(2), 106-119. https://doi.org/10.1038/s41570-023-00565-z

Østby, H., Tuveng, T. R., Stepnov, A. A., Vaaje-Kolstad, G., Forsberg, Z., & Eijsink, V. G. H. (2023). Impact of Copper Saturation on Lytic Polysaccharide Monooxygenase Performance. *ACS*

Sustainable Chemistry & Engineering, *11*(43), 15566-15576. https://doi.org/10.1021/acssuschemeng.3c03714

Pezza, J. A., Kucera, R., & Sun, L. (n.d.). Polymerase Fidelity: What is it, and what does it mean for your PCR? https://www.neb-online.de/wp-content/uploads/2018/06/Polymerase-Fidelity-What-is-it-and-what-does-it-mean-for-your-PCR.pdf

Phillips, C. M., Beeson, W. T., Cate, J. H., & Marletta, M. A. (2011). Cellobiose Dehydrogenase and a Copper-Dependent Polysaccharide Monooxygenase Potentiate Cellulose Degradation by Neurospora crassa. *ACS Chemical Biology*, *6*(12), 1399-1406. https://doi.org/10.1021/cb200351y

Polonio, Á., Fernández-Ortuño, D., De Vicente, A., & Pérez-García, A. (2021). A haustorial-expressed lytic polysaccharide monooxygenase from the cucurbit powdery mildew pathogen Podosphaera xanthii contributes to the suppression of chitin-triggered immunity. *Molecular Plant Pathology*, *22*(5), 580-601. https://doi.org/10.1111/mpp.13045

Quinlan, R. J., Sweeney, M. D., Lo Leggio, L., Otten, H., Poulsen, J.-C. N., Johansen, K. S., Krogh, K. B. R. M., Jørgensen, C. I., Tovborg, M., Anthonsen, A., Tryfona, T., Walter, C. P., Dupree, P., Xu, F., Davies, G. J., & Walton, P. H. (2011). Insights into the oxidative degradation of cellulose by a copper metalloenzyme that exploits biomass components. *Proceedings of the National Academy of Sciences*, *108*(37), 15079-15084. https://doi.org/10.1073/pnas.1105776108

Ramos, O. S., & Malcata, F. X. (2011). 3.48 - Food-Grade Enzymes. In M. Moo-Young (Ed.), *Comprehensive Biotechnology (Second Edition)* (pp. 555-569). Academic Press. https://doi.org/https://doi.org/10.1016/B978-0-08-088504-9.00213-0

Ribis, J. W., & Shen, A. (2023). Protocol for quantifying the germination properties of individual bacterial endospores using PySpore. *STAR Protocols*, *4*(4), 102678. https://doi.org/https://doi.org/10.1016/j.xpro.2023.102678

Romero-Rodríguez, A., Ruiz-Villafán, B., Martínez-de la Peña, C. F., & Sánchez, S. (2023). Targeting the Impossible: A Review of New Strategies against Endospores. *Antibiotics*, *12*(2).

Sabbadin, F., Hemsworth, G. R., Ciano, L., Henrissat, B., Dupree, P., Tryfona, T., Marques, R. D. S., Sweeney, S. T., Besser, K., Elias, L., Pesante, G., Li, Y., Dowle, A. A., Bates, R., Gomez, L. D., Simister, R., Davies, G. J., Walton, P. H., Bruce, N. C., & McQueen-Mason, S. J. (2018). An ancient family of lytic polysaccharide monooxygenases with roles in arthropod development and biomass digestion. *Nat Commun*, *9*(1), 756. https://doi.org/10.1038/s41467-018-03142-x

Schleifer, K. H., & Kandler, O. (1972). Peptidoglycan types of bacterial cell walls and their taxonomic implications. *Bacteriol Rev*, *36*(4), 407-477. https://doi.org/10.1128/br.36.4.407-477.1972

Setlow, B., Melly, E., & Setlow, P. (2001). Properties of spores of Bacillus subtilis blocked at an intermediate stage in spore germination. *Journal of Bacteriology*, *183*(16), 4894-4899.

Setlow, P., Wang, S., & Li, Y. Q. (2017). Germination of Spores of the Orders Bacillales and Clostridiales. *Annu Rev Microbiol*, *71*, 459-477. https://doi.org/10.1146/annurev-micro-090816-093558

Shukla, A. K., Upadhyay, S. K., Mishra, M., Saurabh, S., Singh, R., Singh, H., Thakur, N., Rai, P., Pandey, P., Hans, A. L., Srivastava, S., Rajapure, V., Yadav, S. K., Singh, M. K., Kumar, J., Chandrashekar, K., Verma, P. C., Singh, A. P., Nair, K. N., . . . Singh, P. K. (2016). Expression of an insecticidal fern protein in cotton protects against whitefly. *Nat Biotechnol*, *34*(10), 1046-1051. https://doi.org/10.1038/nbt.3665

Stepnov, A. A., Christensen, I. A., Forsberg, Z., Aachmann, F. L., Courtade, G., & Eijsink, V. G. H. (2022). The impact of reductants on the catalytic efficiency of a lytic polysaccharide monooxygenase and the special role of dehydroascorbic acid. *FEBS Letters*, *596*(1), 53-70. https://doi.org/10.1002/1873-3468.14246

Stepnov, A. A., Forsberg, Z., Sørlie, M., Nguyen, G.-S., Wentzel, A., Røhr, Å. K., & Eijsink, V. G. H. (2021). Unraveling the roles of the reductant and free copper ions in LPMO kinetics. *Biotechnology for Biofuels*, *14*(1). https://doi.org/10.1186/s13068-021-01879-0

Takasuka, T. E., Book, A. J., Lewin, G. R., Currie, C. R., & Fox, B. G. (2013). Aerobic deconstruction of cellulosic biomass by an insect-associated Streptomyces. *Scientific Reports*, *3*(1). https://doi.org/10.1038/srep01030

Tran, H. T., Barnich, N., & Mizoguchi, E. (2011). Potential role of chitinases and chitin-binding proteins in host-microbial interactions during the development of intestinal inflammation. *Histol Histopathol*, *26*(11), 1453-1464. https://doi.org/10.14670/hh-26.1453

Trowsdale, J., & Smith, D. A. (1975). Isolation, characterization, and mapping of Bacillus subtilis 168 germination mutants. *J Bacteriol*, *123*(1), 83-95. https://doi.org/10.1128/jb.123.1.83-95.1975

Vaaje-Kolstad, G., Forsberg, Z., Loose, J. S., Bissaro, B., & Eijsink, V. G. (2017). Structural diversity of lytic polysaccharide monooxygenases. *Current Opinion in Structural Biology*, *44*, 67-76. https://doi.org/10.1016/j.sbi.2016.12.012

Vaaje-Kolstad, G., Horn, S. J., van Aalten, D. M. F., Synstad, B., & Eijsink, V. G. H. (2005). The Non-catalytic Chitin-binding Protein CBP21 from Serratia marcescens Is Essential for Chitin Degradation*♦. *Journal of Biological Chemistry*, *280*(31), 28492-28497. https://doi.org/https://doi.org/10.1074/jbc.M504468200

Vaaje-Kolstad, G., Houston, D. R., Riemen, A. H. K., Eijsink, V. G. H., & van Aalten, D. M. F. (2005). Crystal Structure and Binding Properties of the Serratia marcescens Chitin-binding Protein CBP21*. *Journal of Biological Chemistry*, *280*(12), 11313-11319. https://doi.org/https://doi.org/10.1074/jbc.M407175200

Vaaje-Kolstad, G., Westereng, B., Horn, S. J., Liu, Z., Zhai, H., Sørlie, M., & Eijsink, V. G. H. (2010). An Oxidative Enzyme Boosting the Enzymatic Conversion of Recalcitrant Polysaccharides. *Science*, *330*(6001), 219-222. https://doi.org/10.1126/science.1192231

Van Gestel, J., Vlamakis, H., & Kolter, R. (2015). From cell differentiation to cell collectives: Bacillus subtilis uses division of labor to migrate. *PLoS biology*, *13*(4), e1002141.

van Kempen, M., Kim, S. S., Tumescheit, C., Mirdita, M., Lee, J., Gilchrist, C. L. M., Söding, J., & Steinegger, M. (2024). Fast and accurate protein structure search with Foldseek. *Nature Biotechnology*, *42*(2), 243-246. https://doi.org/10.1038/s41587-023-01773-0

Vandhana, T. M., Reyre, J. L., Sushmaa, D., Berrin, J. G., Bissaro, B., & Madhuprakash, J. (2022). On the expansion of biological functions of lytic polysaccharide monooxygenases. *New Phytol*, *233*(6), 2380-2396. https://doi.org/10.1111/nph.17921

Veith, B., Herzberg, C., Steckel, S., Feesche, J., Maurer, K. H., Ehrenreich, P., Bäumer, S., Henne, A., Liesegang, H., & Merkl, R. (2004). The complete genome sequence of Bacillus licheniformis DSM13, an organism with great industrial potential. *Journal of molecular microbiology and biotechnology*, *7*(4), 204-211.

Voshol, G. P., Punt, P. J., & Vijgenboom, E. (2019). Profile Comparer Extended: phylogeny of lytic polysaccharide monooxygenase families using profile hidden Markov model alignments. *F1000Res*, *8*, 1834. https://doi.org/10.12688/f1000research.21104.1

Walter, A., & Mayer, C. (2019). Peptidoglycan Structure, Biosynthesis, and Dynamics During Bacterial Growth. In E. Cohen & H. Merzendorfer (Eds.), *Extracellular Sugar-Based Biopolymers Matrices* (pp. 237-299). Springer International Publishing. https://doi.org/10.1007/978-3-030-12919-4_6

Waschkau, B., Waldeck, J., Wieland, S., Eichstädt, R., & Meinhardt, F. (2008). Generation of readily transformable Bacillus licheniformis mutants. *Applied microbiology and biotechnology*, *78*, 181-188.

Waschkau, B., Waldeck, J., Wieland, S., Eichstädt, R., & Meinhardt, F. (2008). Generation of readily transformable Bacillus licheniformis mutants. *Appl Microbiol Biotechnol*, *78*(1), 181-188. https://doi.org/10.1007/s00253-007-1278-0

Weidel, W., & Pelzer, H. (1964). BAGSHAPED MACROMOLECULES--A NEW OUTLOOK ON BACTERIAL CELL WALLS. *Adv Enzymol Relat Subj Biochem*, *26*, 193-232. https://doi.org/10.1002/9780470122716.ch5

Westereng, B., Cannella, D., Wittrup Agger, J., Jørgensen, H., Larsen Andersen, M., Eijsink, V. G. H., & Felby, C. (2015). Enzymatic cellulose oxidation is linked to lignin by long-range electron transfer. *Scientific Reports*, *5*(1), 18561. https://doi.org/10.1038/srep18561

Wiegand, S., Dietrich, S., Hertel, R., Bongaerts, J., Evers, S., Volland, S., Daniel, R., & Liesegang, H. (2013). RNA-Seq of Bacillus licheniformis: active regulatory RNA features expressed within a productive fermentation. *BMC Genomics*, *14*(1), 667. https://doi.org/10.1186/1471-2164-14-667

Wong, E., Vaaje-Kolstad, G., Ghosh, A., Hurtado-Guerrero, R., Konarev, P. V., Ibrahim, A. F. M., Svergun, D. I., Eijsink, V. G. H., Chatterjee, N. S., & Van Aalten, D. M. F. (2012). The Vibrio cholerae Colonization Factor GbpA Possesses a Modular Structure that Governs Binding to Different Host Surfaces. *PLoS Pathogens*, *8*(1), e1002373. https://doi.org/10.1371/journal.ppat.1002373

Yadav, S. K., Archana, Singh, R., Singh, P. K., & Vasudev, P. G. (2019). Insecticidal fern protein Tma12 is possibly a lytic polysaccharide monooxygenase. *Planta*, *249*(6), 1987-1996. https://doi.org/10.1007/s00425-019-03135-0

Yang, J., Klassen, H., Pries, M., Wang, W., & Nissen, M. H. (2006). Aqueous Humor Enhances the Proliferation of Rat Retinal Precursor Cells in Culture, and This Effect Is Partially Reproduced by Ascorbic Acid. *STEM CELLS*, *24*(12), 2766-2775. https://doi.org/10.1634/stemcells.2006-0103

Yi, X., & Setlow, P. (2010). Studies of the commitment step in the germination of spores of bacillus species. *J Bacteriol*, *192*(13), 3424-3433. https://doi.org/10.1128/jb.00326-10

Zhong, X., Zhang, L., van Wezel, G. P., Vijgenboom, E., & Claessen, D. (2022). Role for a Lytic Polysaccharide Monooxygenase in Cell Wall Remodeling in Streptomyces coelicolor. *mBio*, *13*(2), e0045622. https://doi.org/10.1128/mbio.00456-22

Supplementary Material

Supplement 1

pPro-mCherry synthetic fragment*

gaattagctt**ggtacc**AAGTTTGCCGAAGCCTGCGGCGGGAAGGGCTTCAGCGTGACAAAGCACGAAGAGCTTAT
TCCTGCTTTGAAAAGCGCCTTTCATTCACAAAAGCCGTCGATTATCGATGTGGCAATTGAAGACGAACCGCCTC
TTCCGGGAAAAATATCCTATACACAAGCTGTAAACTACAGCAAATATATGATCAAAAAACTAGTTGAGAAAAAA
GAGCTCGACTTGCCGCCGCTGAAAAAAAGTTTAAAAAGGATTTTTTAGTATGATGCCAAGGGAGATCGTCCCT
TGGCTTTATAACGGTCAGATGTTAAAATTGAATGGGTAATATTGGAATGGCCGCGTATGTTTTCTTTTTGCATCA
AAACCCGTCTCAACACTGTGAAAAGAGAGGGGATTGTCATATGAGCAAAGGAGAAGAAGATAACATGGCAAT
CATCAAAGAATTTATGCGTTTCAAAGTTCACATGGAAGGTTCTGTAAACGGACACGAATTTGAAATTGAAGGT
GAAGGTGAAGGCCGTCCTTATGAAGGAACACAAACGGCAAAGCTGAAAGTAACAAAAGGCGGACCGCTTCC
GTTTGCATGGGATATCCTTTCTCCGCAATTCATGTACGGTTCAAAAGCATACGTGAAGCATCCGGCTGATATTCC
TGATTATTTGAAGCTGTCATTCCCTGAAGGCTTCAAATGGGAGCGTGTGATGAACTTTGAAGATGGCGGTGTT
GTTACTGTTACTCAAGATTCAAGCCTTCAAGACGGTGAATTTATTTACAAAGTGAAGCTGCGCGGAACAAACT
TCCCATCTGACGGACCTGTCATGCAAAAGAAAACAATGGGCTGGGAAGCAAGCTCTGAACGCATGTATCCAG
AGGACGGTGCTTTAAAAGGAGAAATCAAACAGCGTTTGAAGCTGAAAGACGGCGGACACTATGACGCTGAA
GTGAAAACAACTTACAAAGCGAAAAAGCCGGTTCAGCTTCCAGGTGCTTACAACGTAAACATCAAACTTGATA
TTACAAGCCACAATGAAGATTATACGATTGTTGAACAATATGAACGCGCTGAAGGCCGTCATTCAACTGGCGG
AATGGATGAGCTTTACAAATAA**cccggg**gcagcccgcc

**Restriction sites are indicated in bold, underlined; tails are indicated in lower case; the 400 bp section upstream of Bl*LPMO10A *constituting the promoter part of the fragment is indicated in blue; the gene encoding mCherry is indicated in pink.*

Supplement 2

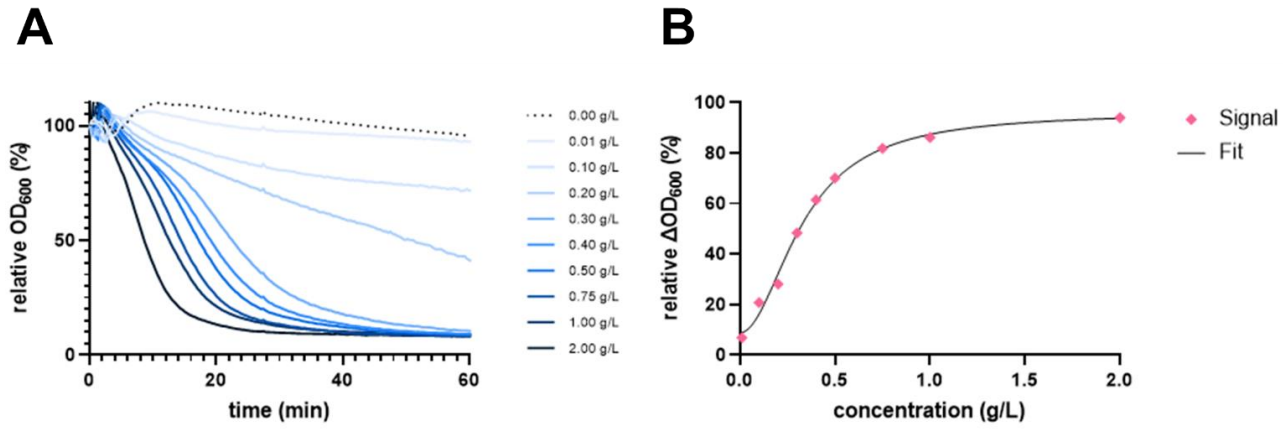

Figure S1. Lysozyme-mediated lysis of *B. licheniformis* cells. (A) Time-dependent lysis profiles of *B. licheniformis*, measured as relative optical density at 600 nm (OD_{600}), over a 60-minute period with varying concentrations of lysozyme. Each curve represents the lysis trajectory for *B. licheniformis* vegetative cells standardized to an initial OD_{600} of approximately 2.5, treated with lysozyme concentrations ranging from 0.01

g/L to 2 g/L. The increasing rate of lysis with increasing lysozyme concentrations demonstrates a dose-responsive effect. **(B)** Dose-response curve showing the percentage decrease in OD_{600} of *B. licheniformis* after 20 minutes of treatment with lysozyme. Data points (diamonds) based on single measurements indicate the measured decrease in OD_{600} at each lysozyme concentration, while the solid line depicts the fitted model.'

Supplement 3

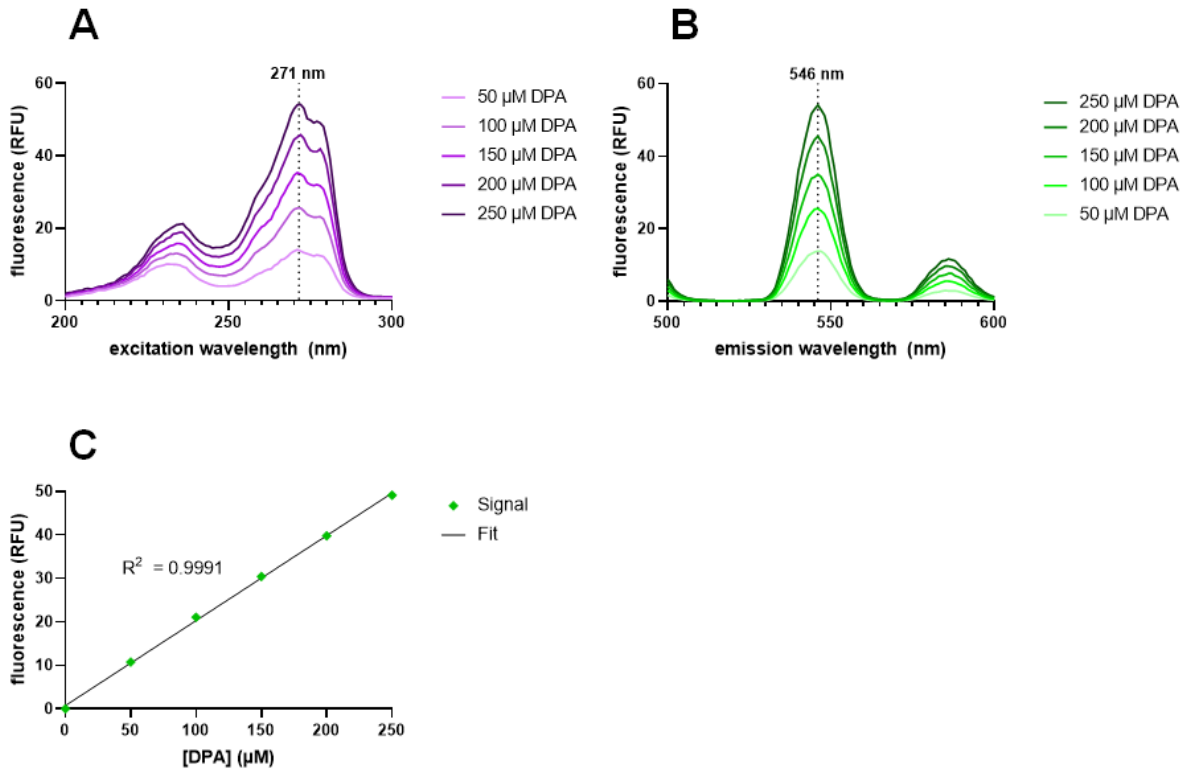

Figure S2: Spectral Analysis and Calibration of the TbDPA Complex for DPA Quantification. (A) Excitation spectrum of the TbDPA complex, with a maximum fluorescence intensity at 545 nm emission occurring at an excitation wavelength of 271 nm. **(B)** Emission spectrum of the TbDPA complex, with a maximum fluorescence intensity observed at 546 nm when excited at 270 nm. The spectral responses in (A) and (B) were recorded through a range of DPA concentrations (50 µM, 100 µM, 150 µM, 200 µM, 250 µM). **(C)** A calibration curve correlating fluorescence intensity (RFU) with DPA concentration, demonstrating a highly linear relationship as indicated by the regression coefficient (R2=0.9991)

Supplement 4

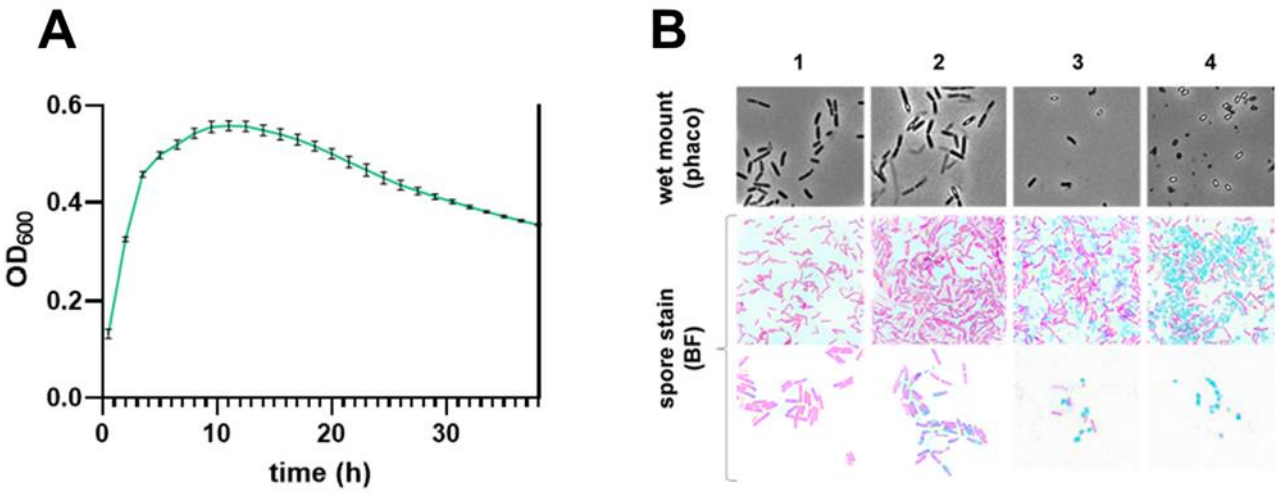

Figure S3. Generation of *B. licheniformis* endospores. (A) Optical density **(**OD_{600}) was continuously measured every 15 min for 36 hours in sporulation medium at 37° C. Each datapoint represents the mean of three technical replicates ± standard deviation. (B) Schaeffer-Fulton staining of endospores. Panels 1-4 represent days 1-4 after inoculation in the generation of B. licheniformis endospores. Top row: phase-contrast microscopy of wet mounts. Middle row: bright-field microscopy images after spore staining, showing both vegetative cells (pink) and endospores (green). Bottom row: magnified views of spore-stained cells.

Norges miljø- og biovitenskapelige universitet
Noregs miljø- og biovitskapelege universitet
Norwegian University of Life Sciences

Postboks 5003
NO-1432 Ås
Norway